Dynamics of Vapor Bubbles and Associated Heat Transfer in Various Regimes of Boiling

A thesis submitted in partial fulfillment of the requirements for the degree of

Doctor of Philosophy

by

Vinod Pandey

Department of Mechanical Engineering
Indian Institute of Technology Guwahati- 781039, India
April 2018

CERTIFICATE

It is certified that the work contained in the thesis entitled **"Dynamics of Vapor Bubbles and Associated Heat Transfer in Various Regimes of Boiling"**, by Vinod Pandey (ID no. 136103021) has been carried out under our supervision and that this work has not been submitted elsewhere for a degree.

(Gautam Biswas)
Professor
Department of Mechanical Engineering
Indian Institute of Technology Guwahati

(Amaresh Dalal)
Associate Professor
Department of Mechanical Engineering
Indian Institute of Technology Guwahati

April 2018

To the loving memories of my Parents

Acknowledgements

"Showing gratitude is one of the simplest yet most powerful things humans can do for each other." -Randy Pausch

The time spent during the years of my doctoral work has been the most beautiful and memorable part of my life which would have not been the same without the influence of some people - directly or indirectly.

First and the foremost, I would like to express my sincere gratitude to my thesis advisors Prof. Gautam Biswas and Prof. Amaresh Dalal for their continuous encouragement. Prof. Biswas has been a constant source of inspiration to me. Every discussion or even a small meeting with him have always infused in me an inquisitiveness and a positive attitude towards my research work. He has never discouraged any idea or doubt I had presented and has always endowed his various valuable prepositions and suggestions which have culminated into the present work. His advices and teachings have helped me build my fundamentals on the subject of boiling. I consider myself fortunate to have had such an advisor who dedicates his valuable time and attention for his students inspite of his busy schedule. Prof. Dalal had been a mentor who was always there to help whenever needed, both personally and professionally. Because of him, I got the opportunity to work in Anupravaha lab in the company of various good researchers and freinds. I am extremely thankful to my supervisors for showing confidence in me throughout the thesis work and providing me an independent environment for my work.

I would also like to express my sincere gratitude and humble respect to Prof. Anoop K. Dass, Prof. Pinakeshwar Mahanta, Prof. Nanda Kishore, Prof. Ganesh Natarajan and Prof. Dipankar Bandopadhyay for their useful suggestions and questions as the doctoral committee members. Their evaluation has helped in improving

the quality of the thesis. My sincere respect and acknowledgement goes to various faculty members of the Department of Mechanical Engineering, IIT Guwahati who have taught various courses. Especially Fluid Mechanics course taught by Prof. Arnab De and courses taught by Prof. Ganesh Natarajan have helped me build an interest into the fluid and thermal engineering field. Their dedicated and enthusiastic mode of pedagogy has always been inspiring for students. I am very much thankful to Prof. Vijay Kumar Dhir for providing a deep insight into the area of boiling during his visit to IIT Guwahati. His teachings during the course on 'Boiling Heat Transfer' have motivated and helped me in my work related to the study of nucleate boiling.

A pleasant workplace makes a healthy mind. The workplace becomes pleasant by the presence of people having cooperative behavior; I have been lucky to get the same. I highly appreciate my labmates Dr. Jai Manik, Mukul, Subrat, Saurabh, Preeti, Shiva and all the present and passed out M.Tech. students of the lab. I am thankful to Dr. Jai Manik, Dr. Jitendra Patel, Mukul Parmananda and Hiranya Deka for various fruitful technical discussions which have helped me understand various nuances of numerical methodology and physical aspects of problems I have dealt with. I also acknowledge the help by Dr. Pitambar Randive during the initial phase of my doctoral work. I cherish the time spent with Hiranya, Manash, Binita, Dhrubo and Vishal while working under the same supervisors and sharing various memorable moments.

Life in IIT Guwahati has been very joyous and pleasant; thanks to the company of various freinds, I feel lucky to have had. It is always great to have company of freinds who share the common interests. I enjoyed the company of Shatru, Siddesh, Prof. Anamika Barua, Basant, Pankaj, Mukul, Shyam, Subrat, Rajendra, Prof. Aditya Panda, Anand, Kishor and Mrs. Swapnali Borah at the badminton courts

and during cycling trips. I specially thank Prof. Anamika Barua for being a freind as well as a mentor and for various thought provoking discussions. I also acknowledge my freinds Prabhjinder, Piyush and Lokesh for all the laughters we shared. This acknowledgement cannot be completed without specially thanking and appreciating Mampi for her support and for always being by my side during these years.

Words can never be enough to express the gratitudes towards my parents and I believe they are always with me with their blessings. My elder brother and sister have always supported me in every decision I have taken, for which, I will always be thankful to them. My family's love and blessings have always been the biggest strength in my life.

Vinod Pandey

Abstract

The dynamics of bubble formation during boiling is highly significant considering its influence on the heat transfer rate associated with various applications. Depending on the heat flux, the mode of boiling transforms from the nucleate boiling regime to the film boiling regime. The present thesis is focused on the study of the varying characteristics of boiling regimes through direct numerical simulations. The liquid-vapor interface-capturing is performed using the CLSVOF (Coupled Level-Set and Volume of Fluid) approach. In the film boiling regime, the phenomenon of bubble formation is governed by the instabilities at the liquid-vapor interface instigated by the combined influence of surface tension, buoyancy, heat flux, vapor thrust or any other applied external field (electric field in the present study). The dynamical disturbances destabilize the interface which results in bubble formation with the passage of time. The bubble release during film boiling is found to be more of a deterministic phenomenon with the separation distance between any two adjacent bubbles being manifested as a function of the most dominant wavelength of disturbance at the interface. Further, the diameter of bubble after departure from the interface is a function of the critical wavelength, which depends on the surface tension and density-ratio between the liquid and the vapor phases. The distance of separation between any two adjacent bubbles is governed by the instability mode at the liquid-vapor interface. The interface growth is found to be governed by the

Rayleigh-Taylor mode of instability at low superheat values and when the superheat is higher it is found to be governed by the Taylor-Helmholtz instability-mode. The bubble morphology is also observed to be highly dependent on the degree of superheat — discrete bubbles are seen at the lower range of superheat values while continuous vapor columns are evinced in case of high superheat values. This in turn affects the heat transfer rate significantly. Bubble growth and departure from the interface follows a regular periodic pattern (both in space and time). As the superheat increases, the time period of bubble-release decreases.

Electric field force results in destabilizing the interface and enhancing the bubble growth rate. Through the applied numerical model of electric force, it was found that the application of electric field normal to the heating surface results in increase of both spatial and temporal frequencies of bubble-formation along the heated surface. The dominant wavelength of disturbance decreases, which in its turn decreases the separation-distance between adjacent bubbles. At a high intensity of electric field, the periodicity of bubble-release diminishes leading to a vigorous and random generation of bubbles. The increased rate of vapor release is accompanied by an increase in vapor-generation and enhanced heat-transfer-rate. The bubble morphology and heat transfer rate is significantly affected only above a minimum threshold-intensity of the applied electric field.

As buoyancy is one of the dominant factors influencing the growth-dynamics of bubbles during boiling, change in the gravity-level results in an apprehensive variation in boiling characteristics. Analyses have been performed at different levels of gravity to determine the changes in bubble morphology and heat-transfer rate. The bubble release-rate decreases as a result of decrease in gravity-level, which goes on to reduce the heat-transfer rate. The application of electric field compensates for this reduction in the heat-transfer rate and recovers the same rate of heat-transfer

as in normal gravity. The dominance of electric field force also increases in case of reduced gravity conditions. Both the length and time scales increase appreciably as a result of reduction in the level of gravity. Variation in geometrical parameters like maximum height and radius of bubble has been analyzed with change in the gravity-level. Bulging of the interface leading to bubble formation and departure is a singularity- phenomenon. During the initial stage of bubble growth, the interfaces exhibit self-similar profiles i.e. the bubble-interface at different instants of time can be converged on a single profile defined by a fitting-function, in which, the variables are normalized using proper scaling-parameters.

Unlike in the film boiling regime, the bubble generation and growth in nucleate boiling is rather intricate. In nucleate boiling, the bubble generation is not instability-dependent but a random process which depends on the heat flux from the surface and the surface-properties. The nucleation starts at cavities as a result of existence of pre-occupied gaseous or vapor phase or due to extreme heat-flux. The rate of bubble growth occurs due to vapor generation at the interface as a result of heat transfer from the superheated-liquid and also due to the microlayer-evaporation. The liquid-microlayer beneath the bubble evaporates completely during the growth of bubble and the region gets dried-out. The dry-out region again gets rewetted when the contact line retracts leading to departure of the bubble from the solid-surface. In the present study, numerical simulations have been performed by incorporating a microlayer-model to account for the contribution of microlayer-evaporation in the growth of a single bubble. The growth rate is found to be affected by the surface-superheat, the wettability of the surface and the degree of subcooling of the ambient liquid. The liquid-subcooling results in condensation of the vapor at the top of the bubble, resulting in the reduction in the growth-rate of the bubble. For a higher degree of subcooling, the bubble does not even depart from the sur-

face. The balance between the evaporation rate and the condensation rate prohibits the buoyancy to dominate and make the bubble depart from the surface; thus, the bubble keeps oscillating at its position. Behavior of the bubble after departure from the surface has also been analyzed at different levels of liquid-subcooling. Extreme reduction in bubble diameter is observed when subcooling of the liquid is increased. The reduction in bubble-size leads to a continuous variation in bubble-rise-velocity in subcooled liquid.

The mode of bubble generation - whether it is from nucleate boiling or film boiling - depends on the intensity of heat flux from the surface. Film boiling occurs at a much higher value of surface-superheat than the nucleate boiling. In between these two above-mentioned regimes, there is a transition regime which exhibits the characteristics of film boiling as well as nucleate boiling. This regime is marked by the existence of both — vapor layer and liquid-solid contact at certain regions of the heated surface. At a superheat higher than the minimum film boiling temperature, the boiling mode transforms to film boiling. The transition regime is highly affected by the wettability of the heated substrate. Simulations have been performed at various values of wettability of the surface to analyze the phenomenon of transition from the film to the nucleate regime of boiling. At high wettability, i.e. at lower contact angle, there is a higher affinity of the surface for the liquid. It has been observed that for surfaces with high wettability, the transition to nucleate boiling from film boiling occurs due to the frequent liquid to solid contacts. For the same value of superheat, such transition is not observed for surfaces with low-wettability. However, when an electric force is applied across the vapor film, liquid-solid contact occurs in low-wettability surfaces too, leading to transition.

Contents

List of Figures

List of Tables

Nomenclature

English Symbols

A	Hamacker constant
c_p	Specific heat capacity
d	Shortest distance of the interface from any point
D	diameter of bubble
$\mathbf{D}_v$	Rate of deformation tensor
$\mathbf{D}$	Electric displacement vector
E	Magnitude of electric field
El^*	Electrical influence number
F	Volume fraction
g	Acceleration due to gravity
h_{lv}	Enthalpy of phase change from liquid to vapor
H	Heaviside function
i, j	Cell numbers in x and y direction, respectively
k	Thermal conductivity
l	Minimum distance of the interface from cell centre
L	Computational domain length
l_s	Capillary length
m	Wave number
$\hat{\mathbf{n}}$	Unit normal vector
$\mathbf{n}$	Normal vector
p	hydrostatic pressure
q	Heat flux
$\mathbf{q}$	Heat flux vector
q_v	Volume charge density
$\mathbf{r}$	Position vector
R	Radius
S	Surface area of the computational region
S_C	Surface area of the computational cell
S_I	Surface area of the phase interface

t	Time
$\mathbf{t}$	Tangential vector
T	Temperature
u	X-direction velocity component
$\mathbf{U}$	Velocity vector
v	Y-direction velocity component
V	Volume of the computational region
x, y	Cartesian coordinates

Greek Symbols

γ	Contact angle
Γ	Electrical conductivity
δ	Half of the thickness of interface
δ_s	Interface delta function
δ_{ml}	thickness of the microlayer
ϵ	Relative dielectric permittivity
ϵ_0	Dielectric permittivity of vaccum
Θ	Parameter based on ratio of surface tension coefficients
κ	Mean curvature of the interface
λ_{01}	Zuber's critical wavelength
λ_{02}	Zuber's most dangerous wavelength wavelength
λ_B	Berenson's most dangerous wavelength
λ_c	Berenson's critical wavelength
λ_J	Johnson's most dangerous wavelength
μ	Dynamic viscosity
ν	Kinematic viscosity
ρ	Density of medium
σ	Surface tension coefficient
$\boldsymbol{\tau}^{\mathrm{v}}$	Viscous stress tensor
$\boldsymbol{\tau}^{\mathrm{E}}$	Maxwell stress tensor
ϕ	Level-set function
χ	Scalar function at cell center

ψ	Electric potential function
ω	Bubble formation frequency

Abbreviations

Gr	Grashoff number
Ja	Jacob number
Nu_{avg}	Space averaged Nusselt number
Re	Reynolds number

Acronyms

CLSVOF	Coupled Level Set and Volume Of Fluid
CSF	Continuum Surface Force
CSS	Continuum Surface Stress
EHD	Electrohydrodynamics
ENO	Essentially Non-Oscillatory
LVIRA	Least square Volume of fluid Interface Reconstruction Algorithm
MAC	Marker And Cell
QUICK	Quadratic Upstream Interpolation for Convective Kinetics
VOF	Volume Of Fluid
WAM	Weighted Arithmatic Mean
WHM	Weighted Harmonic Mean

Subscripts

0	Initial value
∞	far field condition
c	Critical value
l	Liquid
max	Maximum value
sat	Saturation property
t	Temporal derivative
tot	total value
v	Vapor

Superscripts

$n, n+1$	time levels

Chapter 1

Introduction

Boiling of liquids over a heated surface is one of the most frequently occuring phenomena in industrial and domestic applications. The phase-change process during boiling leads to high latent heat transfer rate, which makes the process especially useful in applications demanding high heat transfer rates. In HVAC-R (Heating, Ventilation, Air-conditioning and Refrigeration) systems, performance of devices involving phase change is crucial in meeting efficiency standards with low cost and environmental impact. The phenomenon of boiling is extremely intricate starting from its inception due to convective heating of the liquid to the generation of vapor bubbles and the various morphological changes those bubbles go through during the process. The dynamical and the thermal aspects of the process change extensively from nucleate boiling regime to film boiling regime. A transition regime exists between the nucleate and the film boiling regimes which is marked by the sudden decrease of heat flux due to the hindrance caused by the thin layer of vapor above the heating surface. All three regimes of boiling have been illustrated through the typical boiling curve as shown in Fig. 1.1.

The initiation of nucleate boiling is marked by the inception of vapor bubbles over the heated surface. As the surface temperature increases, the number of active nucleating sites increases with an increase in heat transfer rate. With a further increase in surface temperature, vapor columns are formed and adjacent bubbles start merging. The merger of bubbles eventually leads to the formation of a thin vapor layer switching the boiling mode from nucleate to film boiling. This is marked by a significant drop in the heat transfer rate and the hydrodynamic behavior of

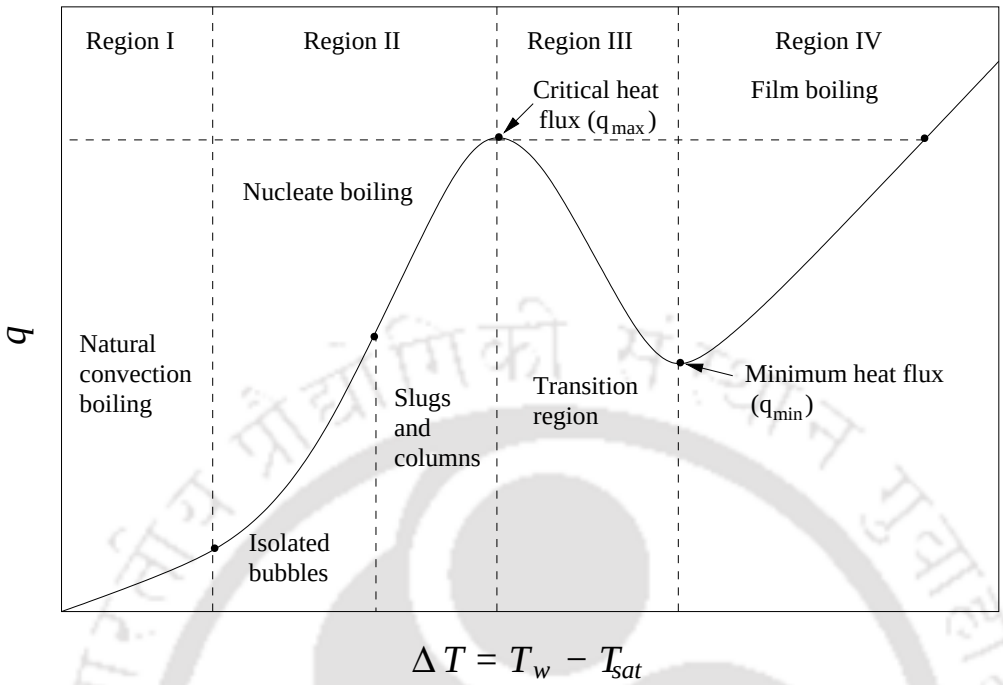

Figure 1.1: Pool boiling curve for saturated water

the vapor bubbles. The vapor bubbles are formed at random nucleating sites during nucleate boiling. Film boiling is governed by the instabilty at the liquid-vapor interface with a preffered separation distance between adjacent bubbles.

1.1 Film Boiling Regime

The term film boiling corresponds to the boiling regime where the solid surface is completely covered by a thin film of vapor layer. Although undesirable in all heat flux removal processes, this mode of boiling is inevitable in the case of high heat flux applications.

1.1.1 Factors influencing interface growth

Due to the constant evaporation at the liquid-vapor interface, the vapor layer starts growing and deforming as a result of perturbations at the interface. These perturbations leads to the growth of vapor bubbles from the bulk vapor film. The interface growth is thus inhibited by the frequent release of vapor bubbles. A constant vapor layer over the substrate surface is maintained by the balance between vapor

release and vapor generation. Film boiling can be controlled by two parameters, i.e. the wall superheat (ΔT_{sup}) and the subcooling (ΔT_{sub}). The wall superheat, ($\Delta T_{sup} = T_w - T_{sat}$) is the difference between the wall temperature (T_w) and saturation temperature (T_{sat}) and the subcooling, ($\Delta T_{sub} = T_{sat} - T_L$) is the difference between the saturation temperature and the bulk temperature (T_L) of the liquid. When the subcooling is zero, the regime is called as the saturated film boiling; otherwise it is known as subcooled film boiling [2].

Growth of the vapor film due to superheat depends on whether the boiling is saturated film boiling or subcooled film boiling. In subcooled film boiling, the stationary film thickness is stable as long as its value is less than a critical value called equilibrium film thickness. As the film thickness grows beyond this critical value, instabilities at the liquid-vapor interface increase. In contrast, saturated film boiling does not experience any steady state and the film thickness grows continuously untill vapor bubble detachment. In saturated film boiling, all the thermal energy transferred from the heated surface to the liquid, through the thin vapor film, is utilized to vaporize the liquid. Vapor bubbles, thus formed, carry the thermal energy from the vapor film to the bulk liquid. Fig.1.2 shows a model for heat transfer in film boiling.

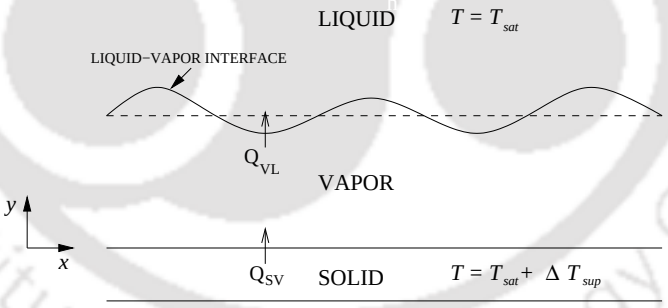

Figure 1.2: Two Dimensional Film Boiling Model

The theoretical development of the study of film boiling suggests various parameters responsible for topological changes in the interface. Some of the major parameters are

- Buoyancy effect : It acts as a destabilising force at the interface and is directly proportional to acceleration due to gravity.
- Surface tension effect : It balances the pressure difference acting at the interface and acts as a stabilising force.

- Vapor thrust : It accounts for the sudden expansion from liquid to vapor during the phase change.
- Heat flux : Heat flux displays bivalent characteristics. It stabilises the film surface initially and at later stages it enhances the instability leading to increased rate of vapor release [3].

1.1.2 Bubble release in film boiling: A deterministic phenomena

The growth and release of vapor bubbles from the thin vapor layer was assumed to be of random nature untill Zuber [4] explained the phenomena using a hydrodynamic analysis. He explained that the bubble formation follows a regular periodic release pattern both in space and time. The bubbles emanate from the interface alternately from nodes and antinodes separated by a distance proportional to the critical wavelength, $\lambda_c = 2\pi\sqrt{\sigma/(\rho_l - \rho_v)g}$, below which every mode of disturbance gets stabilized with time. Here, ρ is density of the medium, σ is the surface tension coefficient, g is the acceleration due to gravity and the subscripts l and v correspond to the liquid and the vapor phase, respectively. Zuber [4] postulated that the diameter, D, of the bubble lies between the critical wavelength and the fastest growing wavelength, $\lambda_0 = 2\pi\sqrt{3\sigma/(\rho_l - \rho_v)g}$, i.e. $\lambda_c < 2D < \lambda_0$. Considering the maximum bubble height to be equal to half of the critical wavelength, the frequency of bubble release was calculated. This provides the expression for a minimum heat flux which is proportional to the product of the fastest growing wavelength and the frequency of bubble release or growth rate (ω) , i.e. $q_{min} \propto \lambda_0\omega$. This hypothesis was purely based on the Rayleigh-Taylor hydrodynamic instability of liquid-vapor interface.

During film boiling on horizontal surfaces, an evaporating liquid mass is supported on a thin vapor layer against the destabilising effect of gravity. This is termed as Rayleigh-Taylor instability. When there is a relative velocity across the interface between two fluids, the instability that results is termed as Kelvin-Helmholtz instability. The vapor also travels horizontally under the liquid layer, to be discharged through the liquid outer boundary in the form of rising bubbles. The vapor velocity can, therefore, result in an instability of the Kelvin-Helmholtz type. It has been observed that the film growth is governed by the Rayleigh-Taylor instability where the lubrication approximation [5] holds good. The Taylor-Helmholtz instability governs

the film growth where inviscid flow approximation is appropriate [6]. The liquid-vapor interfacial instabilities lead to bubble growth and detachment from the vapor film during film boiling.

Zuber [4] studied the film boiling from the instability perspective and provided a relation (called *dispersion relation*) for the frequency of bubble formation depending on various dynamic parameters as,

$$\omega^2 = \frac{\sigma}{\rho_l + \rho_v} m^3 - \frac{(\rho_l - \rho_v)}{\rho_l + \rho_v} gm \tag{1.1}$$

where m is the wave number ($m = 2\pi/\lambda$). The condition $\omega^2 = 0$ implies the limit of the instability growth and the corresponding wavelength obtained is called the 'critical wavelength'. If the value of ω is not real, the disturbance grows exponentially with time. This condition occurs with all modes of disturbances having wavelengths greater than the critical wavelength and among these wavelengths, the one with the highest growth rate is referred to as the fastest growing wavelength.

1.1.3 Electrohydrodynamics in film boiling

The electrohydrodynamics (EHD), as the name suggests is the hydrodynamics in the presence of an electric field. The study considers the effect of the fluid motion on the electric field as well as the influence of the electric field on the fluid motion. The electric field polarises the molecules of the fluid (bound charges) which along with free charges (ions/ electrons) drift towards the free surface [7]. The electric field exerts a force on the charges present at the interface, thus affecting the interfacial stability behavior.

The behavior of the medium in the presence of an electric field depends on its electrical properties like relative electrical permittivity (ϵ) and electrical conductivity (Γ). Based on this, there can be three combinations of the media present across the interface, i.e. dielectric-dielectric, dielectric-conducting and conducting-conducting. The surface forces are normal to the interface in the case of a perfectly dielectric medium whereas in the case of a conducting medium, the tangential component is present too. The nature of the fluid system, whether dielectric or conducting, depends on the relaxation time (time taken by the free charge density to decay in the neighborhood of a given fluid particle), $t^{\mathrm{E}} = \epsilon_0 \epsilon / \Gamma$ and the viscous time scale of fluid motion, $t^{\mathrm{v}} = \rho l_s^2 / \mu$ where ρ and μ are the density and viscosity of the fluid, ϵ_0

is the dielectric permittivity of vacuum and l_s is the characteristic length [8]. This can be mentioned as

- if ($t^{\mathrm{E}} >> t^{\mathrm{v}}$) $\rightarrow$ perfectly dielectric material.
- if ($t^{\mathrm{E}} << t^{\mathrm{v}}$) $\rightarrow$ highly conducting material.

The hydrodynamics of bubble growth is significantly affected by the application of electric field. The extent of influence depends on intensity of the applied electric field. Zuber's [4] dispersion relation (Eq. 1.1) for the frequency of harmonic disturbances was modified by Johnson [9] with the introduction of an additional destabilizing electric field term and extending the hydrodynamic stability theory. The modified dispersion law relating growth rate (ω) and wave number (m) is expressed as

$$\omega^2 = \frac{\sigma}{\rho_l + \rho_v} m^3 - \frac{(\rho_l - \rho_v)}{\rho_l + \rho_v} gm - \frac{f(E, \epsilon_l, \epsilon_v)}{\rho_l + \rho_v} m^2 \tag{1.2}$$

where E is the magnitude of electric field and ϵ is the relative dielectric permittivity. The function f is defined as

$$f(E, \epsilon_l, \epsilon_v) = \frac{\epsilon_l (\epsilon_l - \epsilon_v)^2}{\epsilon_v (\epsilon_l + \epsilon_v)} \epsilon_0 E_l^2 = \frac{\epsilon_v (\epsilon_l - \epsilon_v)^2}{\epsilon_l (\epsilon_l + \epsilon_v)} \epsilon_0 E_v^2 \tag{1.3}$$

The relation for fastest growing wavelength in the presence of an electric field is established as

$$\lambda_J = \frac{6\pi\sigma}{f\left[1 + \sqrt{1 + \frac{3(\rho_l - \rho_v) g\sigma}{f^2}}\right]} \tag{1.4}$$

Jones and Schaeffer [10] also emphasized the effect of a non-uniform electric field on the minimum heat flux in both conducting and highly insulating mediums. Verplaetsen and Berghmans [11] carried out the film boiling experiments over a horizontal surface using electrically conducting medium and with electrically insulating medium [12] to determine the effects of an electric field on the dimensions of the bubbles generated. Nearly constant maximum bubble height was observed in both conducting and insulating medium. They extended the expression of Nusselt number due to Klimenko [13] with inclusion of electric field effect and compared the predictions with their experimental data.

1.1.4 Influence of reduced gravity

Due to large difference in density of the vapor and that of the liquid phases, buoyancy force plays an important role in governing the physics of the two phase flows. Gravity is thus included in most of the empirical correlations for heat transfer in boiling. Change in gravity strongly affects the convection currents and thus the momentum and energy transport during the boiling processes. The main advantage of pool boiling in terrestrial conditions is the inevitable movement of the fluids due to buoyancy. As the gravity is reduced, the phenomenon of phase separation becomes difficult and external power is required for centrifugal or capillarity based flow separators.

Study of reduced gravity on boiling is important in space applications. The space applications demand the study in microgravity or zero gravity conditions while the reduced gravity study is of significance for other terrestrial conditions like in the Martian or Lunar atmosphere. The available techniques for the experimental study under low gravity are executed through drop towers, parabolic flights, sounding rocket flights and orbital flights. Among these, the experiments performed using drop towers are the only ground based techniques.

All the regions on the boiling curve are differently influenced by the reduction in gravity. Studies performed by various authors provided somewhat contradictory results [14, 15] involving heat transfer coefficients in the regime of nucleate boiling. The critical heat flux (CHF) value is found to decrease with the reduction in gravity. In the film boiling region various authors found that the heat transfer coefficient decreases with the reduction in gravity owing to the decrease in bubble release frequency from the vapor film to the bulk liquid.

Many authors concluded the boiling phenomena to have a weak dependence on gravity and found negligible shift in boiling curve through the data obtained from their experiments [15, 16]. Zell et al. [15] observed that film boiling regime is highly influenced by the variation in the level of gravity. However, the boiling curve is negligibly affected due to change in gravity in the nucleate boiling regime. An increase in diameter of bubbles was observed in the case of nucleate boiling though. The experiments on boiling are highly sensitive to the heater geometry, surface roughness, liquid subcooling or liquid pressure. Oka et al. [14] observed a significant deterioration in heat transfer in the low heat flux nucleate boiling for water while there was only a slight change in heat transfer due to reduced gravity

for the organic liquids (CFC-113 and n-pentane). Lienhard [17] pointed out that nucleate boiling in the regime of isolated bubbles is gravity dependent while it is gravity independent in the slugs and column regime of nucleate boiling. Moissis and Berenson [18] provided a correlation for the transition heat flux in the former case of isolated bubbles i.e.

$$q_{(MB)} = 0.11\rho_v h_{lv}(\sigma g/(\rho_l - \rho_v))^{1/4}\gamma^{1/2}. \tag{1.5}$$

Here, γ is the contact angle and h_{lv} is the latent heat of evaporation. While referring to the above correlation, Lienhard [17] gave the correlation for peak heat flux independent of gravity in the slugs and column regime of nucleate boiling as

$$q_{max} = \rho_v h_{lv} u_c (A_j/A_h), \tag{1.6}$$

where A_j is the cross-sectional area of jets, A_h is the heater area and u_c is the vapor velocity in the jets.

The initial studies of the influence of gravity on boiling phenomena can be attributed to the pioneering work by Siegel and coworkers [19–21]. Through the drop towers experiments, they performed various sets of experiments at various values of reduced gravity field mostly in the nucleate boiling regime. Larger bubble diameter, decrease in bubble departure velocity and decreased critical heat flux as the gravity is reduced, were some of the conclusions of their experimental investigations. Contrary to their expectations for the decrease in heat flux in reduced gravity, they observed a significantly comparable value of heat flux with that at the normal gravity. This is attributed to the turbulence generated owing to merger of the smaller bubbles with the already formed large primary bubble.

Merte and Clarke [22] also performed the experiments on fractional gravity and concluded that the heat transfer coefficient in the film boiling region is proportional to $(1/4)^{\text{th}}$ power of the fractional gravity. The same proportionality holds for the maximum and the minimum heat flux values. Lee et al. [23] observed an increase in heat transfer coefficient and significant decrease in maximum heat flux with decreasing gravity in the nucleate boiling regime. They also anticipated the reduction in minimum heat flux value. The heat transfer coefficient is found to be slightly depen-

dent on the degree of subcooling. The heat transfer was governed by the formation of a static large bubble over the surface and the merging of the nearby neighboring bubbles with the larger static bubble.

Unlike the observations of Lee et al. [23], Kim and Benton [24] observed the formation of a larger bubble over the heated surface but it kept on moving over the heater area affecting the heat transfer rate. Heat fluxes obtained in low gravity and high gravity were observed to be greater than at earth's gravity. Raj et al. [25] also performed experiments in the gravity range from 0 to 1.8 times of earth's gravity. They explained the phenomena by differentiating the results in two regimes. First, the low gravity regime where large primary non-departing bubbles are formed and second, high gravity regime where small bubbles continuously depart from the surface. Heat flux is more dependent in low gravity regime as compared to that of the high gravity regime.

The dominant mechanism controlling the dynamics of bubble growth during boiling in low gravity is still a subject of debate. Straub and coworkers [26–28] emphasized on the effect of thermocapillary convection currents owing to the temperature gradient along the interface of the growing bubble. They showed from their experimental and numerical results, the influence of the surface tension force on the heat transfer characteristics of the boiling phenomena. The thermocapillary convection currents resulted in the lateral motion of the bubbles and their merger which maintained the turbulent motion of the detached bubbles. The heat transfer rate in low gravity was found to be equivalent to that in the terrestrial normal gravity condition. They also concluded that the heat transfer reduces significantly in the transition and film boiling regime while it is slightly affected in the nucleate boiling regime. Shatto and Peterson [29] also emphasized on the effect of thermocapillary convection on boiling phenomena.

Qiu and Dhir [30] showed the dynamics of bubble growth during nucleate boiling from bubble inception to lift-off in low gravity environment of parabolic flight. Bubble departure diameter (D_d) was found to be related to the gravity level obeying $D_d \propto 1/\sqrt{g}$. In the case of multiple bubble lift-off after merger, the equivalent diameter was found to be smaller than that of the single bubble at the same gravity level. Abarajith et al. [31] studied the effect of gravity on bubble departure diameter using numerical simulations and showed the same scaling as was observed experimentally by Qiu and Dhir [30]. Although, they showed the dependence on contact angle on the scaling between departure diameter and gravity.

A series of experiments on nucleate boiling was performed at the International Space Station (ISS) by Dhir and coworkers [32–34]. The experimental work was performed following the numerical simulation [33] of single and multiple bubbles in nucleate boiling determining the spacing between the prefabricated heat transfer zones. Experiments were performed in the subcooled and saturated conditions in the microgravity and were compared with the results obtained owing to the earth's gravity. The effect of non-condensable gases was also considered which resulted in local pressure drop at the interface. In the lower heat flux range, lateral bubble merger leads to a single larger bubble which lifts-off as the heat flux is increased. Normalized heat transfer coefficients were found to be weakly dependent on gravity.

Wan and Zhao [35] observed slight enhancement in heat transfer in the low gravity experiments using R113 as fluid using a wire heater while a decrease in heat transfer was observed using plate heater and F72 as fluid. Zhao et al. [36] observed abrupt transition to film boiling from nucleate boiling under the low gravity condition. A decrease in CHF with reduced gravity was also observed.

Verplaetsen and Berghmens [12, 37] studied the effect of electric field on bubble morphology during boiling and observed a tremendous increase in heat transfer coefficient with the application of electric field. Di Marco and Grassi [38] focused on the pool boiling with applied external electric field under low gravity conditions generated through parabolic flights. In the nucleate boiling regime, the effect of both electric field and gravity was mentioned to be negligible [39]. In reduced gravity, the critical heat flux and the heat transfer coefficient in the film boiling regime were appreciably deteriorated. However, both of these were recovered and enhanced with the application of electric field. The electrohydrodynamic (EHD) enhancement of heat transfer during film boiling was observed on both earth's gravity and reduced gravity conditions. At a very high value of electric field, the value of critical heat flux becomes almost indistinguishable on both low gravity and earth's gravity conditions. However, the relative increase in critical heat fluxes as compared to their corresponding values without applied electric field is more in the case of low gravity. The results obtained for the ratio of critical heat flux with electric field to that without electric field were in agreement with the corresponding ratio derived from the hydrodynamic theory by Johnson [9] as

$$\frac{q_{(CHF,E)}}{q_{(CHF,0)}} = \sqrt{\frac{El^* + \sqrt{El^{*2}+3}}{\sqrt{3}}}, \tag{1.7}$$

where El^* is the electric influence number defined as

$$El^* = \frac{f(E, \epsilon_l, \epsilon_v)}{\sqrt{(\rho_l - \rho_v)\sigma g}}, \tag{1.8}$$

with the value of f as given by Eq. 1.3.

$$\frac{\lambda_E}{\lambda_0} = \frac{\sqrt{3}}{El^* + \sqrt{El^{*2}+3}}. \tag{1.9}$$

where λ_E is the wavelenth (distance between two adjacent bubbles) in the presence of an electric field and λ_0 is the wavelength without electric field. Johnson [9] predicted the ratio of heat flux with electric field, $q(E)$ to heat flux without electric field, $q(0)$ in the film boiling regime as

$$\frac{q(E)}{q(0)} = \left[1 + \frac{f}{3[\frac{4}{3}(\rho_l - \rho_v)g\sigma]^{1/2}}\right]^{1/2}. \tag{1.10}$$

The symbols E and 0 refers to the value with electric field and value without electric field, respectively. The electric influence number (El^*) is a function of dielectric permittivities (ϵ) of the media and the electric field strength. Carrica et al. [39] performed experiments using R113 in the film boiling regime to determine the changes in bubble release frequency and wavelengths under the influence of electric field. The most important feature from their results is the clear evidence of boiling-transition within film boiling regime with the application of electric field. At lower superheat, the electric field enhances the bubble release frequency with the significant decrease in wavelength. At this stage, there is no dominant wavelength indicating the bubble spacing. With further increase in wall superheat, the effect of electric field gets suppressed and bubbles again start to depart with larger diameter and increased dominant wavelength.

Having applied an electric field, Di Marco et al. [40] found the similar transition in low gravity film boiling. The film boiling was found to be very sensitive to the

gravity level at low intensity of electric field while it was insensitive to the gravity level at a very high intensity applied electric field value. In addition to the above mentioned researchers, Markels and Durfee [41], Lovenguth and Hanesian [42] and Cooper [43] have also studied the effect of electric field on boiling phenomenon.

1.2 Nucleate Boiling Regime

In the nucleate boiling regime of the boiling curve, high heat flux can be attained at a lower surface superheat. The phenomena of vapor generation and bubble dynamics in nucleate boiling are governed by a different physics than that in film boiling regime.

Nucleate boiling can be a homogenous boiling due to nucleation inside the bulk fluid or a heterogeneous boiling over a heated surface. The initiation of boiling process, as a result of formation of vapor nuclei over a solid surface is called as heterogeneous nucleate boiling. The growth of a vapor nucleus may start at the location overheated due to the presence of a cavity. The growth of the nucleated bubble depends on the temperature of the superheated liquid over the heating surface. The superheated liquid lies within the region of thermal boundary layer formed as a result of the transient conduction from the heated surface. Once a bubble departs from the surface, the cooler liquid rushes into the space that was earlier occupied by the bubble. A swirling motion of the adjacent bulk liquid develops due to the bubble departure. As a consequence, a finite waiting time is required for the next bubble to nucleate from the same cavity. During this period, the liquid acquires a sufficient energy to sustain the growth of the subsequent bubble [44]. The thermal layer re-develops into the bulk liquid up to a finite distance from the heated surface.

Nucleate boiling depends on the factors such as surface roughness, fluid properties, heat flux at the surface or presence of impurities. Kurihara and Myers [45] performed a series of experiments to determine the effect of surface roughness on the heat transfer coefficient during nucleate boiling. The variations in the slopes in boiling curves for different materials are thus explained. The cavity size needs to be sharp enough to entrap any vapor generated [46]. Various correlations have been given by many researchers [47–50] where the heat transfer coefficients have been related to the hydrodynamics of bubbles and factors such as surface superheat, liquid agitation owing to the convection currents and cavity-density over the sur-

face. Rosenhow's correlation [47] for heat flux was based on the Reynolds number calculated using the departure velocity of the bubble from the surface while in the correlation due to Foster and Zuber [51]; the Reynolds number was based on the radial velocity of the growing bubble. The correlation for departure diameter (D_d) of vapor bubble during nucleate boiling was given by Fritz [52] after balancing the buoyancy force with the capillary forces acting on the bubble as

$$D_d = 0.02008\gamma\sqrt{\sigma/g(\rho_l - \rho_v)}. \tag{1.11}$$

Here, γ is the contact angle of liquid-vapor interface with solid, in degrees. Taking into account the effect of system pressure with the inclusion of vapor density term in the Jacob number ($Ja = \rho_l c_p \Delta T/\rho_v k$), Cole [53] proposed following correlation for the departure diameter,

$$D_d \sim \gamma\sqrt{\sigma/g(\rho_l - \rho_v)}Ja. \tag{1.12}$$

where c_p is the specific heat of the medium.

A study based on the measurement of void fraction of liquid during pool boiling over a vertical wall was performed by Liaw and Dhir [54]. The model conceptualize the presence of three regions above the wall as thermal layer, intermediate region and vapor flow dynamics-dominated region. The effect of surface wettability and variation in the magnitude of heat flux on the void fraction distribution was studied. The dependence of active nucleation site-density on the surface wettabily was determined by Wang and Dhir [55]. For a given heat flux, the fraction of the cavities that nucleate increases with decrease in wettability of the surface. However, the cumulative density of active nucleation site is proportional to the square of the heat flux value for all surfaces considered in the study.

The vapor bubble growth rate can be either inertia controlled or thermal diffusion controlled [56]. Lien [57] mentioned that the interface resistance had a little effect on the bubble growth rate. Lien [57] further observed the growth to be inertia dominated in low pressure range while it is dominated by thermal diffusion in the high pressure range.

1.2.1 Importance of microlayer

The phenomenon of nucleate boiling involves many intricate paradigms starting from the heat transfer mechanisms to bubble dynamics during its initiation, growth and departure. The initiation of the bubble strongly depends on the substrate temperature where the cavity is located. The thin superheated thermal layer formed above the surface at the vicinity of the cavity, accelerates the growth of the bubble. The period of formation of a thermal layer prior to the initiation of the bubble is commonly termed as the waiting period. The waiting period is a strong function of surface superheat, which depends on the magnitude of heat flux from the surface. The phase change at the liquid-vapor interface is a very complex phenomenon to analyze. The heat transferred from the surface contributes in vapor generation through exchange of thermal energy to the vapor bubble. Mechanisms involving heat transfer to the bubble in the case of nucleate boiling are the latent heat exchange from the superheated liquid to the vapor bubble, microlayer evaporation near the contact line and convection currents formed as a result of bubble growth in the vicinity of the liquid-vapor interface.

The surface temperature varies continuously during the life cycle of a bubble. The variation in surface temperature during nucleate boiling was first observed by Moore and Mesler [58]. They interpreted latent heat removal due to the evaporation of the liquid microlayer as the reason for a significant drop in surface temperature. Based on the temperature drop occurred at the surface, they estimated the thickness of the liquid film evaporated from the microlayer, with water as the fluid under the atmospheric pressure. Hendricks and Sharp [59] supported the existence of microlayer stating the temperature fluctuations on the boiling surface to be inconsistent with that due to convection currents alone. Sharp [60] was the first to directly measure the microlayer profile. The thickness-variation of microlayer with time and radius of bubble-base was utilized to determine the contribution of microlayer evaporation on the bubble growth. Following Sharp's interferometry technique, Jawurek [61] performed the similar experiments and also measured the bubble growth rate. Voutsinos and Judd [62] observed the significant contribution of microlayer evaporation on the overall heat transfer rate.

The effect of system pressure on the percentage contribution of microlayer during nucleate boiling was determined by Fath and Judd [63]. At low pressure range, the contribution of microlayer evaporation on the overall heat transfer is found

to be more than that at high pressure range. Cooper and Lloyd [64] performed experiments using toluene and isopropyl alcohol on glass and ceramic materials to determine the effect of microlayer evaporation on the bubble growth rate. They also deduced a correlation to determine the thickness of microlayer at any given point as

$$\delta_{ml} = C\sqrt{(\nu t)}. \tag{1.13}$$

where δ is the microlayer thickness, ν is the kinematic viscosity of liquid and t is the growth-time for the bubble-base to reach the point considered. The thickness of microlayer strongly depends on the liquid property. Several authors [60, 61, 65, 66] have tried to find out the thickness of microlayer through their experiments on boiling of various liquids.

The presence of microlayer underneath the growing bubble has been observed by many authors. However the exact contribution of microlayer evaporation in the heat transfer mechanism for bubble growth has always been a topic of discussion. Micro-layer measurement can be performed through the temperature measurement underneath the bubble using micro thermocouples [58, 59, 64] or through laser interferometry technique [60–62, 67]. Interferometric technique measures the microlayer thickness directly while the surface temperature technique measures the heat flux (microlayer evaporation) directly. For both water and ethanol, the data obtained by the experimental group were in the same range. Voutsinos and Judd [62] obtained the microlayer thicknesses in the same range as that were obtained by Cooper and Lloyd [64]. Jawurek [61] and Sharp [60] obtained the thickness which is an order less than that of Cooper and Lloyd [64]. Koffman and Plesset [67] measured the microlayer thickness for ethanol and water vapor bubbles using laser interferometry. A detailed discussion was given for the interpretation of fringe patterns obtained during interferometry to measure the microlayer thickness. They provided the data for their measurements of microlayer evaporation rate at different radial locations. Using the laser extinction technique, Utaka et al. [66] measured the microlayer thickness for water and ethanol over quartz substrate. A comparison of initial microlayer thickness obtained by Koffman and Plesset [67] was demonstrated by Utaka et al. [66]. A linear relation of initial microlayer thickness (δ_0) with the distance from the cavity center (r_l) was given for water as

$$\delta_{ml0} = 4.46 \times 10^{-3} r_l. \tag{1.14}$$

Lay and Dhir [68] developed a model to determine the shape of the vapor stem which depends on the factors like curvature of the interface, hydrostatic head and disjoining pressure (P_d). The disjoining pressure is the result of the long-range intermolecular forces inside the thin liquid film underneath the bubble. They considered the disjoining pressure as a function of the thickness of microlayer (δ_{ml}) given by

$$P_d = A/\delta_{ml}^2. \tag{1.15}$$

where A is the Hamacker constant which describes the van der Waals interactions forces between microscopic bodies. It is relevant to point out that the expression for Hamacker constant remains valid within the framework of continuum theories applicable for two bulk flat surfaces [69]. It is a function of the dielectric properties of the system and hence the intermolecular interaction between molecules. The forces due to the dipole interactions of the molecules have been neglected in the studies conducted by Lay and Dhir [68]. The stability of the thin films depends on the nature of the fluids (polar or apolar) [70] and is an important factor in controlling the behavior of the films based on the macroscopic phenomena, e.g.,interfacial tensions and contact angles.

The first numerical simulation of nucleate boiling was performed by Lee and Nydahl [71] where the microlayer thickness was considered to be varied with time following the relation given by Cooper and Lloyd [64]. The mass transfer from microlayer was calculated from the change in volume of microlayer with time. Micro-layer evaporation found to provide more than 90 percent energy for bubble growth. Son et al. [72] numerically simulated the growth of a single bubble during nucleate boiling by taking into consideration the effect of microlayer underneath the bubble. The contribution of microlayer evaporation was observed to be more than 20 percent in their results. Study of vertical merger and lateral merger of bubbles during nucleate boiling was studied further by Son et al. [73] and Mukherjee and Dhir [74], respectively. A Lagrangian-Eularian meshless numerical technique was developed by Yoon et al. [75] to simulate the bubble growth during nucleate boiling. Analytical studies were performed by Das et al. [76] and Zhao et al. [77] to understand and demonstrate the effect of microlayer on the heat transfer mechanism during the bubble growth. Kim et al [78] developed an analytical model to explain the growth behavior of bubble at different wettability. A free energy analysis was performed and correlated with the wettability of the surface and concluded that a larger departing bubble

evolves for low surface energy, i.e. the surface that possesses more hydrophobicity.

1.2.2 Influence of liquid subcooling

Subcooling of the bulk liquid above the growing bubble critically governs its growth rate and departure size. After the thermal layer above the heated surface fully develops, the liquid above the layer remains in subcooled state. When the bubble interface crosses the thermal layer, condensation of vapor starts at the interface in contact with the subcooled liquid. Hence having attained a maximum value, a decrease in bubble diameter is expected during the subcooled nucleate boiling [79]. Wu and Dhir [80] observed the same effect through the numerical simulations at various values of gravity-levels. There are different views on the influence of subcooling in the case of nucleate boiling [81–83]. The analytical model presented by Snyder and Robin [84] emphasized a decrease in bubble size after it reaches a maximum value as a consequence of subcooled nucleate boiling in forced convection. A comparison was shown with the experimental results of Gunther [85]. Ibrahim and Judd [86] observed an increase in bubble waiting period upto a certain degree of subcooling after which waiting time decreases constantly with further increase in subcooling. A constant decrease in growth time was observed with subcooling.

A direct measurement of heat transfer during subcooled pool boiling was performed by Demiray and Kim [87] using a refrigerant fluid FC-72. Sliding and oscillating behavior of the bubbles were observed during highly subcooled boiling. Marek and Straub [28] presented the effect of thermocapillary convection during subcooled nucleate boiling in the presence of non-condensable gases. The non-condensable gases affect the growth rate of the bubble owing to its accumulation at the top of the bubble boundary. This induces the temperature gradient along the bubble interface generating the thermocapillary currents around the bubble. Recently, Goel et al. [88] experimentally studied the effect of subcooling at low heat flux values and reported the change in bubble departure diameter with the change in liquid subcooling. The effect of surface orientation on the bubble behavior during its growth was analyzed too. Notwithstanding the existence of a large body of available literature, the effect of subcooling during nucleate boiling is still an open area of research.

1.3 Transition Boiling Regime

As the term suggests, transition boiling is the regime where the boiling mode changes from nucleate to film boiling. More precisely, it is the combination of unstable nucleate boiling and unstable film boiling occurring alternately at the same location over the heating surface [89]. During the transition boiling, the heated surface comes in contact with the liquid intermittently. The heat flux decreases suddenly from the critical value to the minimum film boiling value during the transition period. It is difficult therefore, as experienced by many researchers [90–92] to experimentally measure the minimum heat flux while moving from left to right in the boiling curve. Usually, researchers follow the curve from right to left through the film boiling region; decreasing the heat flux gradually and attain the minimum film temperature value corresponding to the first contact between liquid and solid. If the heat flux is reduced, the vapor generation rate diminishes, causing the film thickness to reduce. Eventually the surrounding liquid starts contacting the solid substrate at certain spots when the heat flux reaches a value corresponding to the minimum film boiling point or the Leidenfrost point [93].

The first experimental investigation of transitional boiling indicating quantitative parametric values was performed by Westwater and Santangelo [94]. They investigated the transition boiling in the form of an unstable vapor film with continuous violent bursts of vapor leading to rupture of the film. It was found that the surrounding liquid again rushes towards the heated surface and is transformed into vapor at the point of contact. Zuber [4] analyzed the problem considering that the bubbles were released from the vapor layer and provided the expression for frequency of bubble release and minimum heat-flux density which were in close agreement with the experimental results of Westwater and Santangelo [94]. Berenson [89] described transition boiling as “a combination of unstable nucleate and unstable film boiling alternating at a given location on the heating surface." Determination of the exact mode of heat transfer during transition regime of boiling was attempted through experiments. The liquid-solid contact was confirmed from the effect of wetting behavior of liquid on the boiling curve. For higher wetting-surface, the minimum film boiling point occurs at a higher superheat.

Based on the assumption of alternate contact of liquid and vapor at a particular point on the solid surface, Bankoff and Mehra [95] calculated the heat-flux from the surface during transition boiling. Bradfield [96] showed the possibility of liquid-solid

contacts in stable film boiling which can be controlled by surface roughness, heat-flux and subcooling of the liquid. The intermittent contacts were found and the phenomenon of explosive evaporation was observed frequently in the experiments while using a rough surface. Factors like external pressure field, suction through the surface or application of electric field were described as the means to propagate and control the liquid-solid contacts during boiling. Kovalev [97] observed the dependence of minimum heat-flux on the wettability of the heating surface. An intermittent fluctuation in heat-flux was observed by Nishikawa et al. [98] at a superheat near the minimum film boiling temperature. The experiments on the liquid-solid contact behavior near the minimum film boiling were subsequently performed by various researchers [91, 99–101]. Witte and Lienhard [102] observed the possibility of existence of two boiling curves differentiated mostly in the transition part of the boiling. Different responses were obtained in the heat-flux versus temperature relationship when the transition regime was approached from the left and the right side of the boiling curve by varying the heat-flux. Such occurrence of dual boiling paths was also studied later by Ramilison and Lienhard [90] and Shoji et al. [103]. Effects of surface wettability and roughness were further investigated [104] and transition boiling heat-flux measurements were performed [105].

The significance of transition boiling phase has become more discernable in some recent applications, such as quenching of metals [106, 107] and in the nuclear reactors [108]. Wettability of the surface plays an important role in the process of transition from film to nucleate boiling. Recently, the effects of superhydrophilicity of surface coupled with the subcooled liquid during quenching have been reported by some researchers. Li et al. [106] showed a significant acceleration in the process of quenching in the case of a superhydrophilic surface as compared to an untreated one. Subcooling of liquid was also found to enhance the cooling rate of the surface by reducing the quenching time. The collapse of vapor film occurs rapidly and frequently in the case of superhydrophilic surface and in subcooled liquid. Increasing the subcooling and hydrophilicity of the surface results in increase in minimum film boiling temperature and minimum heat-flux [109]. Frequent liquid- solid contact during the vapor-film collapse also results in the phenomenon of micro-bubble emission boiling (MEB) observed during experiments performed by Kim et al. [25, 110] and Fan et al. [111]. Kang et al. [112] also analyzed the micro-bubble generation due to liquid-solid contact under subcooled boiling over superhydrophilic surfaces. The subcooled liquid at the adjacent surrounding was found to rush towards the

solid following the collapse of vapor film resulting in liquid-solid contacts. Explosive evaporation occurs at the liquid-solid contact spots due to the sudden contact of liquid with the superheated substrate. The nearby vapor bubbles get destabilized and disintegrate into the small micro-bubbles. However, it has been mentioned by some authors [113, 114] that if the surface temperature is above the homogeneous nucleation limit of the liquid, micro-bubble boiling occurs under highly subcooled liquid even without liquid-solid contact.

Even if the surface temperature exceeds the homogeneous nucleation temperature of the liquid, the vapor-film may collapse if the temperature decreases locally at certain spots [115]. Heat transfer coefficient obtained during quenching of metal spheres is much higher in the case of subcooled liquids than in saturated liquid conditions [116] and also depends on the characteristics of the surface of the sphere [117].

Very recently, a study was conducted by Kang et al. [118] to analyze the variation in minimum film boiling temperature and minimum heat flux due to the change in Bond number. The Bond number of interest was defined based on the diameter of the sphere under the condition of quenching.

Using periodic pulse heating and thermal relaxation on a thin tungsten wire, Fau et al. [119] studied the boiling regimes from nucleate to film boiling during heating phase and observed the transition boiling regime during the relaxation phase. Sher et al. [120] observed a “golf-ball" like boiling phenomena during the vapor explosion due to liquid-solid contacts where small concave vapor surface forms over the heated sphere during experiments. The deposition of nanoparticles on the surface results in improved surface wettability and increased roughness which in effect result in vigorous liquid-solid interactions and premature collapse of vapor film [25, 110]. Similar studies have been performed by other authors to determine the effect of surface and liquid subcooling on the heat transfer characteristics [121–123].

High intensity of vapor film collapse may lead to vapor explosion as in the case of fuel melting accidents (loss of coolant accidents) in nuclear reactors. Explaining this particular phenomenon, Freud et al. [108] performed experiments using small spheres coated with anti-oxidant layers and provided the correlations for minimum heat-flux based on the sphere size, surface material and subcooling of coolant. Sharon and Burger [92] performed linear stability analyses of thin vapor films over a vertical heated-wall. The study includes the consequence of liquid subcooling and surface tension on determining the minimum film boiling temperature. Their analyses re-

vealed that the film thickness decreased leading to instability at the interface as a result of decrease in heat flux.

1.4 Interface Capturing Techniques

To determine the exact physical behavior of a multiphase flow, the interface location is required to be known at each time step. The Volume of Fluid (VOF) and level-set (LS) methods are the two main approaches generally followed for the interface tracking problems. The VOF approach of Hirt and Nichols [124] utilizes the donor-acceptor flux approximation technique for computing the mass fluxes. The level-set method, first introduced by Osher and Sethian [125], is an interface capturing technique where the front evolves as a solution of a transport equation of the level-set function. This method is further utilised in the works of Sussman et al. [126,127] and Chang et al. [128]. Apart from the above methods, there are other methods available for capturing the interface, namely, front tracking methods, immersed boundary method and phase field methods [129–133]. These methods can also be utilised to capture the interfaces in complex multiphase flows.

In the VOF method, the volume fraction F is defined for each computational cell based on the initial interface geometry [124,134]. The value of F is zero or unity in pure fluid cells. In each two phase cell its value is defined as $0 < F < 1$. The volume fraction is then advected and the interface is reconstructed based on the updated values of the volume fractions. Thus, the *advection* and interface *reconstruction* are the two main features of this method. A separate surface tension model takes care of the surface tension effects. An important property of the VOF method is the conservation of volume of each fluid which makes the method very useful. The discontinuity of the rheological properties at the interface is taken care of by some suitable smoothening technique which facilitates the calculation of interface normal and curvature.

In the level-set method, the interface is defined by a signed distance function of a level-set function ϕ which is positive on one side and negative on the other side of the interface. The interface itself is represented by the zero level of ϕ. The function $\phi(\mathbf{r}, t)$ at a point with position vector $\mathbf{r}$ and at a time instant t assumes values as

the following:

$$\phi(\mathbf{r},t) = \begin{cases} -d & \text{in the gaseous region,} \\ 0 & \text{at the interface,} \\ +d & \text{in the liquid region} \end{cases} \tag{1.16}$$

where $d = d\,(t)$ is the shortest distance of the interface from point $\mathbf{r}$.

As ϕ is advected with the flow velocity, it does not remain a distance function at later times. Thus, reinitialisation is required after each time step. An important attribute of the level set method is that the interface is inherently smooth. A coupled level-set and volume of fluid (CLSVOF) method (Sussman and Puckett [135]) can be incorporated to blend the properties of both the above methods. In CLSVOF method, the level-set approach is utilised to calculate the interface normal and curvature whereas advection algorithm of VOF is used for volume flux transfer. The present current investigations utilizes the CLSVOF algorithm.

As mentioned earlier, determining the interface location after each time step requires advection and reconstruction methods. The volume fluxes are advected using the advection equation. The reconstruction requires the calculation of the normal vector at the interface which decides its orientation in each computational cell along with the point of intersection of interface with the cell boundaries. There are two approaches which can be used for normal vector calculation. These are the least-square volume-of-fluid interface reconstruction algorithm (LVIRA) approach of Puckett et al. [136], and the CLSVOF approach. The interface can be assumed to be made up of a sequence of segments aligned with the grid. These can be either piecewise constant as in SLIC (simple line interface calculation) by Noh and Woodward [137], constant staircase as in VOF method [124], piecewise linear segments as in PLIC (piecewise linear interface calculation) proposed by Youngs [138] or parabolic segments as in PROST (parabolic reconstruction of surface tension) method [139]. Ashgriz and Poo [140] developed a new technique for interface transport and reconstruction called FLAIR (flux line-segment model for advection and interface reconstruction) in which the interface is represented by a set of line segments defined at the boundary of every two neighboring cells. The orientation of the line segment is based only on the volume fractions of the two cells.

In the problems associated with free surfaces, there is always a localised surface force called surface tension, which is an inherent characteristics of material inter-

faces. For modelling the surface tension force generally the continuum surface force (CSF) model (Brackbill et al. [141]) is followed whereas the continuum surface stress (CSS) model [142] can also be used. The local curvature and the interface normal vector are required to be known in advance for calcualtion of surface tension force. This is difficult in the case of discontinuous volume fraction, where ordinary discretisation scheme cannot be applied unless the interaface is made smooth. The interfacial region can be made smooth by involving the volume fraction function with a radially symmetric kernel K_8 as suggested by Williams et al. [143]. The curvature of the interface can be obtained by direct application of ordinary differential schemes in the case of PROST and CLSVOF methods. The capabilities of these three approaches which can be distinguished by their methods to compute surface tension force was tested by Gerlach et al. [144]. The CLSVOF approach was utilised in solving various problems involving interface interactions like droplets coalescence [145], effect of low and normal gravity on bubble dynamics [146], impact of drop on a liquid surface [147] and many other relevant problems . An inconsistent calculation of surface tension force can result if the discontinuity at the interface is not properly taken care of. This may then result in the well-known phenomena of "parasitic currents" [142]. Usually, problems with parasitic currents arise when the fluids with high density ratios are considered.

The authors have followed different approaches for capturing interfaces. VOF approach with piecewise linear segments for interface representation has been important in studies having complex morphological changes. Level-set method provides smooth changes in properties at the interface but lack mass conservation behavior. The operations of interface reconstruction and advection are crucial in determining the overall accuracy of the computations. CLSVOF approach has been found to acquire the advantages of both mass conservation and accurate tracking of interfaces involving extreme deformation and merging.

1.5 Objectives of the Research

The study on boiling phenomena has been performed by various researchers through analytical, experimental and numerical techniques. Based on the literature review, the present thesis focuses on the following topics for the study:

- **Saturated film boiling**

  On the film boiling, earlier analyses have been performed to understand the bubble dynamics and heat transfer during the process. The study performed by Tomar et al. [3] analyzes the effect of electric field on the film boiling. However, there lies a vast scope for a detailed numerical study on the effects of superheat and particularly with the aplication of electric field. Therefore, the first objective of the present thesis is to analyze the variations in bubble growth phenomena and associated heat transfer during film boiling. Thereafter, the effect of electric field has been studied to focus on and confirm the analytical and experimental findings of Verplaetsen and Berghmens [12, 37] and Johnson's [9] hypothesis related to bubble geometry and heat flux, respectively. Our analysis is restricted to the dynamics of fluids having uniform electrical properties, to the cases where electromechanical coupling is confined to the interfaces [148].

- **Nucleate boiling of a single bubble**

  Many researchers have contributed in understanding the phenomena of nucleate boiling. A detailed numerical simulations covering many aspects of the nucleate boiling have been peformed by the research group of Dhir [30,32,72,73]. However, a detailed study on the effects of liquid-subcooling is needed. One of the objectives is therefore associated with the numerical study of a single bubble nucleation over a heated surface and detailed analysis of the effect of liquid subcooling during bubble growth and its dynamics after it is buoyed away from the surface.

- **Wettability induced transition**

  The final objective of the thesis is to analyze the effect of surface wettability during the film boiling. From the open literature, it is observed that the transition from film boiling to nucleate boiling occurs at the instant when the superheat reduces below the value corresponding to minimum heat flux point on the boiling curve. This transition also depends on the surface wettability; high surface wettability leads to fast transition while low surface wettability prohibits such transition to a large extent.

1.6 Layout of the Thesis

Various regimes of boiling have been studied through complete numerical simulations and are presented in the thesis. A detailed introduction to each of the areas covered in the thesis is mentioned in Chapter 1. An elaborate literature survey is included, explaining all the essential aspects of the present study.

In Chapter 2, the numerical formulation for solving the governing equations and the approach for tracking the liquid-vapor interface are outlined. The boundary conditions incorporated in various problems, have been presented and the detailed procedure to model the microlayer during nucleate boiling has also been explained.

In Chapter 3, a systematic study on the effects of superheat and applied electric field on the bubble formation during film boiling is presented. The combined influence of superheat and the electric field on the phenomenon has also been analyzed.

Chapter 4 presents the effects of various levels of gravity on film boiling and variation in heat transfer characteristics. The morphological changes in the interface due to the application of external electric fields with varying levels of gravity have been studied in detail.

Chapter 5 analyzes the growth and departure of a single bubble during nucleate boiling. The effects of substrate superheat and the effects due to liquid subcooling during the bubble growth and after its departure from the surface are presented.

In Chapter 6, a study on the transition of boiling regime from film to nucleate as a result of surface wettability has been performed. The effects of applied electric field on the transition mechanism in the case of hydrophobic surfaces have also been investigated.

Chapter 7 concludes the thesis and presents the scopes for future work based on the outcome of present investigation.

Chapter 2

Formulation and Numerical Modelling

The two-phase system considered here consists of two incompressible homogeneous fluids with a moving interface. In the flows involving such interfacial motion, the incessant phenomenon of bubble growth at the interface occurs over a very small time and length scales. Simulation of flows involving sharp interfaces requires a physical understanding of the forces acting at the interface and then modelling the flow with a proper mathematical rigor. The interface is considered to be a free boundary where the flow variables exhibit discontinuities. The control volume used have spacing Δx and Δy in x and y directions, respectively. A staggered grid arrangement of Harlow and Welch [149] is deployed to locate the velocity and the scalar functions in the computational cell as shown in Fig. 2.1. Here, χ represents the scalar functions like pressure, temperature, volume fraction (F) and level-set function (ϕ).

2.1 Governing Equations

Single fluid formulation considering both liquid and vapor phases as incompressible and homogeneous is followed in the present simulation. The final set of governing equations are written for a two-phase system as

$$\nabla \cdot \mathbf{U} = 0 \tag{2.1}$$

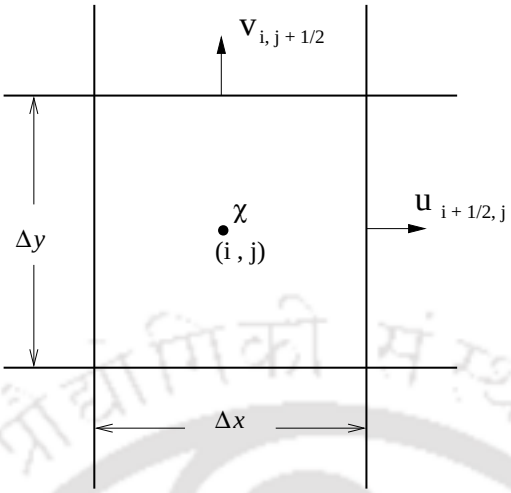

Figure 2.1: MAC grid arrangement

$$\rho\left[\mathbf{U}_t + \nabla\cdot(\mathbf{U}\mathbf{U})\right] = -\nabla p + \rho\mathbf{g} + \nabla\cdot(2\mu\mathbf{D}_v) + \mathbf{f}_{sv} \tag{2.2}$$

$$\frac{\partial T}{\partial t} + \mathbf{U}\cdot\nabla T = \frac{k}{\rho c_p}\nabla^2 T \tag{2.3}$$

where Eqs. 2.1, 2.2 and 2.3 represent mass, momentum and energy conservations, respectively. The term $\mathbf{U} = (u, v)$ is the velocity vector, t is the time, p is the pressure, $\mathbf{g} = (0, -\mathbf{g})$ is the gravitational acceleration, $\mathbf{D}_v = \frac{1}{2}\left\{(\nabla\mathbf{U}) + (\nabla\mathbf{U})^T\right\}$ is the rate of deformation tensor and ρ and μ are the density and viscosity based on the volume fraction function F as

$$\rho(F) = \rho_l F + \rho_v(1 - F) \tag{2.4}$$

$$\mu(F) = \mu_l F + \mu_v(1 - F) \tag{2.5}$$

The subscripts l and v refer to the liquid and vapor phase, respectively. The volume fraction function $F_{i,j}$ is defined on each computational cell (i, j) as the fraction of

the liquid inside a cell.

$$F = \begin{cases} 0 & \text{if gaseous cell} \\ 1 & \text{if liquid cell} \\ 0 < F < 1 & \text{if mixed cell} \end{cases} \tag{2.6}$$

The term $\mathbf{f}_{sv}$ in momentum conservation equation (Eq. 2.2) is the surface tension force per unit volume defined by the continuum surface force model of Brackbill et al. [141] which is explained in detail in Sec. 2.4. In the energy conservation equation (Eq. 2.3), T, k and c_p are the temperature, thermal conductivity and the specific heat of the medium, respectively. For the saturated film boiling case, energy conservation equation is solved only for the vapor phase as the liquid phase is considered to be at constant saturation temperature.

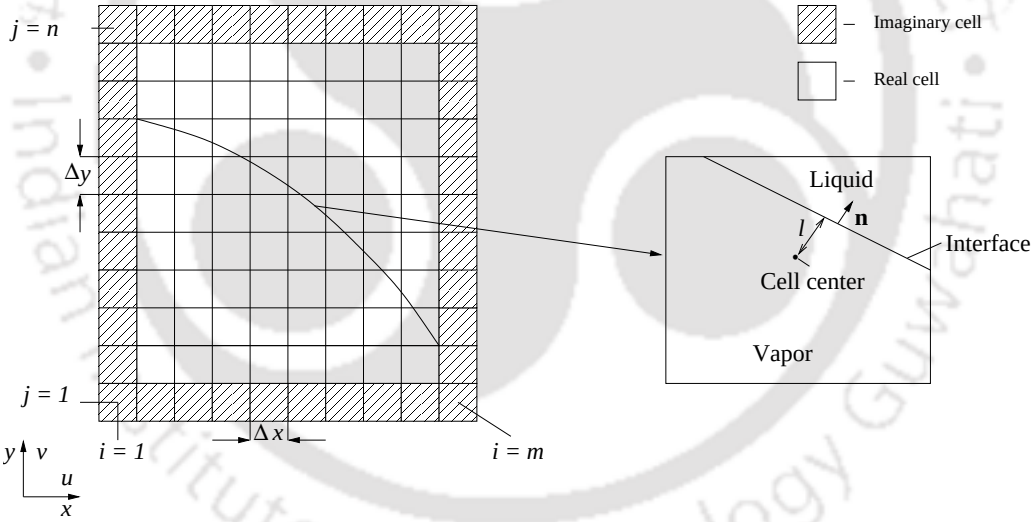

Figure 2.2: Physical domain with fictitious boundary cells and a single two-phase cell in the expanded view. m and n are the number of cells in the x and y directions, respectively.

2.2 Jump Conditions at the Liquid-Vapor Interface

Due to the phase change, there is a mass and energy jump across the liquid-vapor interface [150]. This leads to the jump in normal velocity component which can be

associated with the jump in mass and energy. The mass jump across the interface is given by

$$\|\rho\left(\mathbf{U}-\mathbf{U}_I\right)\|\cdot\hat{\mathbf{n}}=0 \tag{2.7}$$

The mass flux at the interface is

$$\dot{m}=\rho_l(\mathbf{U}_l-\mathbf{U}_I)=-\rho_v(\mathbf{U}_v-\mathbf{U}_I) \tag{2.8}$$

and the energy jump condition is given by

$$\|\rho h_{lv}\left(\mathbf{U}-\mathbf{U}_I\right)\|\cdot\hat{\mathbf{n}}=-\|\mathbf{q}\|\cdot\hat{\mathbf{n}} \tag{2.9}$$

where subscript I denotes the interfacial value and $\mathbf{q}$ and h_{lv} are the heat flux vector and the enthalpy associated with phase change, respectively. From Eqs. 2.7 and 2.9, the jump in normal velocity can be given as

$$\|(\mathbf{U}-\mathbf{U}_l)\|\cdot\hat{\mathbf{n}}=\left(\frac{1}{\rho_l}-\frac{1}{\rho_v}\right)\frac{\|\mathbf{q}\|\cdot\hat{\mathbf{n}}}{h_{lv}} \tag{2.10}$$

The kinetic energy term, viscous work term and the viscous dissipation are neglected in the energy jump condition.

Considering a two-phase computational cell as shown in Fig. 2.2, the mass balance equation for each phase (liquid and vapor) can be written as,

$$\frac{d}{dt}\int_{V_v(t)}\rho\mathrm{dV}+\int_{S_v(t)}\rho\mathbf{U}\cdot\hat{\mathbf{n}}\mathrm{dS}+\int_{S_I(t)}\rho(\mathbf{U}-\mathbf{U}_I)\cdot\hat{\mathbf{n}}\mathrm{dS}=0 \tag{2.11}$$

$$\frac{d}{dt}\int_{V_l(t)}\rho\mathrm{dV}+\int_{S_l(t)}\rho\mathbf{U}\cdot\hat{\mathbf{n}}\mathrm{dS}+\int_{S_I(t)}\rho(\mathbf{U}-\mathbf{U}_I)\cdot\hat{\mathbf{n}}\mathrm{dS}=0 \tag{2.12}$$

where $V_l(t), S_l(t), V_v(t)$ and $S_v(t)$ are the volume and surface area of the cell boundary at the liquid and the vapor region, respectively. $S_I(t)$ is the phase interface at the common boundary of the two regions moving with velocity $\mathbf{U}_I$. The unit normal vector $\hat{\mathbf{n}}$ points into the liquid phase on $S_I(t)$. Now, considering the overall volume

of the cell as time invariant and taking into account the incompressibility of each phase, the conservation of mass equation for the cell volume is given by,

$$\int_{S_C} \mathbf{U} \cdot \hat{\mathbf{n}} \mathrm{dS} + \int_{S_I(t)} \|(\mathbf{U} - \mathbf{U}_l)\| \cdot \hat{\mathbf{n}} \mathrm{dS} = 0 \tag{2.13}$$

where S_C is the boundary of the computational cell. From Eqs. 2.10 and 2.13, the conservation of mass equation in modified form can be written as,

$$\int_{S_C} \mathbf{U} \cdot \hat{\mathbf{n}} \mathrm{dS} + \int_{S_I(t)} \left(\frac{1}{\rho_l} - \frac{1}{\rho_v}\right) \frac{\|\mathbf{q}\| \cdot \hat{\mathbf{n}}}{h_{lv}} = 0 \tag{2.14}$$

2.3 CLSVOF Approach of Interface Capturing

In the CLSVOF algorithm, the transfer of phases from one computational cell to another is calculated based on the volume fraction function. The volume flux is calculated and updated volume fraction obtained facilitates in determining the volume of each phase present in every cell. The level set function, on the other hand defines the geometrical parameters of the interface and its orientation in each computational cell.

2.3.1 Advection algorithm for volume fraction

In the VOF method, since the fluid type remain invariant along the flow, the volume fraction F can be advected with the flow velocity as

$$\frac{\partial F}{\partial t} + \mathbf{U} \cdot \nabla F = 0 \tag{2.15}$$

Using the contunuity equation (Eq. 2.1), it can be written as

$$\frac{\partial F}{\partial t} + \nabla \cdot (\mathbf{U}F) = 0 \tag{2.16}$$

Equation. 2.16 can be discretized by finite differencing methods as

$$F_{i,j}^{n+1} = F_{i,j}^{n} + \frac{\Delta t}{\Delta x}(\delta V_{i-1/2,j} - \delta V_{i+1/2,j}) + \frac{\Delta t}{\Delta y}(\delta V_{i,j-1/2} - \delta V_{i,j+1/2}) \tag{2.17}$$

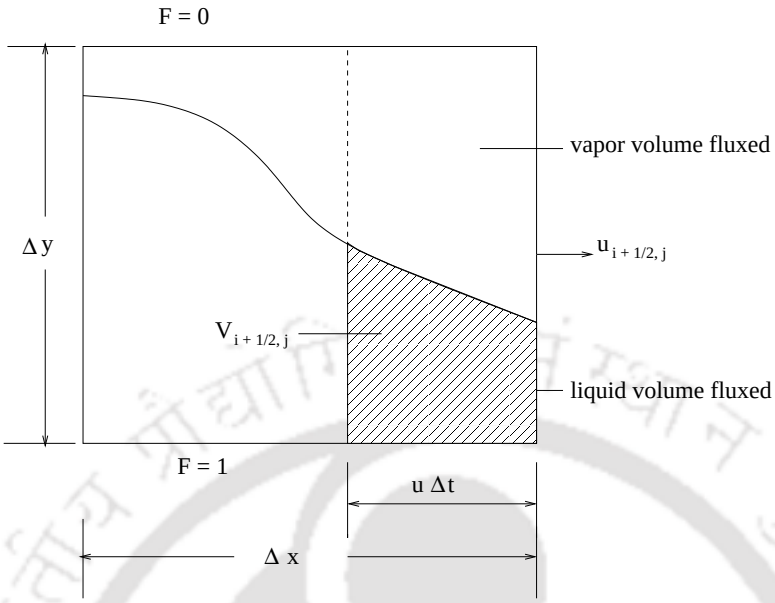

Figure 2.3: Volume fraction fluxed through the righ-face of computational cell.

where $\delta V_{i+1/2,j} = (uF)_{i+1/2,j}$ is the amount of liquid volume fraction fluxed through the right cell face as can be referred to Fig. 2.3. The superscript $(n+1)$ denotes the values at the next time step and $\Delta t, \Delta x$ and Δy are the time step and the grid spacing in x and y direction, respectively. The operator split approach due to Puckett et al. [136] is applied to solve Eq. 2.17 as

$$F^*_{i,j} = F^n_{i,j} + \frac{\Delta t}{\Delta x}(\delta V_{i-1/2,j} - \delta V_{i+1/2,j}) + \frac{\Delta t}{\Delta x} F^*_{i,j}(u_{i+1/2\,,j} - u_{i-1/2\,,j}) \tag{2.18}$$

$$F^{n+1}_{i,j} = F^*_{i,j} + \frac{\Delta t}{\Delta y}(\delta V^*_{i,j-1/2} - \delta V^*_{i,j+1/2}) + \frac{\Delta t}{\Delta y} F^*_{i,j}(v_{i\,,j+1/2} - u_{i\,,j-1/2}) \tag{2.19}$$

Equation. 2.18 is solved implicitly in the first sweep direction whereas Eq. 2.19 in the second sweep direction, is solved explicitly. The star $(*)$ denotes the values obtained after the first sweep. In addition, it can be inferred from Eq. 2.18 and Eq. 2.19 that we are basically solving $\partial F/\partial t + \nabla \cdot (\mathbf{U}F) = F\nabla \cdot \mathbf{U}$, rather than Eq. 2.16 into two equations with the third term on the right hand side of both equations as 'divergence correction' terms.

The volume flux δV in descretised form can be obtained using geometrical based calculation as shown in Fig. 2.3. Knowing the interface position and the velocity in

the two phase control volume, the fluxed volume from the right face can be calculated as

$$\delta V_{i+1/2,j} = \frac{u_{i+1/2,j} V_{i+1/2,j}}{u_{i+1/2,j} \Delta t \Delta y} = \frac{V_{i+1/2,j}}{\Delta t \Delta y} \tag{2.20}$$

Equation. 2.18 can be solved after determining the value of δV from Eq. 2.20 and the interface is again reconstructed based on $F^*_{i,j}$. Same method is followed for the vertical fluxes, calculating geometrically the fluxes of the volume fractions crossing the top and bottom cell face. Hence, the new volume fraction field $F^{n+1}_{i,j}$ is obtained. The procedure can be made second order accurate by alternating the sweep directions at each time step [151].

2.3.2 Advection algorithm for level-set function

In the CLSVOF method, the level set function is used to define the interface geometry and is defined as a distance function from the interface. The advection equation for the level set function is given by

$$\frac{\partial \phi}{\partial t} + \mathbf{U} \cdot \nabla \phi = 0 \tag{2.21}$$

The level set function ϕ is the signed distance function from the reconstructed interface as mentioned in Eq. 1.16. The advection of $\phi_{i,j}$ can be achieved in following steps:

1. The intermediate volume fraction $F^*_{i,j}$ is obtained by solving the Eq. 2.18 in the first sweep direction (x direction).

2. After $F^*_{i,j}$ is obtained, a split form of advection equation (Eq. 2.21) is solved implicitely for ϕ, in the first sweep direction as

$$\frac{\partial \phi}{\partial t} + u \frac{\partial \phi}{\partial x} = 0 \tag{2.22}$$

   The discretization of the convective term in Eq. 2.22 is performed by employing a second order ENO scheme [73, 128].

3. The smoothness of the level set field allows the interface unit normal vector

to be calculated in every two-phase cell by discretizing the following equation using a central finite-differencing scheme

$$\hat{\mathbf{n}} = \frac{\nabla\phi}{|\nabla\phi|} \tag{2.23}$$

The length l (offset distance between cell centre and interface) as shown in Fig. 2.2, is adjusted to match the given volume fraction with that of the reconstructed interface.

4. The final distribution of volume fraction in the current time step ($F_{i,j}^{n+1}$) is obtained by solving ϕ in y direction. After that, the intermediate level set function is advanced in the y direction by solving

$$\frac{\partial\phi}{\partial t} + v\frac{\partial\phi}{\partial y} = 0 \tag{2.24}$$

The discretization scheme is the same as described in step 2.

5. Based on the updated ϕ, the interface is again reconstructed by calculating $\hat{\mathbf{n}}$ and l as in step 3.

6. Due to the advection with the flow, ϕ may not remain a distance function from the interface. For this reason, the level set function has to be reinitialised in all cells based on the reconstructed interface. Reconstruction algorithm due to Sussman et al. [135] is followed for the same.

Second order accuracy for the advection of F and ϕ cane be acheived by changing the the sweeping direction after each time step (as mentioned in Section 2.3.1)

2.3.3 Interface reconstruction

The advection of volume fraction requires the position of the interface to be known at each time step. The interface at every two-phase cell is reconstructed based on the updated values of the level-set functions. In CLSVOF, as the level set function is smoothened across the interface, the normal vector $\hat{\mathbf{n}}_{i,j}$ can be calculated simply by taking the gradient of the level set function at the cell centre as given by Eq. 2.23. Once the normal vector is obtained, the distance $l_{i,j}$ is fixed so as to calculate the

exact values of the volume fraction. The slope of the interface in all the two-phase cells are, thus, obtained and hence the interface can be represneted as a line segment in every two-phase cell.

2.3.4 Smoothening technique

In the VOF method, as the volume fraction changes abruptly and the physical properties undergo sharp jump across the interface, normal finite difference techniques cannot be applied to discretize the spatial derivatives of F which may bring about large inaccuracies in the solution. Therefore, the properties are smoothened in a thin region near the interface as shown in Fig. 2.4. In the surface tension model to follow, the volume fraction is considered as a smoothened color function along a transition region.

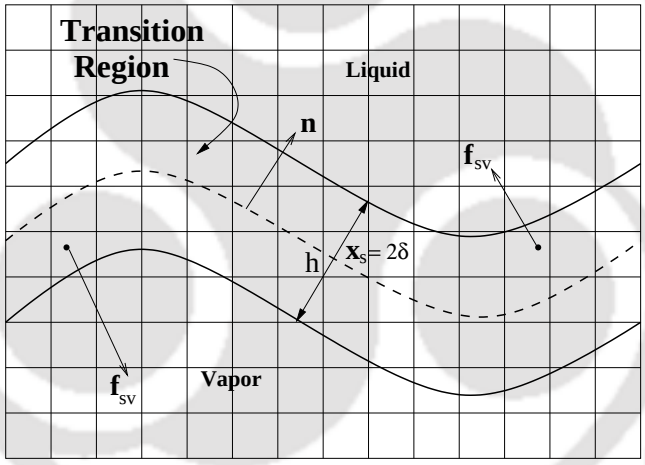

Figure 2.4: Transition region around the interface

Interface is defined on the basis of level-set function where $\phi = 0$. Across the interface, the lvel-set function is defined as a normal distance function from the interface, being positive on one (liquid) side while negative on the other (vapor) side. The smooth variation of the level set function in the CLSVOF method facilitates in

defining a smoothed function called Heaviside function H as

$$H(\phi) = \begin{cases} 0 & \text{if } \phi < -\delta \\ \frac{1}{2} + \frac{\phi}{2\delta} + \frac{1}{2\pi}\left[\sin\left(\frac{\pi\phi}{\delta}\right)\right] & \text{if } |\phi| \leq \delta \\ 1 & \text{if } \phi > +\delta \end{cases} \tag{2.25}$$

The normal vector is calculated following Sussman et al. [135] as

$$\mathbf{n} = \nabla H(\phi) \tag{2.26}$$

The curvature κ is then given by

$$\kappa = -\nabla \cdot \hat{\mathbf{n}} = \nabla \cdot \frac{\nabla\phi}{|\nabla\phi|} = -\frac{\phi_y^2\phi_{xx} - 2\phi_x\phi_y\phi_{xy} + \phi_x^2\phi_{yy}}{(\phi_x^2 + \phi_y^2)^{3/2}} \tag{2.27}$$

2.4 Surface Tension Model

The complex morphological changes during the merging or deformation of interface require an efficient modelling of surface tension. In the present work, we adopted the surface tension model due to Brackbill et al. [141] called as continuum surface force (CSF) model. The interfacial surface area force $\mathbf{f}_{sa}$, in general, is defined as

$$\mathbf{f}_{sa} = \mathbf{f}_{sa}^{\mathrm{n}} + \mathbf{f}_{sa}^{\mathrm{t}} \tag{2.28}$$

where subscript n and t denote the normal and tangential components. These components are then defined as $\mathbf{f}_{sa}^{\mathrm{n}} = \sigma\kappa\hat{\mathbf{n}}$ and $\mathbf{f}_{sa}^{\mathrm{t}} = \nabla_s\sigma$, where σ is the surface tension coefficient, κ is the curvature and ∇_s is the surface gradient. Hence,

$$\mathbf{f}_{sa} = \sigma\kappa\hat{\mathbf{n}} + \nabla_s\sigma \tag{2.29}$$

In our study, as we are not taking into consideration the temperature and concentration gradient along the surface, $\nabla_s\sigma$ can be neglected. The surface tension force

per unit volume can be defined as

$$\mathbf{f}_{sv} = \mathbf{f}_{sa}\delta_s \tag{2.30}$$

where δ_s is the Dirac delta function which is zero everywhere except at the interface. Hence, we get

$$\mathbf{f}_{sv} = \sigma\kappa\hat{\mathbf{n}}\delta_s \tag{2.31}$$

2.5 Discretisation of the Governing Equations

The spatial discretization of the governing equations follows the variable locations in the staggard marker and cell (MAC) grid of Harlow and Welch [149] as shown in Fig. 2.1.

The energy equation is discretized as,

$$T^{n+1} = T^n + \left(-\mathbf{U}\cdot\nabla T^{n+1} + \frac{k}{\rho c_p}\nabla^2 T^{n+1}\right)\Delta t \tag{2.32}$$

The convective term in energy equation are discretized by using third order accurate QUICK scheme (Leonard [152]). The temperature field obtained after each time step is deployed to calculate the heat flux at the interface which is utilised in the mass balance equation. The mass transfer rate across the interface depends on the heat flux vector in the normal direction to the interface.

The continuity equation in the bulk region (Eq. 2.1) is discretized as,

$$\nabla\cdot\mathbf{U}^{n+1} = 0 \tag{2.33}$$

and at the interface the mass balance follows Eq. 5.2 to incorporate the mass jump due to evaporation. The discretization of continuity equation at the interface is as,

$$\int_{S_C}\mathbf{U}^{n+1}\cdot\mathbf{n}dS + \int_{S_I(t)}\left(\frac{1}{\rho_l}-\frac{1}{\rho_g}\right)\frac{\|\mathbf{q}^{n+1}\|\cdot\mathbf{n}}{h_{lg}}\mathrm{dS} = 0 \tag{2.34}$$

The discretization of momentum equation is performed as,

$$\mathbf{U}^{n+1} = \mathbf{U}^n + \left(-\nabla \cdot \left(\mathbf{U}^n \mathbf{U}^n\right)\right) \Delta t + \left(\mathbf{g}\right) \Delta t$$
$$+ \left(\frac{\left[-\nabla p^{n+1} + \nabla \cdot 2\mu\left(\phi^n\right) \mathbf{D}_v^n\right] + \sigma\kappa\left(\phi^n\right) \nabla H\left(\phi^n\right)}{\rho\left(\phi^n\right)} \right) \Delta t \tag{2.35}$$

The convevtive terms in the momentum equation are discretized using a second order essentially non-oscillatory (ENO) scheme as described by Chang et al. [128] and the remaining space derivatives are discretized using central differencing.

The discretized form of the momentum equation is solved explicitly for the known volume fraction field F^n which gives rise to an intermediate velocity field that may not be divergence free. The intermediate (provisional) velocity field is substituted into continuity equation. Thus a poisson equation for pressure correction can be formed. The resulting pressure correction equation is solved using the pre-conditioned HYPRE multigrid solver [153]. Making use of the improved pressure field, the velocities are corrected. Using the new velocity field, the advection equation are utilised to obtain the new volume fraction field F^{n+1} and level set function ϕ^{n+1}, which aids in the interface reconstruction. The numerical scheme followed for solving velocity field is thus second order in space and first order in time. The advection algorithm and the explicit treatment of convective terms, leads to the time constraints in the numerical treatment of the problem. The advection algorithm requires the sum of the volume fluxed over the cell faces must be smaller than the total cell volume which gives,

$$\Delta t_c \leq \frac{\Delta x}{2\text{max}(|\mathbf{U}|)} \tag{2.36}$$

Again, the explicit treatment of the surface tension term results in a restriction as given in Brackbill et al. [141] as,

$$\frac{C_\phi \Delta t_s}{\Delta x} < \frac{1}{2} \tag{2.37}$$

where C_ϕ is the capillary wave phase velocity given by,

$$C_\phi = \left[\frac{\sigma\pi}{\Delta x(\rho_l + \rho_v)}\right]^{1/2} \tag{2.38}$$

Thus, the capillary time step limit can be given by,

$$\Delta t_s < \left[\frac{(\rho_l + \rho_v)\Delta x^3}{4\pi\sigma}\right]^{1/2} \tag{2.39}$$

The time step is chosen to be smaller than Δt_c and Δt_s .

2.6 Electrohydrodynamic (EHD) Model

The basic electrical laws associated with the interaction of electric field and the flow field are discussed in this section. The assumptions exclude the negligibly small induced magnetic field due to the low intensity of dynamic current and presence of any external magnetic field. The important relations consists of the irrotationality of electric field **E**,

$$\nabla \times \mathbf{E} = \mathbf{0} \tag{2.40}$$

Considering the medium to be a pure dielectric, the divergence of the electric displacement vector, $\mathbf{D} = \epsilon\epsilon_0\mathbf{E}$ according to Gauss law, in the absence of free charge, becomes zero,

$$\nabla \cdot \mathbf{D} = 0 \tag{2.41}$$

where $\epsilon_0 = 8.85 \times 10^{-12}$ C/Vm is the dielectric permittivity of the vaccum.

Equation 2.41 can be written as

$$\nabla \cdot (\epsilon\epsilon_0\mathbf{E}) = 0 \tag{2.42}$$

and the irrotationality of **E** ($\nabla \times \mathbf{E} = 0$) implies the electric field to be a gradient

of some scalar funcion as

$$\mathbf{E} = -\nabla\psi \tag{2.43}$$

where ψ is the electric potential function. Hence,

$$\nabla \cdot (\epsilon\epsilon_0 \nabla\psi) = 0 \tag{2.44}$$

For a two fluid system with constant electrical permittivities, Eq. 2.44 reduces to a Laplace equation ($\nabla^2\psi = 0$) in each medium.

The application of an electric field, in general results in the electric body force of the form,

$$\mathbf{f}_{\mathrm{v}}^{\mathrm{E}} = q_{\mathrm{v}}\mathbf{E} - \frac{1}{2}E^2\nabla\epsilon_0\epsilon + \frac{1}{2}\nabla\left[E^2\rho\left(\frac{\partial\epsilon_0\epsilon}{\partial\rho}\right)_T\right] \tag{2.45}$$

where the first term on the right hand side is the coulombic force term called electrophoretic force which depends on sign of the electric field and can be assumed to be negligible in the absence of any free charge. The second term on the same side is the result of inhomogeneity of the electric permittivity due to thermal gradient or phase discontinuities and the third term consists of dielectrophoretic and electrostrictive forces. The dielectrophoretic force is the consequence of the non-uniformity of the electric field and the electrostrictive force is due to the non-uniformity of the permittivity associated with the volumetric change in material.

The third term on the right hand side of Eq. 2.45 can be neglected for uniform electric field and the absence of any volumetric change in material. Whereas the first term in the right hand side can be neglected for a perfectly dielectric medium in the absence of any free charge. The final form of electric force can therefore be expressed as,

$$\mathbf{f}_{\mathrm{v}}^{\mathrm{E}} = -\frac{1}{2}E^2\nabla\epsilon_0\epsilon = \nabla\cdot\boldsymbol{\tau}^{\mathrm{E}} \tag{2.46}$$

where $\boldsymbol{\tau}^{\mathrm{E}}$ is the Maxwell stress tensor defined as,

$$\boldsymbol{\tau}^{\mathrm{E}} = \epsilon\epsilon_0\left(\mathbf{EE} - \frac{1}{2}E^2\mathbf{I}\right) \tag{2.47}$$

where $\mathbf{I}$ is the identity tensor.

At the interface there is a continuity of electric potential,

$$\|\psi\| = 0 \tag{2.48}$$

and the normal component of the electric field satisfies the jump condition as

$$\mathbf{n} \cdot \|\epsilon \mathbf{E}\| = 0 \tag{2.49}$$

which implies,

$$\|\epsilon \epsilon_0 \nabla \psi \cdot \mathbf{n}\| = 0 \tag{2.50}$$

The volume force representation of the electric field force Eq. 2.46 for dielectric medium can be given as in Tomar et al. [8] by,

$$\mathbf{f}_{\mathrm{v}}^{\mathrm{E,d}} = \frac{\epsilon_0}{2}\left(\frac{(\mathbf{D}\cdot\mathbf{n})^2}{\epsilon_0^2}\nabla\left(\frac{1}{\epsilon}\right) - (\mathbf{E}\cdot\mathbf{t})^2\nabla\epsilon\right) \tag{2.51}$$

In the limit of vanishing transition region, the above expression can be written as a surface force,

$$\mathbf{f}_{\mathrm{s}}^{\mathrm{E,d}} = \frac{\epsilon_0}{2}\left(\frac{(\mathbf{D}\cdot\mathbf{n})^2}{\epsilon_0^2}\left(\frac{1}{\epsilon_1} - \frac{1}{\epsilon_2}\right) - (\mathbf{E}\cdot\mathbf{t})^2(\epsilon_1 - \epsilon_2)\right)\hat{\mathbf{n}}\delta_s \tag{2.52}$$

where $i = 1, 2$, denotes the different phases and δ_s is the Dirac-delta function. The force balance at the interface considering the pressure difference across interface, viscous stresses, surface tension force and electric stress forces can be given as,

$$p_1 - p_2 = \sigma\kappa + \|\mathbf{n}\cdot(\boldsymbol{\tau}^{\mathrm{v}}\cdot\mathbf{n})\| + \mathbf{f}_{\mathrm{s}}^{\mathrm{E,d}}\cdot\mathbf{n} \tag{2.53}$$

where $\boldsymbol{\tau}^{\mathrm{v}}$ is the viscous stress tensor and $\mathbf{f}_{\mathrm{s}}^{\mathrm{E}}$ is the surface force due to the applied electric field which for perfectly dielectric fluids acts normal to the interface and is given by $\mathbf{f}_{\mathrm{s}}^{\mathrm{E}}\cdot\mathbf{n} = \|\mathbf{n}\cdot(\boldsymbol{\tau}^{\mathrm{E}}\cdot\mathbf{n})\|$. The electric field stress in tangential direction is

zero at the interface and thus the tangential stress balance can be given by

$$\|\mathbf{t} \cdot (\boldsymbol{\tau}^{\mathrm{v}} \cdot \mathbf{n})\| = 0 \tag{2.54}$$

2.6.1 Modified governing equations with EHD

Formulation of the problem is based on the staggard MAC grid with x and y components of electric field located at the vertical and horizontal faces of the computational cells. The electric potential function and permittivity are defined at the cell centre. The modified form of momentum equation with an additional volume force term of electric field force is expressed as,

$$\rho(\mathbf{U}_t + \nabla \cdot \mathbf{U}\mathbf{U}) = -\nabla p + \rho\mathbf{g} + \nabla \cdot (2\mu\mathbf{D}_v) + \mathbf{f}_{\mathrm{sv}} + \mathbf{f}_{\mathrm{v}}^{\mathrm{E}} \tag{2.55}$$

where $\mathbf{f}_{\mathrm{v}}^{\mathrm{E}}$ is the volume force term due to electric field and can be expressed as Eq. 2.51 for a dielectric medium.

2.6.2 Discretisation

The modified momentum equation is discretized in time as,

$$\begin{aligned}\mathbf{U}^{n+1} = \mathbf{U}^n &+ \left(-\nabla \cdot (\mathbf{U}^n\mathbf{U}^n)\right)\delta t + (\mathbf{g})\,\delta t \\ &+ \left(\frac{\left[-\nabla p^{n+1} + \nabla \cdot 2\mu\left(\phi^n\right)\mathbf{D}_v^n\right] + \sigma\kappa\left(\phi^n\right)\nabla H\left(\phi^n\right) + \left\{\mathbf{f}_{\mathrm{v}}^{\mathrm{E}}\right\}^{n+1}}{\rho\left(\phi^n\right)}\right)\delta t\end{aligned} \tag{2.56}$$

The electric field can be obtained by solving the potential function in Eq. 2.44 using pre-conditioned HYPRE multigrid solver [153].

The normal unit vector can be calculated using the Heaviside function as $\hat{\mathbf{n}} = \nabla H_\delta / |\nabla H_\delta|$. The electrical permittivity of the medium can be smoothened in the two-phase cells using weighted arithmetic mean interpolation (WAM) with smooth Heaviside function as,

$$\epsilon\left(\phi\right) = \epsilon_l H(\phi) + \epsilon_v\left(1 - H(\phi)\right) \tag{2.57}$$

or weighted harmonic mean interpolation (WHM) as

$$\frac{1}{\epsilon} = \frac{H(\phi)}{\epsilon_1} + \frac{1 - H(\phi)}{\epsilon_2} \tag{2.58}$$

A comparition of the above two approaches was shown by Tomar et al. [8]. In the present work, we have followed the WHM method for smoothening of permittivity values across the interface.

2.7 Microlayer Modelling for Nucleate Boiling

As discussed in Sec. 1.2, the growth of bubble during nucleate boiling is goverened by the vaporisation at the interface and also due to the evaporation of the thin liquid layer called microlayer existing underneath the bubble.

The physical dimensions of microlayer underneath the growing bubble is in the range of a few micrometers for water [66]. This may require a mesh dimensions for which computation become unaffordable based on the currently available resources. In order to simulate the nucleate boiling, therefore, we need to model the microlayer evaporation separately which can be applied to exhibit the required physical conditions. A schematic of the microlayer dynamics during the bubble lifespan has been shown in the Fig. 2.5. After the bubble nucleation at the surface, it starts growing due to the evaporation at the liquid-vapor interface and microlayer depletion. The depletion of the microlayer starts from the cavity centre where the thickness is minimum. The region where microlayer is completely depleted is referred as the dryout region. The liquid inside the microlayer is almost depleted at the instant corresponding to the time when the maximum base radius is reached. As the bubble grows further, the buoyancy force dominates over the capillary force. As a result, the bubble starts rising at a much faster rate resulting into the retraction of the bubble base towards the cavity centre. The dryout region gets rewetted as a consequence of the shrinking of bubble-base.

In the present work, we adopted the microlayer evaporation model similar to the one developed by Sato et al. [154]. Here, the initial microlayer thickness (δ_{ml0}) is assumed to linearly vary with the radial distance from the cavity centre [66] as

$$\delta_{ml0} = C_0 r_l \tag{2.59}$$

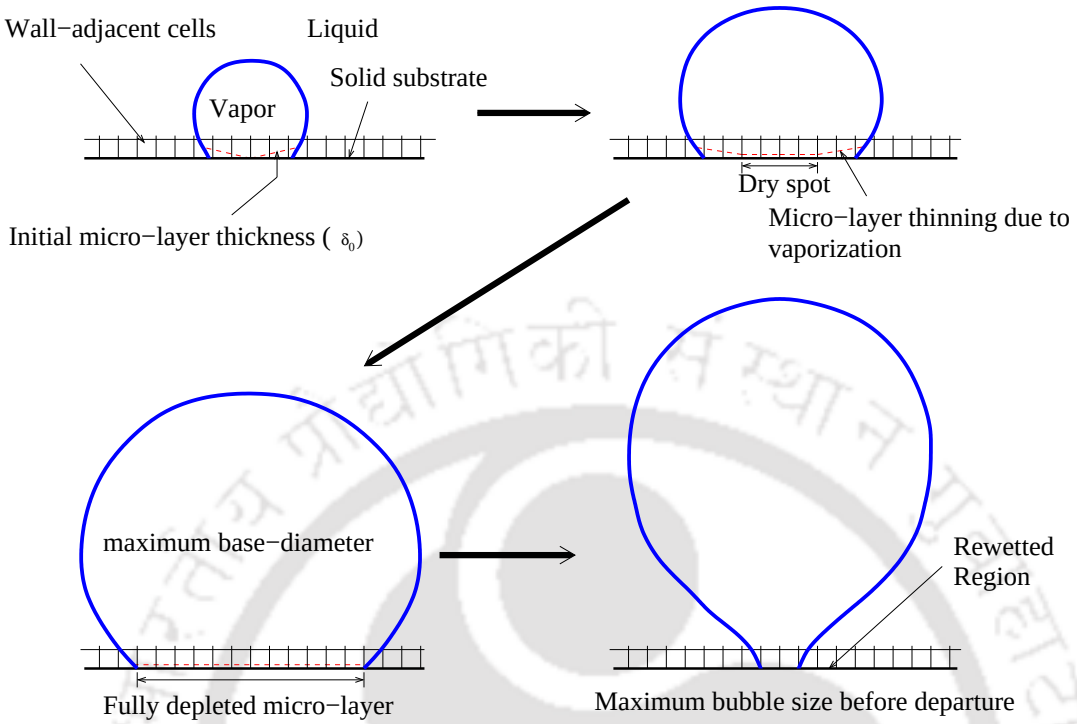

Figure 2.5: Microlayer behavior during bubble lifecycle.

where C_0 is the constant depending on the fluid and substrate combination. The assumptions involved in modelling of microlayer are mentioned below,

1. The liquid inside the microlayer is assumed to be stagnant and hence effect of convection currents on microlayer evaporation is neglected. Thermal energy is conducted purely due to conduction through the microlayer to the vapor bubble.

2. The temperature along the interface between microlayer and vapor bubble is assumed to be equal to the saturation temperature. Similar conditions are applied throughout the liquid-vapor interface.

3. As mentioned earlier, the initial microlayer thickness is a linear function of the radial distance from the cavity centre.

4. An apparent static contact angle has been assumed which is unaffected by the microlayer evaporation throughout the bubble growth period.

The liquid inside the microlayer receives thermal energy through conduction from the superheated wall and evaporates, thereby contributes in vapor mass. The heat

flux through the microlayer is given by

$$q_{ml} = k_l \frac{T_w - T_{sat}}{\delta_{ml}} \tag{2.60}$$

where δ_{ml} is the thickness of the microlayer at the location of the cell considered. The vapor mass flux (m_{ml}) through the interface between microlayer and vapor is thus obtained by

$$m_{ml} = q_{ml}/h_{lv} \tag{2.61}$$

The microlayer thickness changes with time due to evaporation and thus needs to be updated after every time-step of simulation. This is achieved using the relation

$$\frac{d\delta_{ml}}{dt} = -\frac{1}{\rho_l} q_{ml}/h_{lv} \tag{2.62}$$

The above equation is solved explicitly with time. A threshold limit is defined for the minimum microlayer thickness below which the microlayer is considered to be completely dried out. This value in the present simulations has been taken as 1×10^{-10} m.

The same set of governing equations for mass, momentum and energy have been employed in the case of nucleate boiling as in the case of film boiling (Sec. 2.1). The additional mass generation term, as calculated in Eq. 2.61 is incorporated to calculate the velocity jump in the two-phase cells consistent with the modified continuity equation (Eq. 2.10).

2.8 Boundary Conditions

The left and right boundaries are the symmetry boundaries, i.e.

$$\text{at} \quad x = 0 \quad \text{and} \quad x = L: \quad u = 0, \frac{\partial v}{\partial x} = 0, \frac{\partial T}{\partial x} = 0, \frac{\partial F}{\partial x} = 0, \frac{\partial \phi}{\partial x} = 0, \frac{\partial \psi}{\partial x} = 0 \tag{2.63}$$

At the top wall, outflow boundary conditions are used, i.e.

$$\text{at} \quad y = H: \quad \frac{\partial u}{\partial y} = \frac{\partial v}{\partial y} = \frac{\partial T}{\partial y} = \frac{\partial F}{\partial y} = \frac{\partial \phi}{\partial y} = 0; \quad P = P_0 \tag{2.64}$$

where P_0 is the saturation pressure less than the hydrostatic pressure difference from the initial film level to the outlet. No-slip and constant wall superheat boundary conditions are enforced at the bottom wall as

$$\text{at} \quad y = 0 : u = v = 0 \quad \text{and} \quad T = T_{sat} + \Delta T_{sup} \tag{2.65}$$

While solving the film boiling problem, energy equation (Eq. 2.3) is solved in the vapor region alone, as the temperature at the interface and in the liquid phase is fixed as the saturation temperature at the corresponding pressure,i.e.

$$T = T_{sat} \tag{2.66}$$

However, in the case of nucleate boiling, the vapor temperature is considered to be constant and the energy equation is solved in the liquid region alone.

In the simulations performed for film boiling, the domain length along horizontal and vertical directions can be varied whose dimensions are proportional to the most unstable wavelength of Taylor-Helmholtz instability or Berenson's fastest growing wavelength, i.e. λ_B. A uniform grid spacing of $\Delta x = \Delta y = \lambda_B/240$ is used. For the simulations with an applied electric field, a specified intensity of electric field is defined at the top boundary while zero electric potential is applied at the bottom wall.

While solving problems including the wettability of the solid surface, a static contact angle condition at the bottom wall is incorporated as

$$\frac{\partial \phi}{\partial y} = -\cos\gamma. \tag{2.67}$$

Here, γ is the static contact angle between the solid and the liquid-vapor interface.

2.9 Validations of the Solver

The solver used for the present work is capable of tracking intricate interfacial flows along with phase change. The CLSVOF based technique deployed in the present solver, has been found to be highly promising in terms of its applicability and accuracy. This aspect was demonstrated in the work of Gerlach et al. [144]. In the context of the present thesis, some benchmark physical problems related to interfacial flows have been presented below,

1. Rayleigh-Taylor instability

Rayleigh-Taylor instability (RTI) develops owing to any perturbation when a heavier fluid is supported by a lighter fluid. The instability is characterized by the difference in density between the two fluids and the acceleration is directed from the heavier to the lighter fluid. Tryggvason [155] performed numerical simulations considering the fluids to be inviscid and without surface tension to determine the growth rate of perturbation in RTI. Ding et al. [156] performed the similar problem including the viscous effects as in Guermond et al. [157].

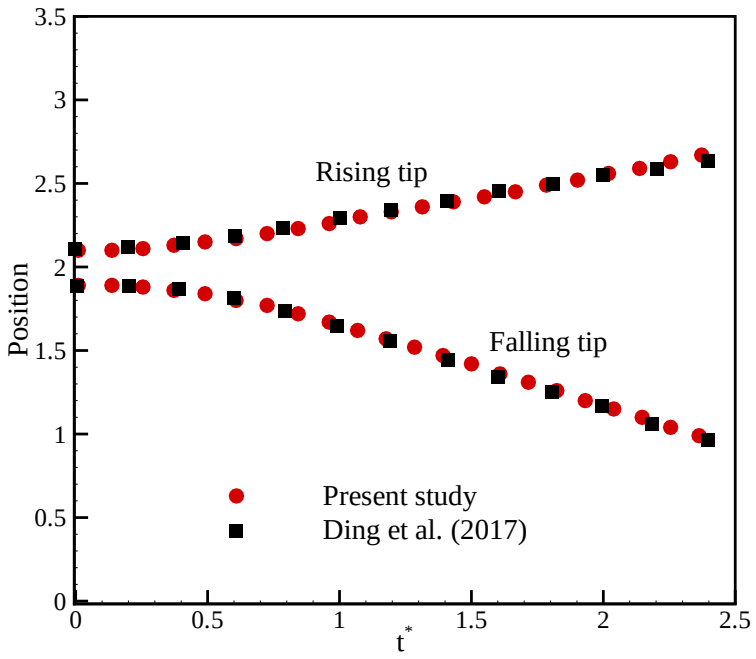

Figure 2.6: Variation of y-coordinate of rising and falling fluid with time.

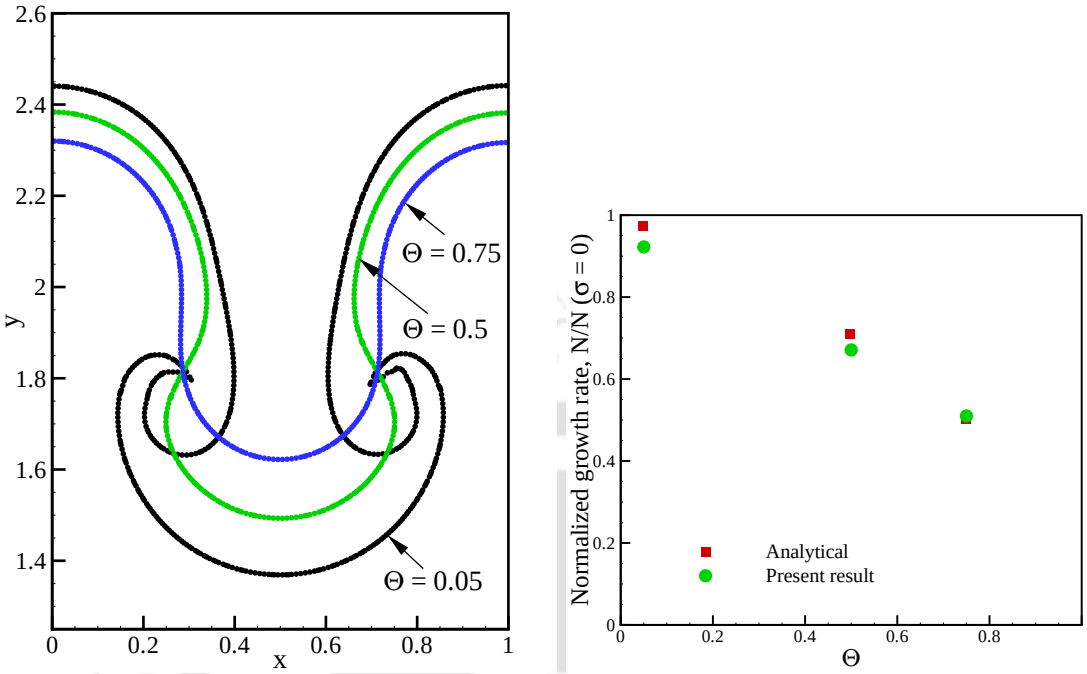

(a) (b)

Figure 2.7: (a) Interface profiles for different values of Θ after the same instant of time and (b) comparison of growth rate with the analytical solution.

Validations are initially performed for the same conditions as in Ding et al. [156] considering the value of Atwood number $\left(At = \frac{\rho_l - \rho_v}{\rho_l + \rho_v}\right)$ as 0.5 and Reynolds number $\left(Re = \frac{\rho_l \sqrt{l^3 g}}{\mu_l}\right)$ as 3000. Intial perturbation of the form, $y(x) = 2d + 0.1d\cos(2\pi x/d)$ having wave number $k = 1$ and amplitude $0.1d$ is given in a domain of size $[0, d] \times [0, 4d]$. The value of d corresponding to $k = 1$ is 2π. A grid-mesh of 100×400 is considered for the simlation. Figure. 2.6 shows the variation of top of the rising fluid and bottom of the falling fluid in the domain and compared with the results of Ding et al. [156]. For normalization, characteristic length scale (l_c) and time scale are chosen as $d = 2\pi$ and $\sqrt{l_c/At.g}$, respectively.

With the included effect of surface tension, the growth rate of perturbation (N) is given by Bellman and Pennington [158] as,

$$N^2 = kg\left[At - \frac{m^2\sigma}{g(\rho_l + \rho_v)}\right] \tag{2.68}$$

A critical value of surface tension (σ_c) can be calculated using Eq. 2.69, for which $N^2 = 0$. Thereby, a dimensionless parameter Θ can be defined following Daly [159] as,

$$\Theta = \frac{\sigma}{\sigma_c} \tag{2.69}$$

such that $\Theta < 1$ implies the growth of instability at the interface. In the present simulations, three diferent values for Θ have been chosen as 0.05, 0.5 and 0.75 and the growth rates obtained have been compared with that obtained from Eq.2.69. Figures.2.7a and 2.7b present the growth rate of perturbation.

The growth rates at different values of Θ are found to be comparable with the analytical values.

2. Hydrodynamic transition in bubble release pattern during film boiling

Mode of vapor release during film boiling varies significantly with the change in superheat of the surface. The variation is more prominently observed near critical pressure where small change in surface superheat may bring about an abrupt change in bubble release mechanism. Reimann and Grigull [1] observed a hydrodynamic transition in bubble release pattern with a change in applied heat flux at the heating surface as illustrated in Fig. 2.8. They observed a variation in bubble release pattern from discrete bubbles at lower values of heat flux to generation of continuous vapor columns at higher values of heat flux. The present results as shown in Fig. 2.9 shows similar transition in interface morphology and vapor release pattern as observed by Reimann and Grigull [1] with increase in superheat of the surface.

Simulations have been performed considering water near critical state (critical pressure of 21.9 MPa). At low value of superheat of ΔT = 10K, discrete bubbles are released alternatively from nodes and antinodes of the critical wavelength which governs the separation distance between adjacent bubbles. With an increase in surface superheat to ΔT = 22K, continuous vapor columns are generated at some of the bubble formation sites while the remaining sites still form discrete vapor bubbles. A further increase in superheat to ΔT = 30K generates vapor columns at all the existing vapor release sites. The change in vapor release

pattern observed in the present simulations have been consistent with the results obtained by Reimann and Grigull [1].

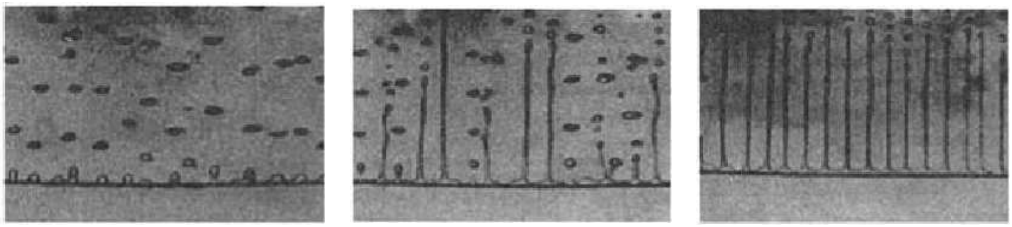

(a) q = 16.21 W/cm^2 (b) q = 21.49 W/cm^2 (c) q = 27.10 W/cm^2

Figure 2.8: Hydrodynamic transition in vapor release observed by Reimann and Grigull [1]

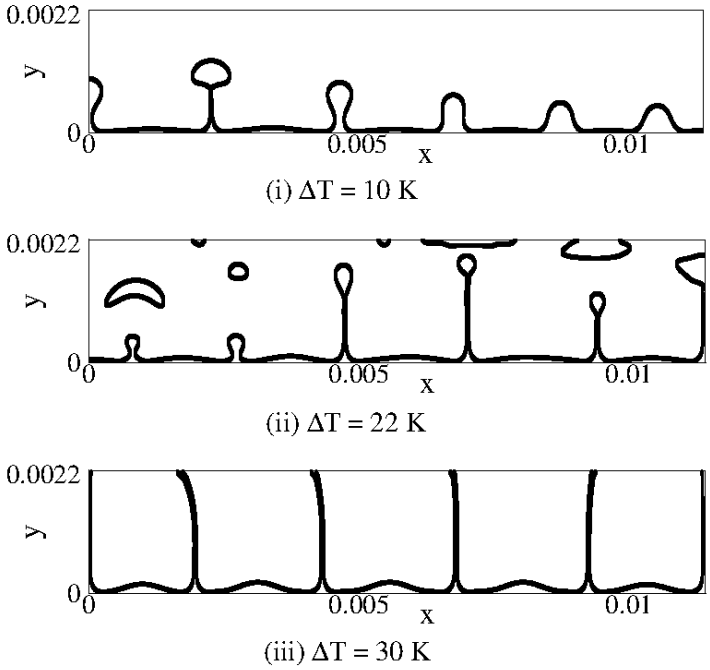

Figure 2.9: Hydrodynamic transition observed through the present numerical simulations.

3. Jump in electric field due to horizontal interface

When an electric potential difference exists across a two-phase interface, a jump in the electric field value occurs as a result of the difference in dielectric permittivity between the media. To numrically calculate the electic field values

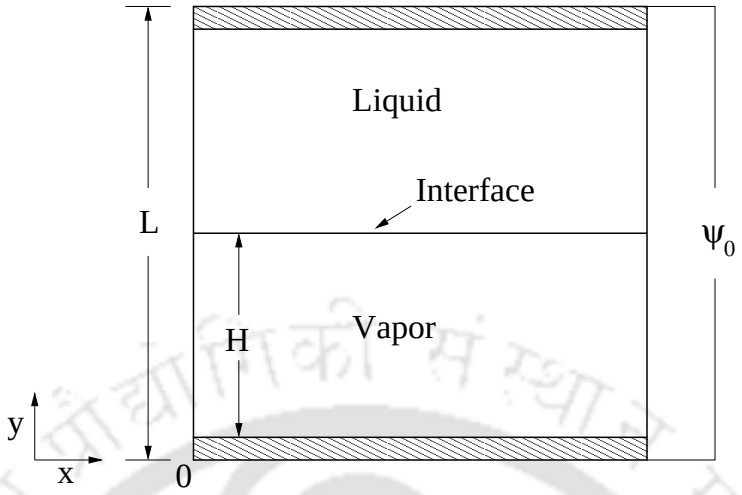

Figure 2.10: Schematic for the flat interface jump problem.

in problems associated with a two-phase interface, it is therefore required to smoothen the dielectric permittivity values in the diffuese region across the interface. The present investigations in the thesis considered the smothening of the dielectric permittivities using the weighted harmonic mean interpolation (WHM) as described in Sec. 2.6.2 through Eq. 2.58.

A motionless liquid-vapor configuration in thermal equilibrium with a flat interface is considered. The schematic of the problem is shown in Fig. 2.10. Properties of water near critical pressure of 21.9 MPa have been considered with the dielectric permittivities values of liquid phase as $\epsilon_l = 7.35$ and vapor phase as $\epsilon_v = 3.71$. The interface is located at $y = H$ in a domain of length L along y direction such that vapor lies in the region $0 < y < H$ and liquid occupies the region $H < y < L$. An electric potential of $\psi_0 = 1.0$ kV is provided at the top boundary while zero electric potential is provided at the bottom boundary.

For a one-dimensional problem, the exact values of uniform electric field in both the liquid and vapor phases can be analytically provided as

$$E_l = -\frac{\psi_0}{\zeta}, \; E_v = -\frac{\epsilon_l}{\epsilon_v}\frac{\psi_0}{\zeta} \tag{2.70}$$

where

$$\zeta = L\left(\frac{\epsilon_l}{\epsilon_v} - 1\right) + H. \tag{2.71}$$

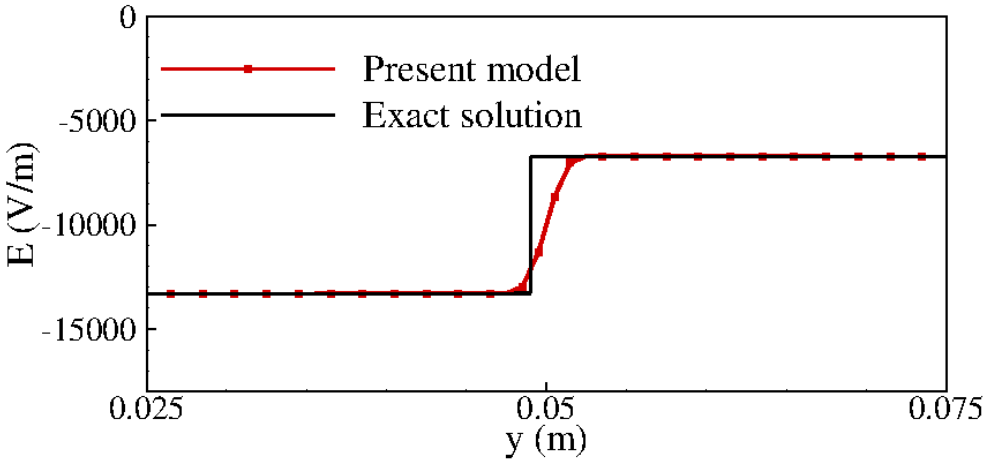

Figure 2.11: Jump in electric field across the interface.

A comparison of the electric field values obtained by solving Eq. 2.51 and that obtain from the exact solution is illustrated in Fig. 2.11. The numerical solution provides the exact values of electric field values in both the media with a smoothening across the interface.

2.10 Summary

A detailed description of the numerical techniques and computational methodology followed in the present work has been presented in this chapter. Techniques involved in the solution of governing equations for mass, momentum and energy conservations have been outlined highlighting complexities associated with the two-phase computational cells due to phase-change. The coupled level set and volume of fluid (CLSVOF) approach for interface capturing has been presented, documenting the procedures of normal and curvature calculations at the interface. A description of microlayer evaporation model required for nucleate boiling has been presented. Boundary conditions involved in the solution of various problems have been introduced and few test-problems to validate the solver have been presented.

Chapter 3

Effect of Superheat and Electric Field on Saturated Film Boiling

The influence of superheat temperature and applied uniform electric field across the liquid-vapor interface during film boiling has been investigated. The hydrodynamics of bubble growth, detachment and its morphological variation with electrohydrodynamic forces are investigated considering the medium to be incompressible, viscous and perfectly dielectric at near critical pressure. The transition in interfacial instability behavior occurs with increase in superheat, the bubble release being periodic both in space and time. Discrete bubble growth occurs at a smaller superheat whereas vapor columns form at the higher superheat values. Destabilization of interfacial motion due to applied electric field, results in decrease in bubble separation distance and increase in bubble release rate culminating in enhanced heat transfer. A comparison of maximum bubble heights owing to application of different intensities of electric field is performed at a smaller superheat. The change in dynamics of bubble growth due to increasing superheat at a high intensity of electric field is studied too. The effect of increasing intensity of electric field on the heat transfer rate at different superheats is determined. The boiling characteristics are found to be influenced significantly above a minimum critical intensity of the electric field.

The contents in this chapter have been published as Pandey, V., Biswas, G., and Dalal, A.,"Effect of superheat and electric field on saturated film boiling", *Physics of Fluids*, 2016, vol. **28**, pp. 052102-1 – 052102-19 (available online, DOI: http://dx.doi.org/10.1063/1.4948545).

3.1 Introduction and Definition of the Problem

The hydrodynamics of film boiling extensively depend on the variation in vapor film thickness along the superheated substrate. The variation in substrate superheat results in changes in the variation of heat transfer rate from solid to the vapor and hence the changes in vapor generation at the liquid-vapor interface. As mentioned in Sec. 1.1.1, the instability at the interface depends on the degree of superheat of the substrate. Therefore, the heat transfer rate and the bubble morphology are also strongly dependent on the magnitude of superheat.

Using the CLSVOF approach, Tomar et al. [160] performed simulations of film boiling, analyzing different modes of bubble growth. They also found the discrete bubble release at lower values of superheat and the columnar growth at higher values of superheat. Study of the frequency of bubble release and the heat transfer analysis was performed using water and R134a as the fluids. The work was extended to multimode analysis [3] of bubble growth and the change in mode of instability from Rayleigh-Taylor to Taylor-Helmholtz with increasing superheat was observed. The nature of interface instability and bubble dynamics with different Jacob numbers was further studied by Hens et al. [161]. They observed the change in flow behavior from laminar to turbulent mode where the periodicity of bubble release was ceased to exist and the columnar structures of bubbles were found interacting and merging with each other.

The numerical simulation of film boiling under the effect of electrohydrodynamic (EHD) forces was performed by Welch and Biswas [162]. The mass transfer model and surface tension model were implemented in CLSVOF algorithm with an electric force term. Tomar et al. [163] also simulated the effect of EHD on film boiling using their method [164] and found an increase in bubble release frequency.

The present analysis utilizes the formulation explained in Chapter 2, to study the influence of a range of electric fields on the bubble growth rate and heat transfer characteristics at different degrees of superheat. The interface is initially perturbed with disturbances of random modes and a random film thickness of small magnitude in y direction. A time step of $\Delta t = 5.0 \times 10^{-6}$ s, which is much below the restrictive capillary time limit is considered in all simulations. A grid dimension of $\Delta x = \lambda_B/240$ has been considered for all the simulations performed.

Single fluid formulation has been followed considering both liquid and vapor phases as incompressible and homogeneous. The physical conditions considered

are at near critical pressure (properties are mentioned in Table 3.1) so that large variation in bubble morphology is brought about by a small increase in the value of superheat. In the bulk vapor or liquid regions, corresponding phase properties are used while at the interface, the properties are calculated using the volume fraction of each phase.

A range of wall-superheats and intensities of electric field have been applied to analyze the changes in interface growth pattern and heat transfer characteristics. In the CLSVOF algorithm, the jump in interfacial properties across the interface is smoothened in a transition region whose thickness is considered to be $\delta = 1.5\Delta x$. The properties of water are taken at near critical pressure, i.e. $P = 0.99P_{sat}$ where the capillary length is $l_s = \sqrt{\sigma/(\rho_l - \rho_v)g} = 2.1 \times 10^{-4}$ m. The value of Berenson's most dominant wavelength [6], $\lambda_B = 2\pi\sqrt{3\sigma/(\rho_l - \rho_v)g}$ is 0.002275 m. The schematic of the computational domain is shown in Fig. 3.1.

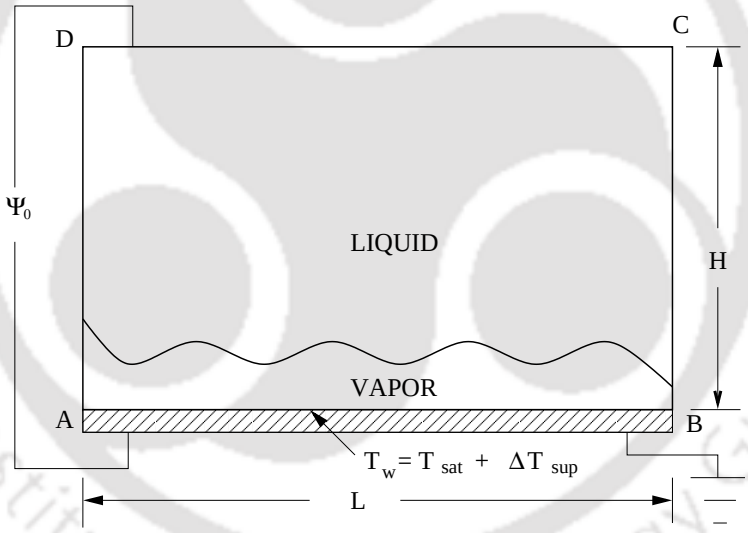

Figure 3.1: Schematic of the computational domain.

Isolated effects of superheat is shown initially to verify the already observed change in instability-mode from lower to higher superheat and then detailed effects of higher superheats are analyzed. The effect of electric field at a given superheat has been studied, in order to observe the change in interfacial morphology and heat transfer characteristics. The effect of electric field on change in bubble deformation is another focus of the current investigation. Various combinations of electric field intensities and superheats have been deployed to analyze the changes in bubble ebullition cycles and variation in heat transfer rates. In this investigation, the

Table 3.1: Properties of water with T_{sat} = 646 K; P_{sat} = 21.9 MPa; h_{lv} = 276.4 kJ/kg; σ = 0.07 mN/m

Phase	ρ (kg/m^3)	μ (N.s/m^2)	k (W/m.K)	c_p (kJ/kg.K)	ϵ
Liquid	402.4	46.7	0.5454	2.18 $\times 10^2$	7.35
Vapor	242.7	32.38	0.5383	3.52 $\times 10^2$	3.71

interface has been captured by CLSVOF approach [144] and the medium has been considered purely dielectric discarding the effect of free charges at the interface. Dielectrophoretic forces have not been considered.

3.2 Grid Refinement Study

A grid independence study has been performed using 80×160, 120×240 and 160×320 grid-meshes. A comparison of the bubble profile at the instant of 2.58 s with a time-step of $\Delta t = 5.0\times10^{-6}$ s is shown in Fig. 3.2. The convergence study is shown for the bubble profiles when the dynamical steady state has been attained. The difference

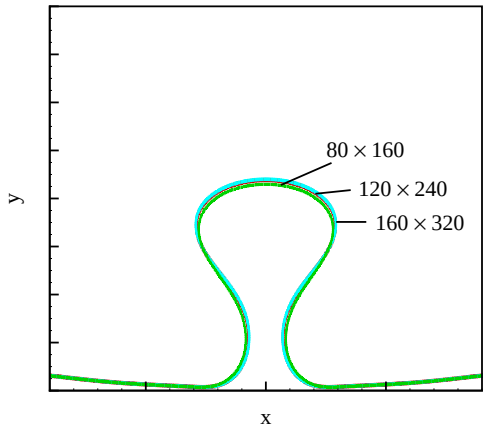

Figure 3.2: Comparison of bubble-profiles at an instant of t = 2.58 s for three different grid-meshes.

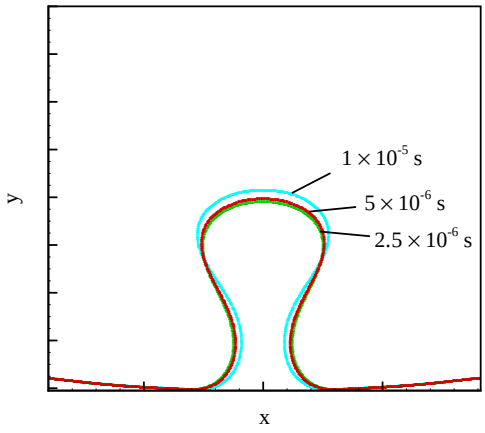

Figure 3.3: Bubble-profiles with a grid mesh of 120 × 240 for three different time-steps.

in maximum height of the bubble predicted using 80 × 160 and 120 × 240 grid-meshes is 1.5 % whereas the difference in predictions using 120 × 240 and 160 × 360 grid-

meshes is 0.14 %. A time convergence study has been performed and shown in Fig. 3.3 for a grid-mesh of 120×240 as a comparison of bubble-profiles at 2.45 s. The time-steps considered are in accordance with the capillary time-step limit (Sec. 2.5). In the present study for film boiling, a grid-mesh of 120×240 and the time-step of $\Delta t = 5.0 \times 10^{-6}$ have been utilized.

The following sections describe distinctly the effect of superheat, effect of electric field and combined effect of varying electric field at different superheat values.

3.3 Effect of Wall Superheat

At near critical pressure, the boiling characteristics change significantly for any fluid with a slight variation in superheat temperature. Simulations have been performed in a domain of size $5\lambda_B \times \lambda_B$ with different degrees of superheat to analyze the changes in interface morphology and bubble formation. The results are shown in Fig. 3.4. The appearance of higher number of bubble formation sites at lower superheat is attributed to the Rayleigh-Taylor mode of instability. The bubble formation sites decrease with increasing superheat which signifies the transformation of the instability-mode to Taylor-Helmholtz as determined earlier by Tomar et al. [3]. Earlier, the same observation has been found experimentally by Hosler and Westwater [165]. Formation of six (6) bubbles in $5\lambda_B$ domain at lower superheat and reduction to five (5) bubbles at higher superheat depicts the change in most dominant wavelength from $\lambda = \sqrt{2}\lambda_c$ to $\lambda = \sqrt{3}\lambda_c$.

The simulations for heat transfer analysis at different superheats are performed in a domain size of $\lambda_B/2 \times \lambda_B$ where an alternate formation of bubbles is observed at the nodes and at the anti-nodes, respectively. The domain length along the x direction is exactly half of Taylor's most dangerous wavelength. A comparison of change in space averaged Nusselt number (Nu) with time for different superheat temperatures is shown in Fig. 3.5. The horizontal line represents the time average of the variation of space averaged Nusselt number. A discrete bubble release pattern is observed up to a superheat of 18 K, above which the the interface grows and forms a vapor column. The variation of space averaged Nusselt number at $\Delta T = 22$ K reveals formation of vapor column. The plot shows no detachment of emanating vapor stream. The peak value of the space averaged Nusselt number decreases with increase in superheat because the minimum distance of the interface from the heated

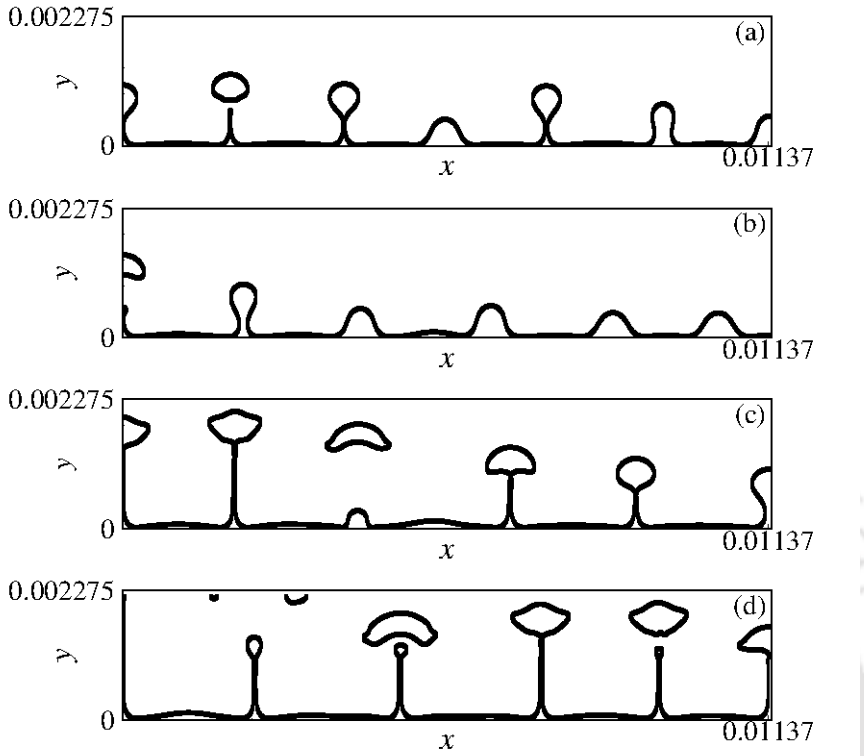

Figure 3.4: Interface morphology for wall superheat of (a) 2 K (b) 5 K (c) 18 K and (d) 22 K .

wall during the course of bubble formation increases with increasing superheat. The temporal frequency of bubble release increases with increase in superheat, as can be observed from the increase in the number of peaks which corresponds to the instants of bubble release. It is observed that the time period of bubble formation decreases from 1.12 s at 2 K to 0.65 s at 5 K and then further decreases to 0.24 s at 18 K superheat. The time averaged Nusselt number value is governed by the maximum peak value and the temporal frequency of bubble growth in the domain. Comparatively higher value of time and space averaged Nusselt number is observed for a superheat of 2 K as compared to the time and space averaged value due to the superheat of 5 K. This is attributed to the higher peak values at 2 K superheat than at 5 K superheat. The time and space averaged Nusselt number value decreases with the increase in superheat up to a certain value of superheat and then it starts increasing with the increase in superheat owing to enhanced temporal frequency (also refer Table 3.3). In the present simulations, the space averaged Nusselt number is

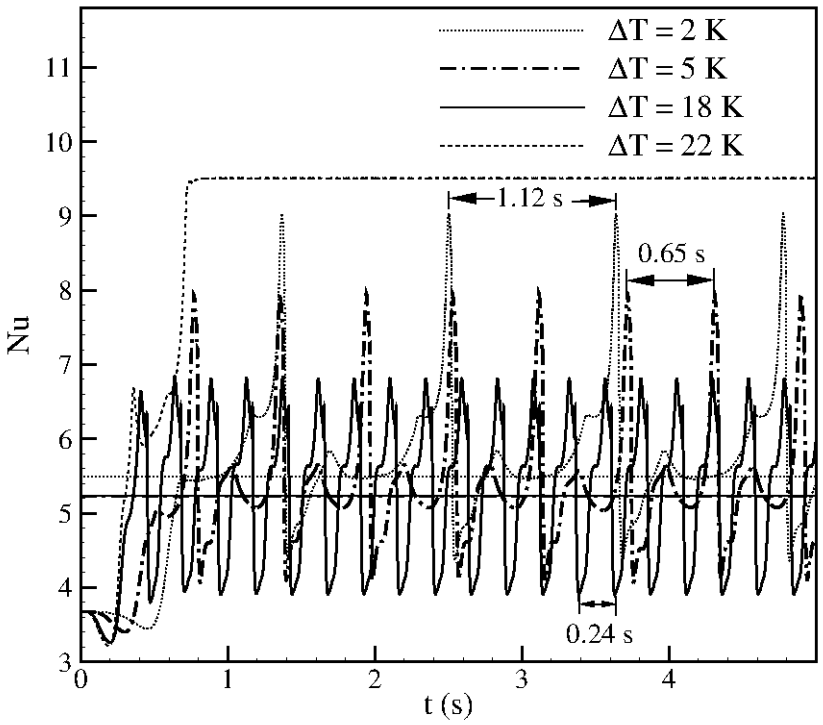

Figure 3.5: Variation of space averaged Nu number at various values of superheat.

calculated as

$$\overline{\mathrm{Nu}_S} = \frac{1}{L}\int_0^L \left(\frac{l_s}{T_s - T_{sat}}\right)\left.\frac{\partial T}{\partial y}\right|_{y=0} \mathrm{dx} \tag{3.1}$$

where L is the horizontal span of domain length, T_s is the surface temperature, T_{sat} is the saturation temperature and $l_s = \sqrt{\frac{\sigma}{(\rho_l - \rho_v)g}}$ is the characteristic length.

The phenomenon of continuous vapor columns formation at the nodes while formation of discrete vapor bubbles at the anti-nodes as observed by Son and Dhir [166], in smaller domain of $\lambda_B/2 \times \lambda_B$, is revealed by our simulation too on a comparatively larger domain of $3\lambda_B \times \lambda_B$. The simulation in the larger domain depicts the influence of the neighboring bubbles on any bubble of interest more prominently. The coalescence and break-up of columns are observed as an additional feature in excess of what was observed by Son and Dhir [166] in smaller domain of $\lambda_B/2 \times \lambda_B$. In Figs. 3.6(a) - 3.6(j), the changes in the bubble growth pattern after the first set of bubble formations are shown. After the column formation on the first set of nodes of the liquid-vapor interface, the columns break-up due to vigorous swirling

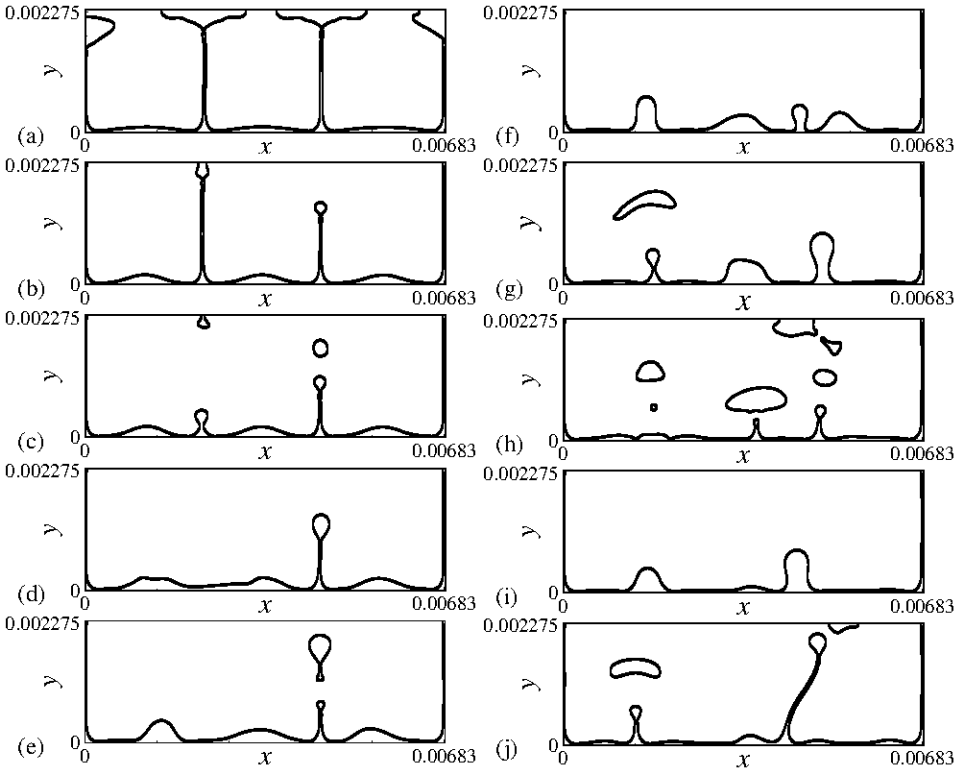

Figure 3.6: Interface morphology with time for 22 K wall superheat at (a) 0.5 s (b) 0.575 s (c) 0.595 s (d) 0.62 s (e) 0.65 s (f) 0.67 s (g) 0.72 s (h) 0.775 s (i) 0.8875 s (j) 0.95 s.

motion of the liquid as seen in Figs. 3.6(a) - 3.6(e). The evolution of the successive set of discrete bubbles at the antinodes can be observed from Figs. 3.6(f) - 3.6(h). The next ebullition cycle of bubble evolution again starts from the nodes followed by the growth of the laterally deformed column growth [Figs. 3.6(i) - 3.6(j)]. A stable vapor column during all these stages is observed at the side walls. This can also referred to be analogous with the experimental observation of Reimann and Grigull [1].

3.4 Effect of Electric Field

The effect of electric field on the bubble release pattern is studied with the application of varying electric field intensities and is shown in Fig. 3.7. At a low intensity of electric field i.e. at 1×10^4 V/m, the number of bubble formation sites does not change significantly. It can be observed that the number of bubble formation

sites increases with further increase in electric field intensity entailing a significant change in bubble morphology. The bubble spacing decreases and bubbles get narrower along the electric field. Without the application of electric field, the interface grows and bubbles emanate following the most dominant wavelength of separation between the adjacent bubbles. With the introduction of electric field, the Maxwell stresses further destabilize the interface and thereby decrease the most dominant wavelength. The decreased wavelength and increased disturbance enhances the spatial frequency of bubble release i.e. the number of bubble formation sites increases for a specified domain.

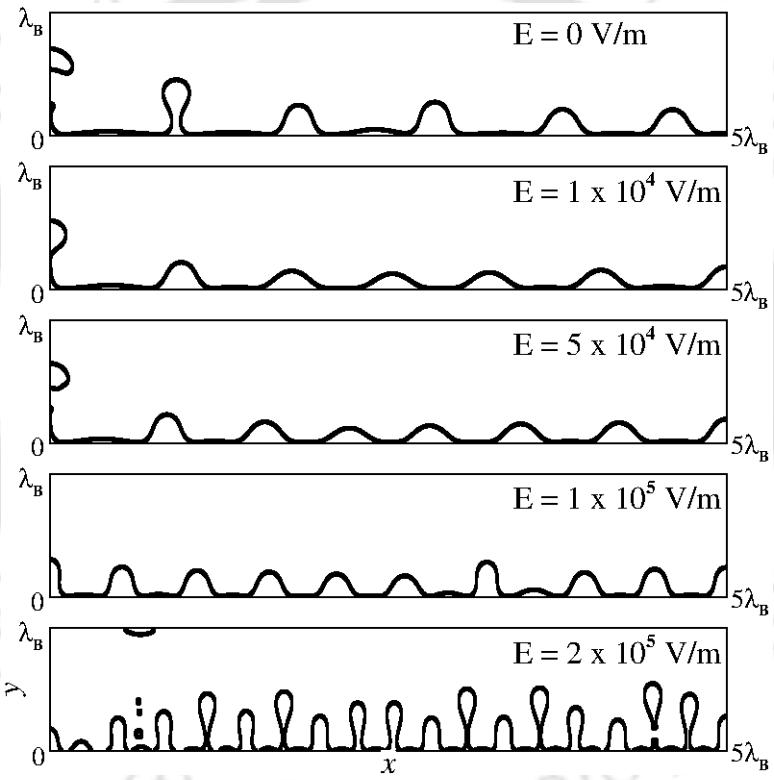

Figure 3.7: Interface profiles for the first set of bubble release with different applied electric field intensities at 5 K superheat.

The effect of electric field on the heat transfer characteristics is shown in Fig. 3.8. For this, the simulations have been performed for smaller domain of size $\lambda_B/2 \times \lambda_B$. At a low electric field intensity (1×10^4 V/m), the change in number of bubble formation sites is negligible. As the intensity of electric field increases, the dominant wavelength decreases and hence the number of bubbles increases on a specified domain length. For a high electric field value (2×10^5 V/m), the wavelength reduces

significantly and the spatial periodicity (i.e. the distance between nodes and anti-nodes) continues to exist revealing the dominance of a particular wavelength. The bubble formation becomes a-periodic in time as can be clearly observed from the space averaged Nusselt number plot in Fig. 3.8. The bubble release becomes rather random or chaotic which leads to an increase in convection currents and thus an increase in the rate of heat transfer.

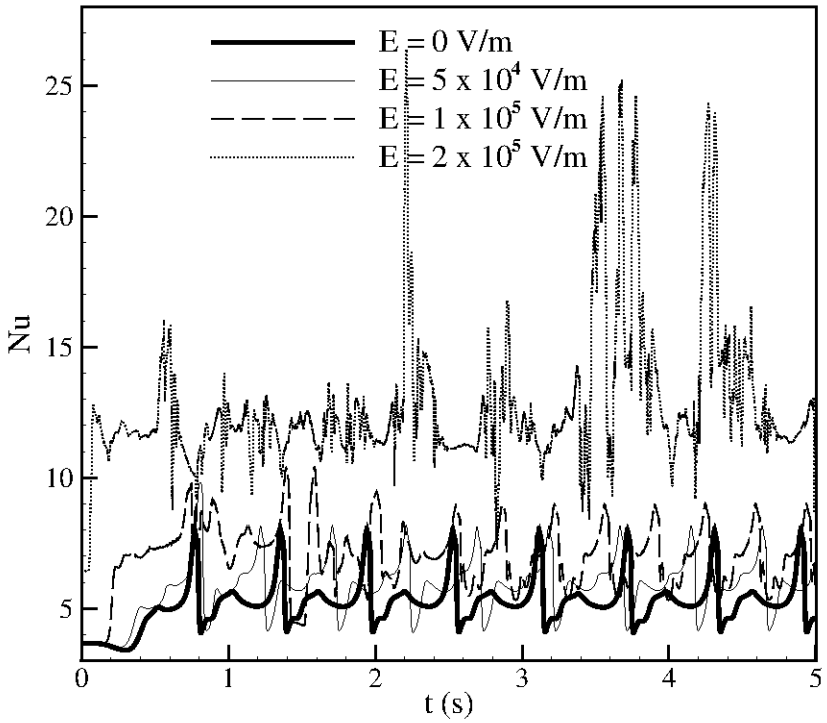

Figure 3.8: Variation of space averaged Nusselt number for 5 K wall superheat and varying electric field intensity.

The comparative analysis of the change in bubble morphology as a function of an applied electric field can be more clearly observed from Fig.3.9. The higher superheat yields more bubbles over a given domain length of $3\lambda_B$. Exactly three bubble formation sites are discerned in absence of an electric field. The number of sites increases to twelve with the application of an electric field of 2×10^5 V/m intensity. The electrodynamic interaction culminate in decreased spacing between adjacent bubbles.

Electric field affects the evolution of interface and the shape of the detached bubbles. Verplaetsen and Berghmans, based on their analytical model [11] and

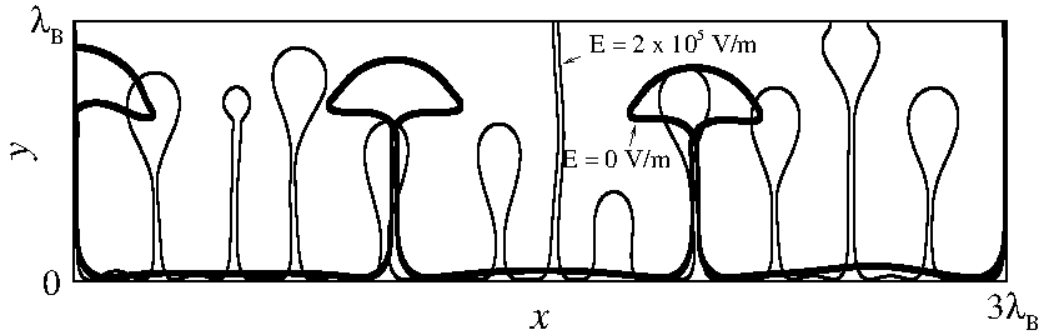

Figure 3.9: Comparison between bubble growth with applied electric field of E = 2×10^5 V/m and without electric field at 40 K superheat.

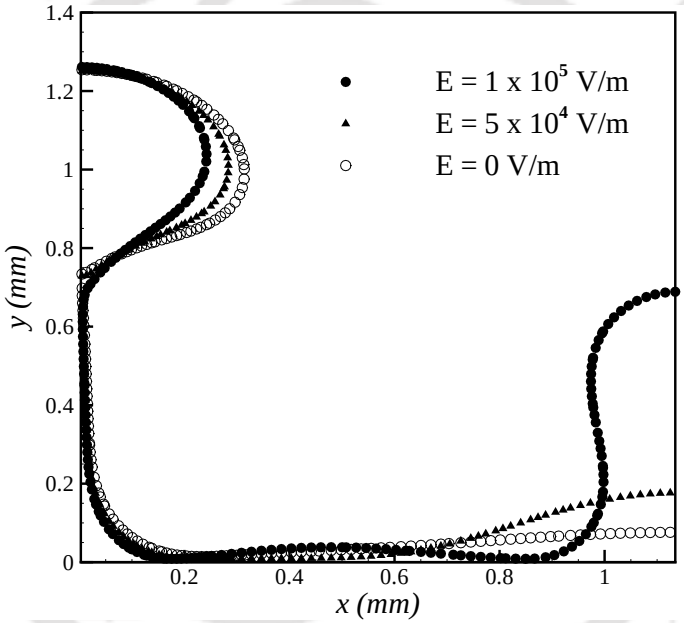

Figure 3.10: Comparison of maximum bubble height at various values of applied electric field and superheat of 5 K.

experimental results [12] showed that the bubbles get elongated as they grow in the presence of additional Maxwell stresses due to the presence of electric field. The height of the bubbles remains practically unchanged but the radius decreases. The resulting effect is brought about by the combined influence of Maxwell stresses and the surface tension force. The Maxwell stress is always directed from the liquid to the vapor while the direction of the surface tension depends on the sign of radius of curvature of the interface [11]. At the top of the bubble, Maxwell stress is very small. At the center of the bubble Maxwell stress and surface tension work in opposite

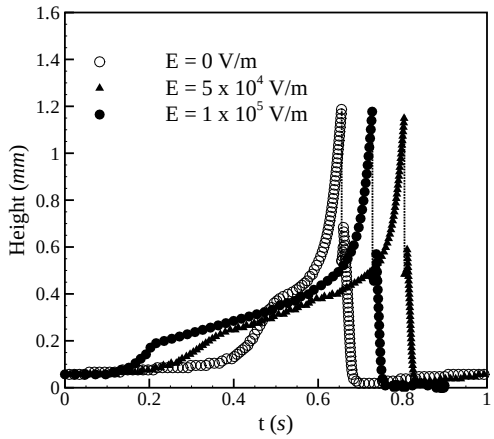

Figure 3.11: Variation of apex height of the bubble with time at 5 K superheat and different values of applied electric field.

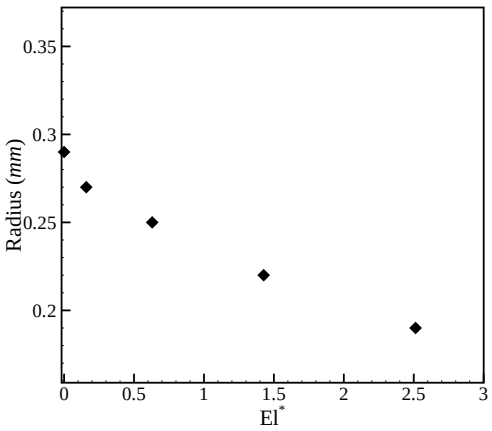

Figure 3.12: Variation of radius of the bubble just after release at 5 K superheat with different values of applied electric field.

directions. Due to the higher Maxwell stress the bubble is contracted at the center. To verify this, we performed simulations in a domain size of $\lambda_B/2 \times \lambda_B$ with varying electric field intensity. The comparison of bubble profiles at a wall superheat of 5 K and with different values of applied electric field is shown in Fig. 3.10. The maximum height just before the bubble release is seen to be almost invariant. The rate of bubble growth at the anti-node is larger with the increasing applied electric field. The growth of bubble at the anti-node, in absence of an electric field is also shown in the figure.

The variation of apex height of the bubbles is also shown in Fig. 3.11 for more illustrative comparison. The figure shows the variation of the apex height of the bubbles under various conditions at the node with time. After a bubble is released from the surface, the vapor left behind experiences a downward force due to surface tension. The agglomeration of vapor drops down and impinges on the horizontal surface. The decreases in the height of recoiling vapor packets with time under various field intensities, are also shown in the figure. The dotted lines indicate the gap between detachment of the bubble and the recoiling state of residual vapor agglomeration. It can also be observed that the bubble volume decreases due to the effect of electric field which has been illustrated in Fig. 3.12. It shows the variation of bubble radii at the instants of detachment for different intensities of electric field.

3.5 Combined Effect of Electric Field and Superheat

The inclusion of electric field results in the decrease in bubble spacing which has already been shown in the previous section for 5 K wall superheat at different values of the electric field. The simulations are performed at higher superheat values too where a different interface dynamics is observed. Application of electric fields yield different effects at different values of superheats. The difference in bubble morphology can be observed from Fig. 3.13 where interface growth at different instants of time is shown for three different values of superheat at a high value of electric field. At a low superheat value, say for 5 K, the bubble growth follows a dominant wavelength which decreases with the increased intensity of electric field and discrete bubble formation is observed. Even for a high intensity of electric field, the bubble growth follows a dominant wavelength. At a low superheat, the formation of small fragments of vapor-packets after the bubble detachment is also observed unlike for the case of without electric field where no such small satellite bubble fragments are formed [Fig. 3.4(b)].

On increasing the superheat value to 18 K, the formation of vapor columns is observed. With the inclusion of a high value of electric field, we observe the increased tendency of bubbles to grow and form continuous vapor columns. Figure

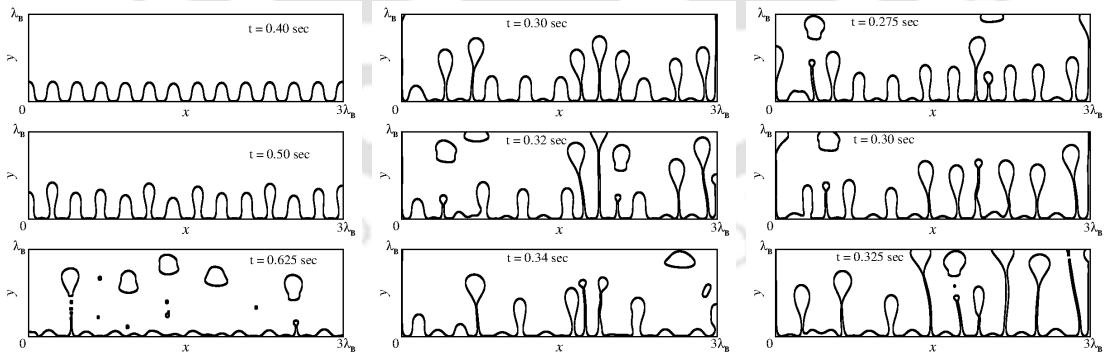

(a) $\Delta T = 5$ K (b) $\Delta T = 18$ K (c) $\Delta T = 22$ K

Figure 3.13: Interface growth for different wall superheat with an applied electric field of intensity 2×10^5 V/m.

3.13(b) shows the increased number of column formation sites. In case of the bubble formation due to 18 K superheat, in absence of electric field, the column formation

sites are less in number [Fig. 3.4(c)]. Similarly for a superheat of 22 K [Fig. 3.13(c)], almost every bubble growth site produces a vapor column that sometimes breaks and merges with another neighboring column. The vapor columns start interacting vigorously and bring about additional perturbations to the interface which disturbs the dominance of a particular wavelength. Hence, for higher values of superheat and at a high value of electric field, the bubble growth is not governed by any dominant wavelength.

A comparison of the growth of first set of bubbles for the cases of with and without electric field at 18 K superheat is shown in Fig. 3.14. There is a considerable decrease in time for the release of first set of bubbles in the case of boiling with electric field. An increased number of bubble formation sites is observed in the presence of applied electric field. A better illustration of the influence of the

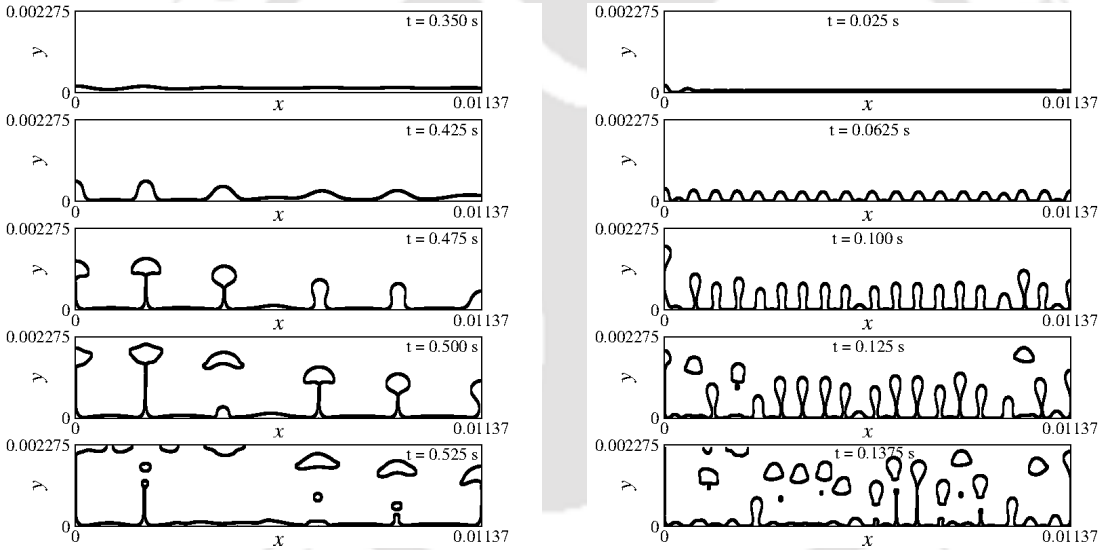

Figure 3.14: Interface evolution for 18 K wall superheat (a) without electric field and (b) with electric field intensity of 2×10^5 V/m.

neighboring liquid adjacent to the emanating bubbles is shown in Fig. 3.15. The streamlines and temperature contours during the first set of bubble release are shown in the figure.

Figure 3.16 shows the variation of space averaged Nusselt number with time for varying electric field intensities at a superheat of 18 K. From the Nusselt number variation, the importance of intensity of the electric field for heat transfer enhancement can be observed. Lower intensity of electric field does not affect the boiling

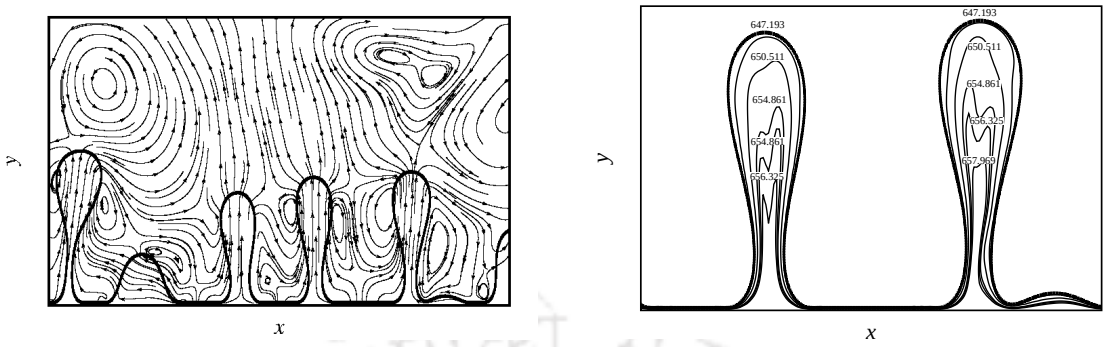

(a) (b)

Figure 3.15: Zoomed view of (a) velocity streamlines and (b) Temperature contours near the bubbles emanating at 18 K wall superheat with applied electric field intensity of 2×10^5 V/m.

characteristics appreciably which can be attributed to the negligible change in frequency of bubble release and the value of Nusselt number. Also, the maximum heat transfer rate is practically unaffected at a lower value of the electric field. As the intensity is increased, the value of Nusselt number and the frequency of bubble release increases. At much higher value of electric field, the bubble release becomes random and thus loses the periodicity. With applied electric field strength of 2×10^5 V/m, the bubbles formed grow at the nodes of instability and subsequently detach and buoy away leaving slender vapor stem which due to the higher electric field, leads to the formation of vapor columns. Owing to the formation of continuous columns, the Nusselt number becomes constant with time. Hence, from the heat transfer perspective we observe that at higher superheat, electric field stimulates the vapor column formation at the bubble formations sites. Although the formation of continuous vapor columns may hinder the heat transfer rate, the increased interaction of the neighboring columns and their subsequent merging and breaking-up promotes heat transfer.

At high value of electric field (3×10^5 V/m) and a moderate value of superheat (5 K), we observe that the interface tends to come in contact with the wall surface leading to the rupture of the vapor film. This may lead to the transition from film boiling to nucleate boiling regime. Whereas for the higher value of superheat (18 K), even though the minimum film thickness is observed to decrease significantly, it never touches the wall surface and the continuous release of bubbles is observed. The above mentioned results can be observed from Fig. 3.17 and Fig. 3.18 where interface

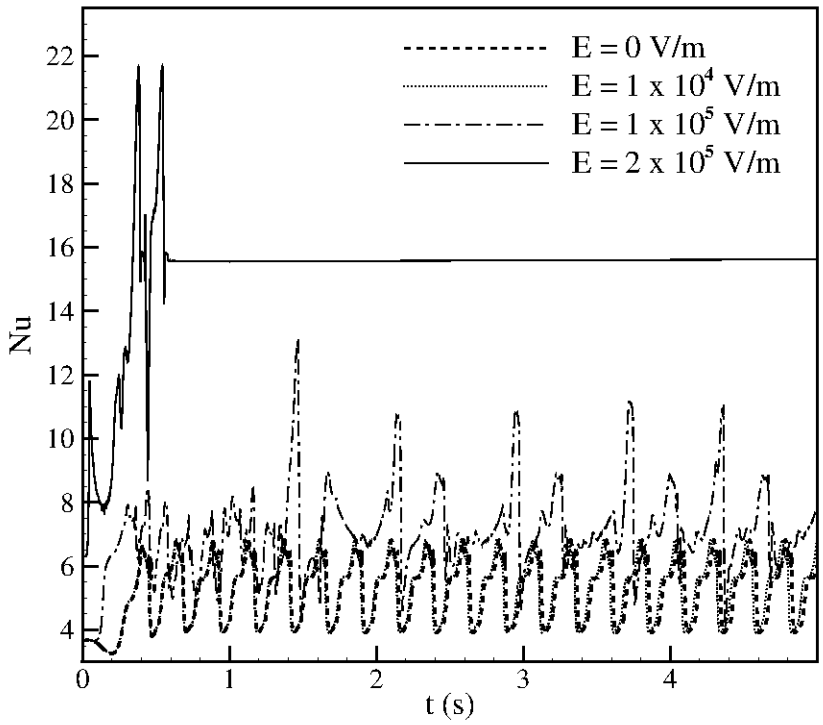

Figure 3.16: Variation of space averaged Nusselt number for 18 K wall superheat and varying electric field intensity.

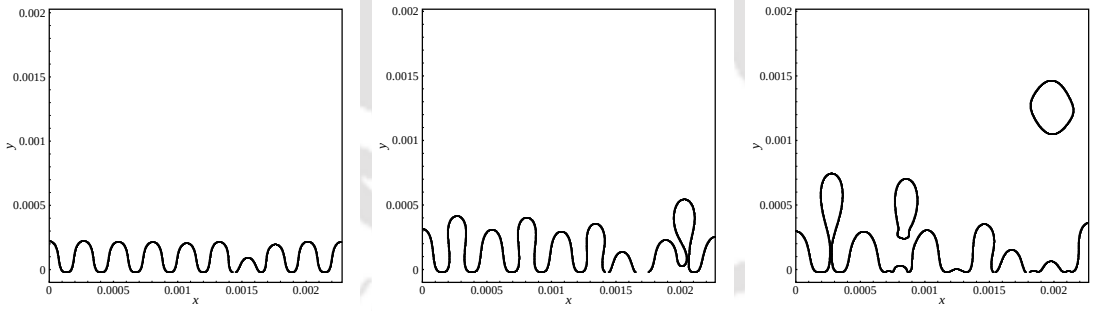

(a) t = 0.150 s (b) t = 0.225 s (c) t = 0.263 s

Figure 3.17: Interface growth for 5 K wall superheat with an applied electric field intensity of 3×10^5 V/m.

growth at three different instants of time is shown for 5 K and 18 K superheat, respectively. The location at $y = 0$ refers to the superheated wall location. These simulations, for 3×10^5 V/m are performed on a domain size of $\lambda_B \times \lambda_B$ and using a fine grid size of $\Delta x = \Delta y = \lambda_B/700$. In the case of 5 K superheat, it is observed that the interface at the anti-nodes flattens leading to its rupture as seen between

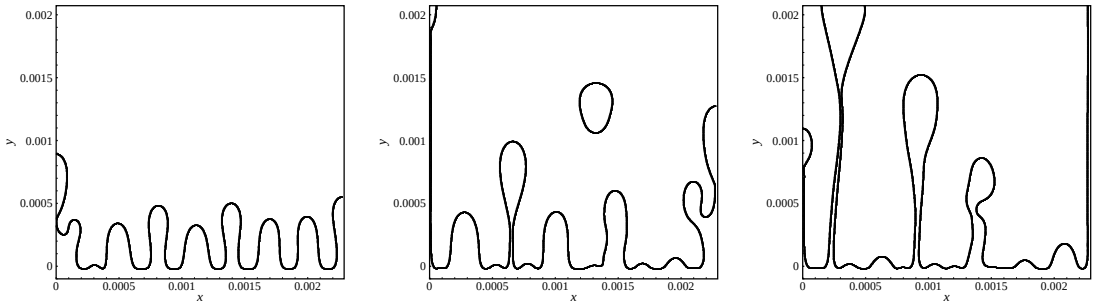

(a) t = 0.130 s (b) t = 0.175 s (c) t = 0.275 s

Figure 3.18: Interface growth for 18 K wall superheat with an applied electric field intensity of 3×10^5 V/m.

$x = 0.001$ m and $x = 0.002$ m.

A detailed comparison of the variation in bubble spacing with applied electric field at different values of superheat is presented in Table 3.2. The ratio of wavelength obtained with electric field to the one obtained without electric field owing to the simulations is compared with their counterparts comprising of analytical values [9]. The theoretical value of wavelength with applied electric field is obtained from Eq. (1.4). The number of bubble formation sites owing to the applied electric fields, found in our simulations is almost same for all the cases. This is because the electric force dominates over the other destabilizing forces and governs the flow behavior.

Johnson [9] postulated that the electric field forces will have noticeable effect on boiling characteristics only above a critical value which can be determined from the magnitude of the term $\frac{3(\rho_l-\rho_v)g\sigma}{f^2}$. Equation (1.4) infers that for the electric field to have significant effect on the bubble spacing, the condition $\frac{3(\rho_l-\rho_v)g\sigma}{f^2} \simeq 1$ is required while the condition $\frac{3(\rho_l-\rho_v)g\sigma}{f^2} >> 1$ refers to almost negligible effect. In the later case the most dominant wavelength without electric field (λ_B) is nearly equal to that of the wavelength obtained with electric field (λ_E), i.e. $\lambda_B \simeq \lambda_E$. This implies the magnitude of the electric field intensity needs to be of appreciable value to bring about a change in heat transfer rate and interface growth. Johnson [9] predicted the ratio of heat flux with electric field, $q(E)$ to heat flux without electric field, $q(0)$ as

$$\frac{q(E)}{q(0)} = \left[1 + \frac{f}{3[\frac{4}{3}(\rho_l - \rho_v)g\sigma]^{1/2}}\right]^{1/2} \tag{3.2}$$

Table 3.2: Comparison of variation in bubble separation distance.

ΔT (K)	E (V/m)	El^*	λ_B (mm)	λ_J (mm)	$\frac{\lambda_J}{\lambda_B}$	$\frac{\lambda_S}{\lambda_B}$
2	0	0		–	–	0.833
	1×10^5	0.6300	2.278	1.60	0.702	0.50
	2×10^5	2.5130		0.709	0.311	0.278
5	0	0		–	–	0.909
	1×10^5	0.6300	2.278	1.60	0.702	0.55
	2×10^5	2.5130		0.709	0.311	0.263
18	0	0		–	–	1.0
	1×10^5	0.6300	2.278	1.60	0.702	0.50
	2×10^5	2.5130		0.709	0.311	0.256
22	0	0		–	–	1.0
	1×10^5	0.6300	2.278	1.60	0.702	0.50
	2×10^5	2.5130		0.709	0.311	0.25

For the large values of electric field, the value $q(E)/q(0)$ is predicted to vary linearly with f since f is proportional to E^2. To justify this postulation, effect of varying electric field intensities on the heat transfer characteristics is observed through simulations. The ratio of the heat flux and the Nusselt number for the cases of with and without the electric field at a different range of superheats and electric influence numbers is shown in Table 3.3. Here, the subscripts J and S represent Johnson's prediction and the present simulation, respectively. The subscripts B, SD and S associated with the Nusselt numbers represent the values calculated from Berenson's correlation [6], Son and Dhir's correlation [166](Eq. **??**) and the present simulation, respectively. First column is the superheat temperature in excess of the saturation temperature, i.e. $\Delta T = T_s - T_{sat}$. For the electric influence number $El^* = 0.0006$, which corresponds to an electric field intensity of 1×10^4 V/m, the value of the ratio $q(E)/q(0)$ is very close to unity while for the higher values of electric field it is comparatively much higher than unity. For low values of the term $\frac{3(\rho_l - \rho_v)g\sigma}{f^2}$, i.e. for the higher electric fields, the heat flux is affected much more.

Table 3.3: Comparison of heat transfer characteristics.

ΔT	El^*	$\left[\frac{q(E)}{q(0)}\right]_J$	$\left[\frac{q(E)}{q(0)}\right]_S$	$\frac{3(\rho_l-\rho_v)g\sigma}{f^2}$	Nu_B	Nu_{SD}	Nu_S
	0	1.0000	1.0000	–	5.44	5.471	5.50
	0.0006	1.0009	1.0035	76018			5.51
2	0.1570	1.0224	1.0922	122			6.0
	0.6300	1.0869	1.4893	8			8.15
	0	0	1.0000	–	4.32	5.573	5.25
	0.0006	1.0009	1.0015	76018			5.27
5	0.1570	1.0224	1.1164	122			5.75
	0.6300	1.0869	1.3429	8			6.95
	0	0	1.0000	–	3.63	5.727	5.08
	0.0006	1.0009	1.0030	76018			5.10
10	0.1570	1.0224	1.0870	122			5.55
	0.6300	1.0869	1.3520	8			7.05
	0	0	1.0000	–	3.28	5.835	5.20
	0.0006	1.0009	1.0040	76018			5.21
15	0.1570	1.0224	1.0550	122			5.48
	0.6300	1.0869	1.3200	8			6.90
	0	0	1.0000	–	3.14	5.887	5.26
	0.0006	1.0009	1.0041	76018			5.27
18	0.1570	1.0224	1.0413	122			5.50
	0.6300	1.0869	1.3283	8			7.10

Thus, from our simulations, it is also inferred that a higher value of electric field intensity is required to bring any significant enhancement in heat transfer rate.

In Fig. 3.19, the variation in heat flux ratio, $q(E)/q(0)$ with increasing intensity of electric field is compared for the superheats of 5 K and 18 K. It can be observed that the significant increase in heat flux ratio is observed only above 5×10^4 V/m,

below which the the ratio $q(E)/q(0)$ is nearly equal to unity. For the higher range of electric field values, we observe comparatively larger increase in the heat flux ratio for a superheat of 5 K as compared to that of the superheat of 18 K. Although for some combinations of superheat and electric field values, this deduction may not hold good. However, in most of the cases we observe that at the lower superheat values, the electric field seems to have more prominent effect as compared to higher superheats.

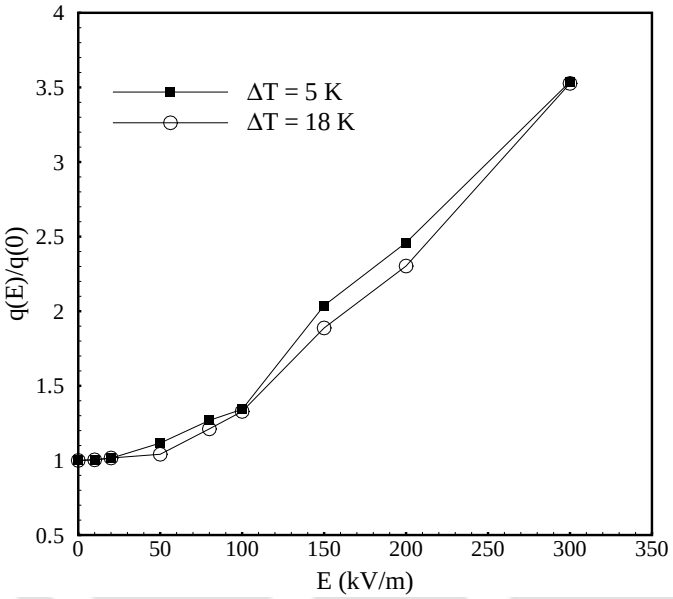

Figure 3.19: Comparison of the ratio of heat flux values with electric field to without electric field between superheats of 5 K and 18 K.

3.6 Summary

The analyses performed in the present chapter have been focused on the effects of wall superheat and aplied electric field on the changes in morphology of bubbles and associated heat transfer. The dependence of bubble formation on the parameters affecting the instabilities at the liquid-vapor interface during saturated film boiling has been studied. As the growth and departure of the bubble in this regime is dependent on the heat-flux from the heated surface along with the balance between dynamical factors like buoyancy and surface tension, the changes in degree of superheat have been found to significantly govern the processes. A transformation in the

instability-mode governing the bubble-growth has been found with an increase in the superheat value. The bubbles depart alternately from nodes and anti-nodes of the most critical wavelength and hence a periodicity with space and time has been observed. Discrete bubbles are formed at lower superheats while continuous vapor columns are generated at higher superheats. The critical wavelength of disturbance which governs the separation distance between adjacent bubbles decreases with the application of an electric field across the interface. The electric field is found to affect the periodicity of bubble release and heat transfer rate only after it attains a threshold value of intensity.

Chapter 4

Saturated Film Boiling at Various Levels of Gravity

The analyses of the bubble growth and heat transfer characteristics in saturated film boiling at various levels of gravity have been performed through direct numerical simulations. In addition to this, the occurence of self-similarity in interface structures during the initial stages of bubble growth is examined. The phenomena of bubble growth is strongly influenced by the buoyant forces due to gravity and its dominant effect is found to be replaced by the electrohydrodynamic forces in reduced gravity conditions. The decrease in gravitational acceleration results in an increase in the characteristic wavelength and time scale. The bubble volume and maximum height before pinch-off, thus increase enormously as the gravity value is reduced. The bubble pinch-off velocity is found to have decreased significantly under reduced gravity conditions. Heat transfer rate deteriorates in reduced gravity conditions which can be recovered by an externally imposed electric field. The dominance of electric field on the heat transfer rate is found to be more in reduced gravity conditions. However, as the value of imposed electric field is enhanced, the difference in the effect of increasing heat flux tends to reduce.

The contents in this chapter have been published as Pandey, V., Biswas, G., and Dalal, A., 2017, vol. **29**, pp. 032104-1 – 032104-13 "Saturated film boiling at various gravity levels under the influence of electrohydrodynamic forces", *Physics of Fluids*, (available online, DOI: http://dx.doi.org/10.1063/1.4978056).

4.1 Introduction and Definition of the Problem

In normal terrestrial conditions on earth, the acceleration due to gravity is the most dominant factor that controls the physics of vapor flows in boiling. Other forces, such as the capillary forces due to surface tension are often considered to have negligible effect due to the predominance of the buoyancy force. The most dominant wavelength of disturbance in film boiling as defined by the hydrodynamic theory of Zuber [4] is inversely proportional to the square root of gravity. Hence, in reduced gravity condition, the separation distance between the detaching bubbles is much larger than that in normal gravity. Also, the buoyancy force is reduced significantly and the counter force of surface tension which tends to keep the bubbles attached to the vapor volume becomes much more relevant [26]. Although it has been observed that the reduced gravity does not influence the nucleate boiling regime, it still has a significant effect in the transition and film boiling regime and can reduce the heat transfer rate by up to 50 percent [27].

The study concerning the effect of low gravity in film boiling has remained a topic of substantial interest. The present study is focused to analyze, in detail, the changes in bubble dynamics, spacing between the adjacent bubbles and heat transfer characteristics at various ranges of gravity levels. Attempts have been made to determine the changes in maximum height of the bubbles and the bubble pinch-off velocities with change in gravity. In addition to this, we have also tried to show the self-similarity behavior of the bubble interface during its linear growth phase.

The present analysis utilizes the formulation explained in Chapter 2. The simulations are performed for various domain lengths proportional to Berenson's most dominant wavelength [6], $\lambda_B = 2\pi\sqrt{3\sigma/(\rho_l - \rho_v)g}$. The fluids used are water and R134a near critical pressure whose properties have been mentioned in Tables 3.1 (for water) and 4.1 (for R134a), respectively.

Boiling beyond minimum heat flux region on the boiling curve, i.e. film boiling is simulated using the boundary conditions as mentioned in Sec. 2.8. The schematic of the model is the same as shown in Fig. 3.1 in Chapter 3. It is to be noted that the length scale $l_s = \sqrt{\sigma/(\rho_l - \rho_v)g}$ is a function of gravity. The most dangerous wavelength in earth's normal gravity near critical pressure for water ($P = 0.99P_c$) is $\lambda_B = 0.002275$ m and for R134a ($P = 0.92Pc$) is $\lambda_B = 0.002263$ m. The grid dimension is taken as $\Delta x = \lambda_B/240$ in all the simulations performed herein. The

Table 4.1: Properties of R134a with $T_{sat} = 370.46$ K; $P_{sat} = 3.763$ MPa; $h_{lv} = 54.6$ kJ/kg; $\sigma = 0.182$ mN/m

Phase	ρ (kg/m^3)	μ (N.s/m^2)	k (W/m.K)	c_p (kJ/kg.K)	ϵ
Liquid	730.8	56.72	0.0520	5.128	5.0
Vapor	301.9	21.71	0.0415	4.445	4.2

symbol, λ_B corresponds to the most dangerous wavelength in terrestrial condition. A time-step of value $\Delta t = 5.0 \times 10^{-6}$ s is used in all simulations which is consistent with the capillary time limit. The bubble dimensions and spacing between adjacent bubbles are expected to be enhanced in the case of reduced gravity as compared to those in normal gravity conditions. Simulations have been performed considering saturated water and refrigerant R134a as the working fluids near critical pressure. In order to analyze the variation in bubble release pattern and the shape of the bubble under normal and reduced gravity conditions, numerical simulations have been performed with and without the application of an electric field. In the sections to follow, we have tried to explore the effect of variation in gravity level on the bubble dynamics, i.e. the bubble release frequency and spacing between bubble formation sites, pinch-off velocity, bubble release time and maximum height of the bubble. In addition to these, the changes in heat transfer characteristics owing to different levels of gravity and various intensities of electric fields have been determined using the simulations. Together with the earth's normal gravity, two different gravity levels have been considered in the present study. In order to compare with realistic values, we have also considered gravity levels corresponding to moon ($g/g_e = 0.16$) and mars ($g/g_e = 0.37$).

4.2 Boiling at Different Levels of Gravity

During film boiling, the heating of the vapor layer from the superheated bottom surface leads to vaporization of the adjacent liquid mass close to the interface. The vapor mass generated continuously tends to buoy away due to the difference in density of vapor and liquid. The tendency of movement of vapor mass gets suppressed as the gravity is reduced. Simulations are performed in the domain size with hor-

izontal span of $5\lambda_B$ for R134a and $3\lambda_B$ for water to show the change in bubble morphology. It may be mentioned that the bubble pinch-off and the frequency of bubble release have been accurately predicted using a similar domain and technique as by Agarwal et al. [167]. The vertical span varies as the wavelength corresponding to the gravity-level of interest.

In order to determine the morphological variations at the interface owing to varying gravity-levels, simulations have been performed in the domain size of $5\lambda_B$ for R134a. It can be observed from the Fig. 4.1 that the dimensions of the bubbles become larger as the gravity is reduced. The spacing between adjacent bubble formation sites increases significantly with the reduction in the level of gravity. Also, the time for the first set of bubble departure increases with the decrease in gravity. The time for the first set of bubble release corresponding to each gravity-level is illustrated in Fig. 4.1. The number of bubbles for a fixed domain at any given gravity-level should be consistent with the critical wavelength defined by Taylor-Helmholtz instability. The number of bubbles for the case of $g/g_e = 1.0$, is five which is consistent with the requirements of Taylor-Helmholtz instability. For $g/g_e = 0.37$ the number reduces to four bubbles, for which the number of bubbles defined by instability criterion is between three and four. For $g/g_e = 0.16$, two bubbles in $5\lambda_B$ domain is also consistent with the instability criterion for that level of gravity.

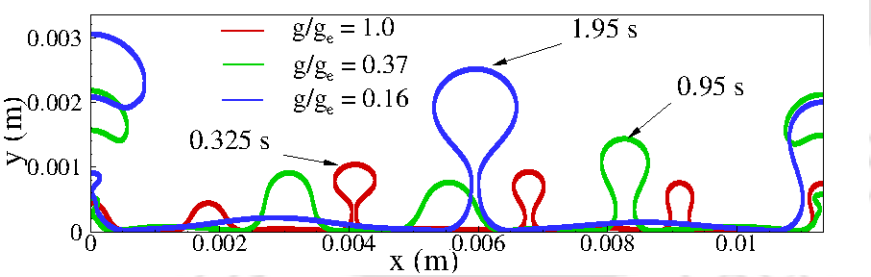

Figure 4.1: Comparison of interface profiles at the instant of first set of bubble release at three different levels of gravity for R134a with $\Delta T = 20$ K

Similar analysis has been performed using water as the working fluid in the domain size of $3\lambda_B$. The results are shown in the Fig. 4.2 for the first set of bubble release. Increase in bubble size and increased distance between bubble formation sites is observed at reduced gravity conditions.

In order to show the variation in bubble dynamics as a result of change in the level of gravity, a minimum domain length is required. The larger domain length explains the variations in a better manner. As compared to the case of water, the

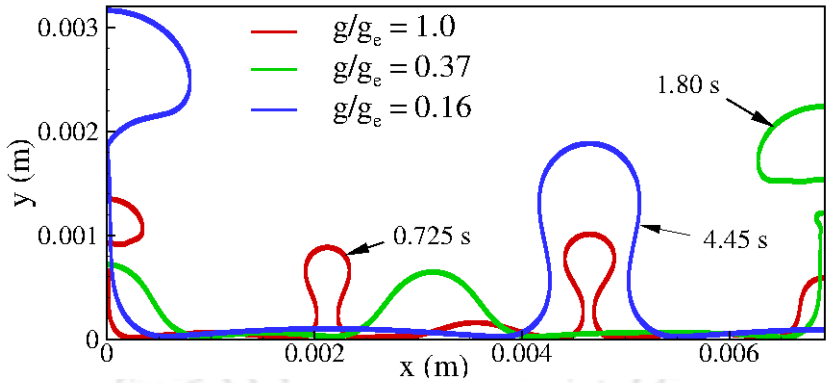

Figure 4.2: Comparison of interface profiles at the instant of first set of bubble release at three different levels of gravity for water with $\Delta T = 5$ K

domain length in the case of R134a can be extended to $5\lambda_B$ due to the low values of specific heat and latent heat of vaporisation.

Figure 4.3 shows the variation in the height of the apex of the vapor bubble with time for both normal ($g/g_e = 1.0$) and reduced gravity ($g/g_e = 0.1$) conditions during the growth of a single bubble. It can be clearly observed that the maximum height of the bubble in reduced gravity is more than three times of the one in normal gravity. The number of bubbles formed (number of peaks) is five for normal gravity as compared to the single bubble formed in reduced gravity during the same time interval. The rate of increase of maximum height of interface till the onset of bulging of the bubble is very low as compared to the growth rate after neck formation. It may be stated that along with the slower growth of interface due to reduced gravity, the bubble volume also requires to be larger so that the bubble can generate enough buoyancy force to be buoyed away. The larger bubble volume is indicated by greater apex height of the bubble.

The decrease in buoyancy force due to the reduced gravity results in slower rate of bubble growth. It is clearly illustrated in the Fig. 4.3 where the slow growth rate leads to the delayed departure of the bubble in the case of reduced gravity. The reduction in buoyancy force not only leads to the delay in bubble departure but also can be contemplated to reduce the bubble pinch-off velocity from the vapor film. This effect is verified from the plot of the vertical velocity of the vapor bubble during its growth period starting from its inception to the departure. This is illustrated in Fig. 4.4 where the vertical velocity is averaged over all the vapor cells and two phase cells associated with the growing vapor bubble. The velocity is calculated after

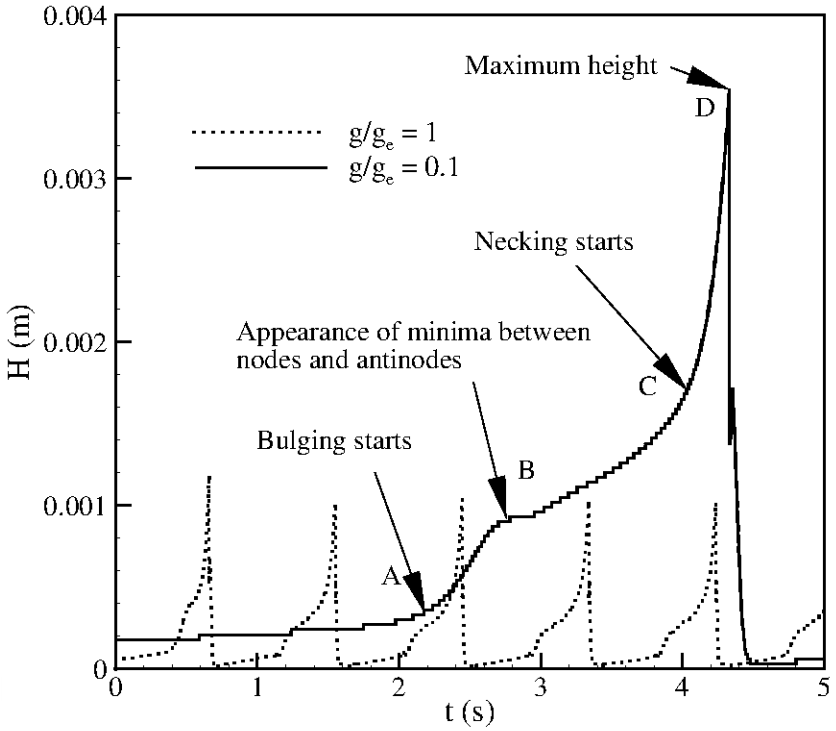

Figure 4.3: Variation of apex height of bubble with time at normal and reduced gravity conditions for water at $\Delta T = 5$ K.

the vapor bulge attains a height of $\lambda_B/8$. As can be observed from the plot, the maximum velocity occurs just before the bubble roll-up (mushroom shape) begins. Specifically, this is the instant of having the neck streched before the pinch-off. Due to roll-up of vapor column, vortices are generated and hence some components of velocities are directed in the negative y direction. As a result, there are fluctuations in the plot near the maximum value. The different shapes of bubble during its growth have been shown at the corresponding points in the plot. Point 'C' corresponds to the instant just before the initiation of streching due to neck formation. After the bubble pinch-off, the left-over vapor packet recoils back and impinges on the horizontal vapor film. This attributes to the negative velocity in the plot.

The effect of reduced gravity results in decreasing the pinch-off velocity of bubble. It can be observed from the plot that the value of pinch-off velocity at normal gravity ($g/g_e = 1.0$) is close to 0.05 m/s while at the reduced gravity ($g/g_e = 0.16$), the value decreases to about 0.03 m/s. Hence, a significant decrease in the pinch-off velocity occurs due to the reduction in gravity.

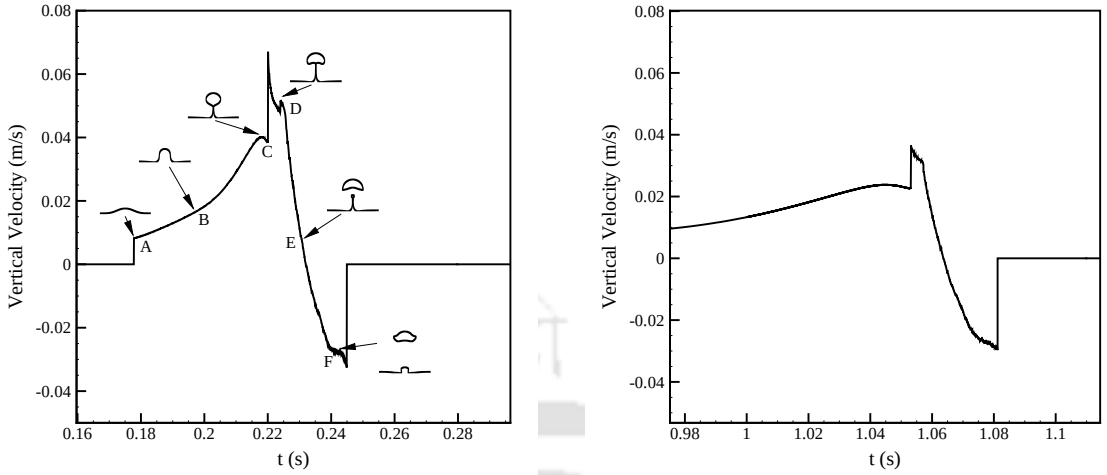

Figure 4.4: Variation in vertical velocity of vapor volume during the growth and detachment of a bubble in (a) normal gravity ($g/g_e = 1.0$) and (b) reduced gravity ($g/g_e = 0.16$) with time for R134a at $\Delta T = 30$ K.

The radius of the growing bubble is also calculated using the same approach of area averaging. The area-average-based radius from all the two phase cells and vapor cells is plotted in Fig. 4.5 at normal and reduced gravity conditions. The plot shows that the maximum radius (≈ 0.066 cm) of the bubble before detachment in reduced gravity condition is more than two times the radius (≈ 0.032 cm) in normal gravity condition. Also the inception time and total time of growth of the bubble is more in the case of reduced gravity as compared to that in normal gravity.

During film boiling, heat removal from the heated surface occurs as a result of continuous departure of vapor bubbles from the vapor film to the bulk liquid. Thus the heat transfer takes place from the surface to the bulk liquid through the vapor layer. This vapor removal rate tends to decrease when the gravity is reduced. Heat transfer analysis is performed using water and R134a as the fluids, to determine the effect of variation in gravity levels. The variations in heat flux are shown in Fig. 4.6(a) for water and in Fig. 4.6(b) for R134a at different levels of gravity. For water at normal gravity ($g/g_e = 1.0$), the value of heat flux, averaged over space and time, is 66 kW/m^2 while it is 42 kW/m^2 at $g/g_e = 0.37$ and 30 kW/m^2 at $g/g_e = 0.16$. For R134a at normal gravity ($g/g_e = 1.0$), the value of heat flux averaged over space and time is 28 kW/m^2 while it is 19 kW/m^2 at $g/g_e = 0.37$ and 13 kW/m^2 at $g/g_e = 0.16$. It is thus inferred from the heat flux results that the reducing gravity

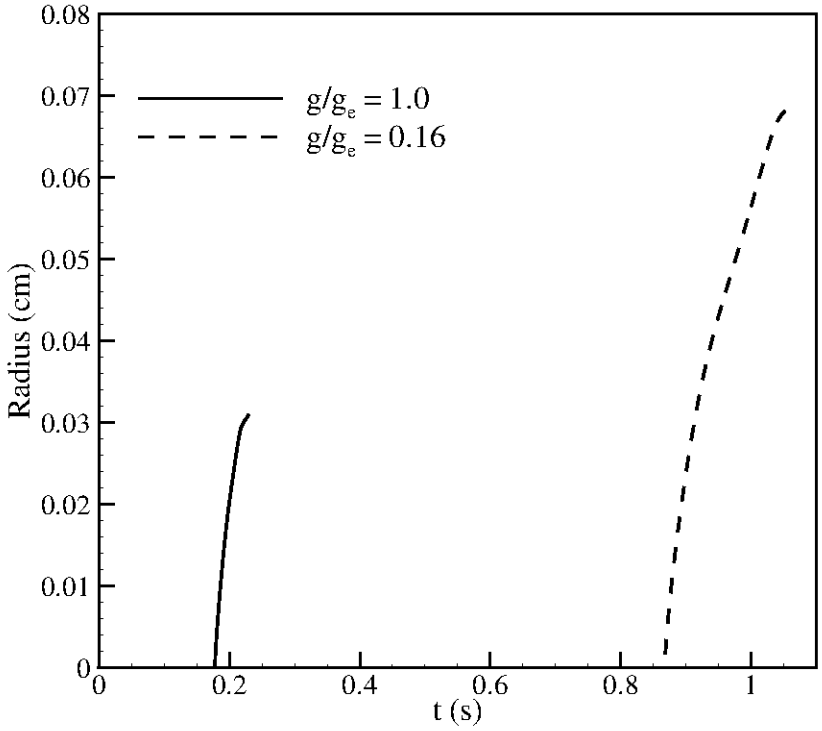

Figure 4.5: Comparison of bubble radius between normal gravity ($g/g_e = 1.0$) and reduced gravity ($g/g_e = 0.16$) for R134a at $\Delta T = 30$ K.

has dimishing effect on the heat transfer rate. The similar trend was observed by Zell et al. [15] and Merte and Clarke [22] in their experimental investigations.

4.3 Boiling with EHD at Different Levels of Gravity

Application of electric field along the direction of evolving vapor bubbles results in increased instabilities at the liquid-vapor interface. This can be deduced from the analytical dispersion relation for the frequency of bubble release given by Johnson [9]. The additional stresses due to electric field brings about critical morphological changes on the interface which affects the entire boiling regime. Di Marco and Grassi [38] described the existence of two different regimes of film boiling in reduced gravity under applied electric field. This was done based on the intensity of the applied electric field. At a low intensity of electric field under a low gravity condition, the boiling is highly affected and is deteriorated as compared to that at a normal gravity with same value of the electric field. While at a very high intensity, the

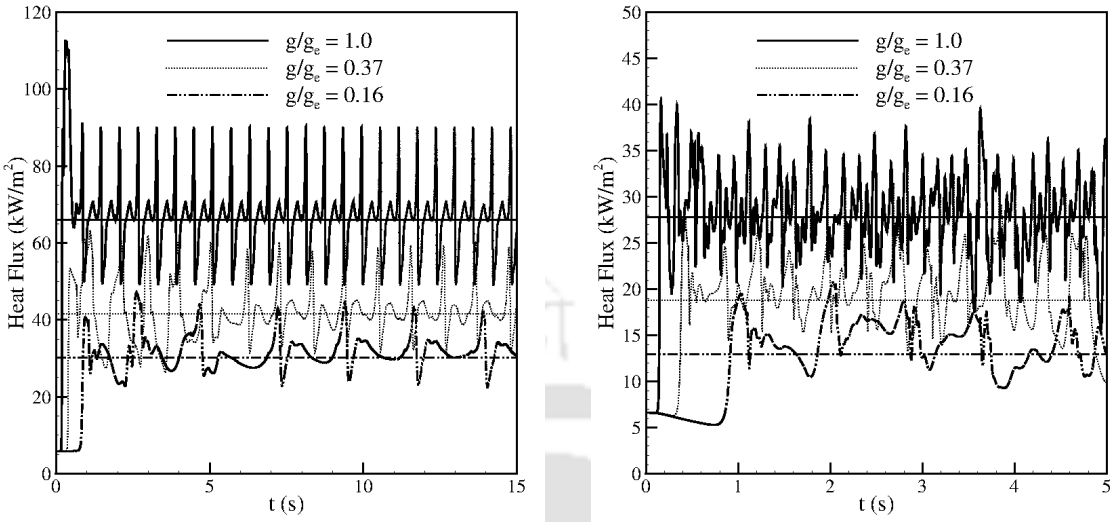

Figure 4.6: Comparison of heat flux variation with time at different levels of gravity for (a) water at $\Delta T = 5$ K and (b) R134a at $\Delta T = 30$ K.

difference in the effect of electric field on boiling at a low gravity and under normal gravity is not significant. Hence, beyond a certain value, electric field force dominates the flow behavior offsetting the effect of gravity.

The increased disturbance at the interface due to the applied electric field decreases the value of most dominant wavelength. The spacing between the adjacent bubbles decreases significantly and the bubble release frequency also gets enhanced. The effect of reduced gravity can thus be counterweighed by the application of electric field. The length and time scale in normal gravity can also be restored and controlled by applying a suitable intensity of electric field under reduced gravity conditions. These effects can be seen from the comparisons of the first set of bubble release at different gravity levels followed by the application of electric field at a reduced gravity, as shown in Fig. 4.7 and Fig. 4.8. Figure 4.7 corresponds to the simulation for water in a $3\lambda_B$ domain and Fig. 4.8 corresponds to that for R134a in a $5\lambda_B$ domain. The increased frequency of bubble release and reduced spacing between adjacent bubbles are observed in both fluids (water and R134a) owing to the application of electric field.

Application of electric field of same intensity in normal and reduced gravity shows different effects. This may be contemplated from the Eq. 3.2 which refers that as the gravity is reduced the ratio of heat transfer with electric field to that without

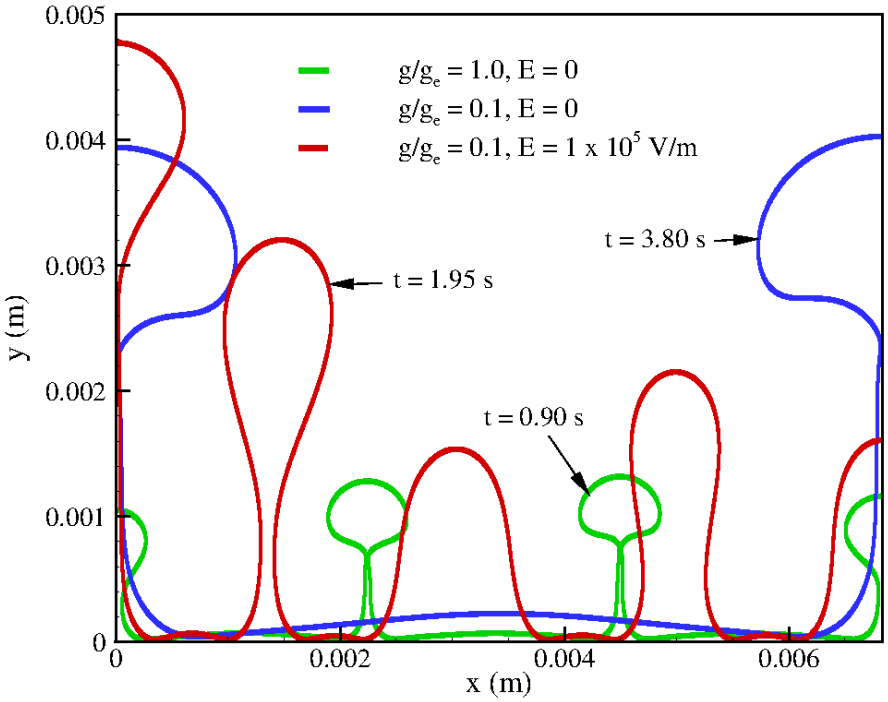

Figure 4.7: Comparison of interface profile at the instant of first set of bubble release for water with $\Delta T = 18$ K and at different values of applied electric field and levels of gravity.

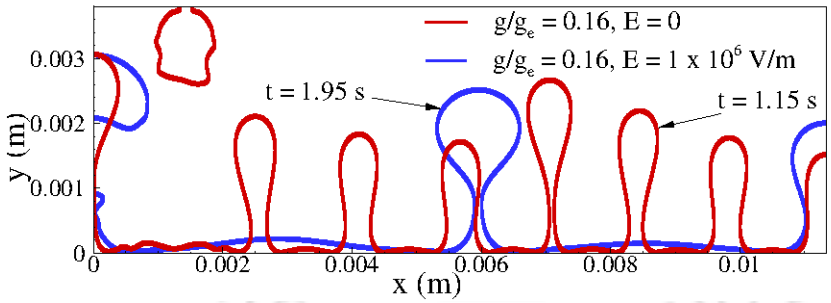

Figure 4.8: Effect of an applied electric field on bubble morphology for R134a with $\Delta T = 20$ K.

electric field increases. Hence, one can also speculate the change in morphological behavior of the interface with the application of same intensity of electric field under different levels of gravity. This may become more clear from the results shown in Fig. 4.9 and Fig. 4.10. Figure 4.9(a) shows discrete bubble release under normal gravity ($g/g_e = 1.0$) with three bubbles in $3\lambda_B$ domain. With the introduction of electric field of intensity 2×10^5 V/m, the number of bubbles inreases to ten bubbles

in $3\lambda_B$ domain [Fig. 4.9(b)]. Even under such a situation, separate bubble release sites are discerned without any merger between the adjacent bubbles. The time instant of the first set of bubble release has also been shown. In the reduced gravity condition ($g/g_e = 0.1$), the bubbles detach separately [Fig. 4.10(a)] with a distance of $3\lambda_B$ between the adjacent bubble formation sites. However with the application of electric field, the bubble formation sites increase and the departing bubbles seem to interact vigorously and start merging with each other. The results have been shown in Fig. 4.10(b). The lateral merging can be due to the increased dominance of capillary forces as compared to the buoyancy force. This effect get enhanced in reduced gravity.

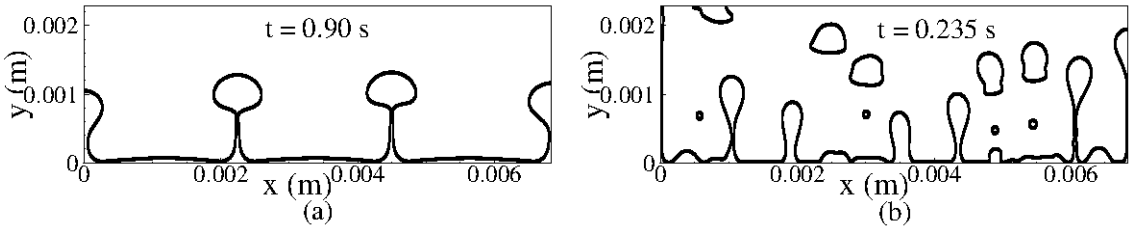

Figure 4.9: Interface morphology at the instant of first set of bubble release at normal gravity ($g/g_e = 1.0$) (a) without electric field and (b) with an applied electric field of intensity E = 2×10^5 V/m for water with $\Delta T = 18$ K.

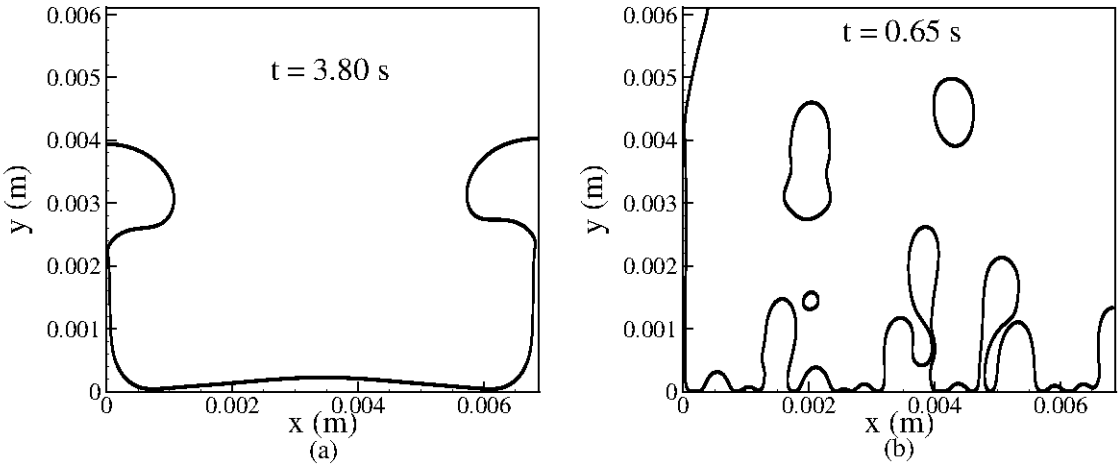

Figure 4.10: Interface morphology at the instant of first set of bubble release at reduced gravity ($g/g_e = 0.1$) (a) without electric field and (b) with an applied electric field of intensity 2×10^5 V/m for water with $\Delta T = 18$ K.

The reduced gravity effect delays the departure of the bubbles from the vapor

Table 4.2: Comparison of variation in heat flux with applied electric field at various gravity levels for water.

Gravity	q_0	$E = 5 \times 10^4$ V/m		$E = 8 \times 10^4$ V/m	
(g/g_e)	(kW/m^2)	q_E(kW/m^2)	(%) increase	q_E(kW/m^2)	(%) increase
1.0	66	72	9.0	77	16.67
0.37	42	55	30.95	62	47.61
0.16	30	40.1	33.67	50	66.67

film and thus the heat transfer rate from the heated surface gets deteriorated. As the application of electric field enhances the frequency of bubble release, the heat transfer rate also gets improved. This can be observed from the Figs. 4.11(a), 4.11(b) and 4.11(c) where the variation of heat flux with time is shown for different values of electric field at $g/g_e = 1.0$, $g/g_e = 0.37$ and $g/g_e = 0.16$, respectively. It is observed that the effect of electric field, i.e. the percentage increase in heat flux value for the same intensity of electric field is more in reduced gravity than that of the normal gravity condition. The observed changes are tabulated in Table 4.2. The percentage increase in heat flux owing to any imposed electric field is with respect to the value of heat flux without electric field. It can be observed from the tabulated data that the percentage increase in the heat flux for any given value of electric field increases with decrease in the level of gravity.

From the variation of heat flux with varying imposed electric field at a given value of gravity, it is observed that the effect of electric field increases with decrease in gravity. The difference in percentage increase of heat flux with application of electric force increases with the intensity of electric field. This observation can be more clearly stated from the plots shown in Figs. 4.12(a) and 4.12(b). The heat flux plots at different levels of gravity at a specified high intensity (2×10^5 V/m) of electric field tends to become close. At even higher value of electric field (3×10^5 V/m), the heat flux plots almost coincide with each other at different levels of gravity. Under the reduced gravity condition, the magnitude of heat flux is less than under the normal gravity condition at every given intensity of imposed electric field. However, the ratio of heat flux with electric field (q_E) to the heat flux without electric field (q_0) is found to be much larger in the case of reduced gravity condition for the range of applied electric field. This has been illustrated by the plots in Figs. 4.13(a) and

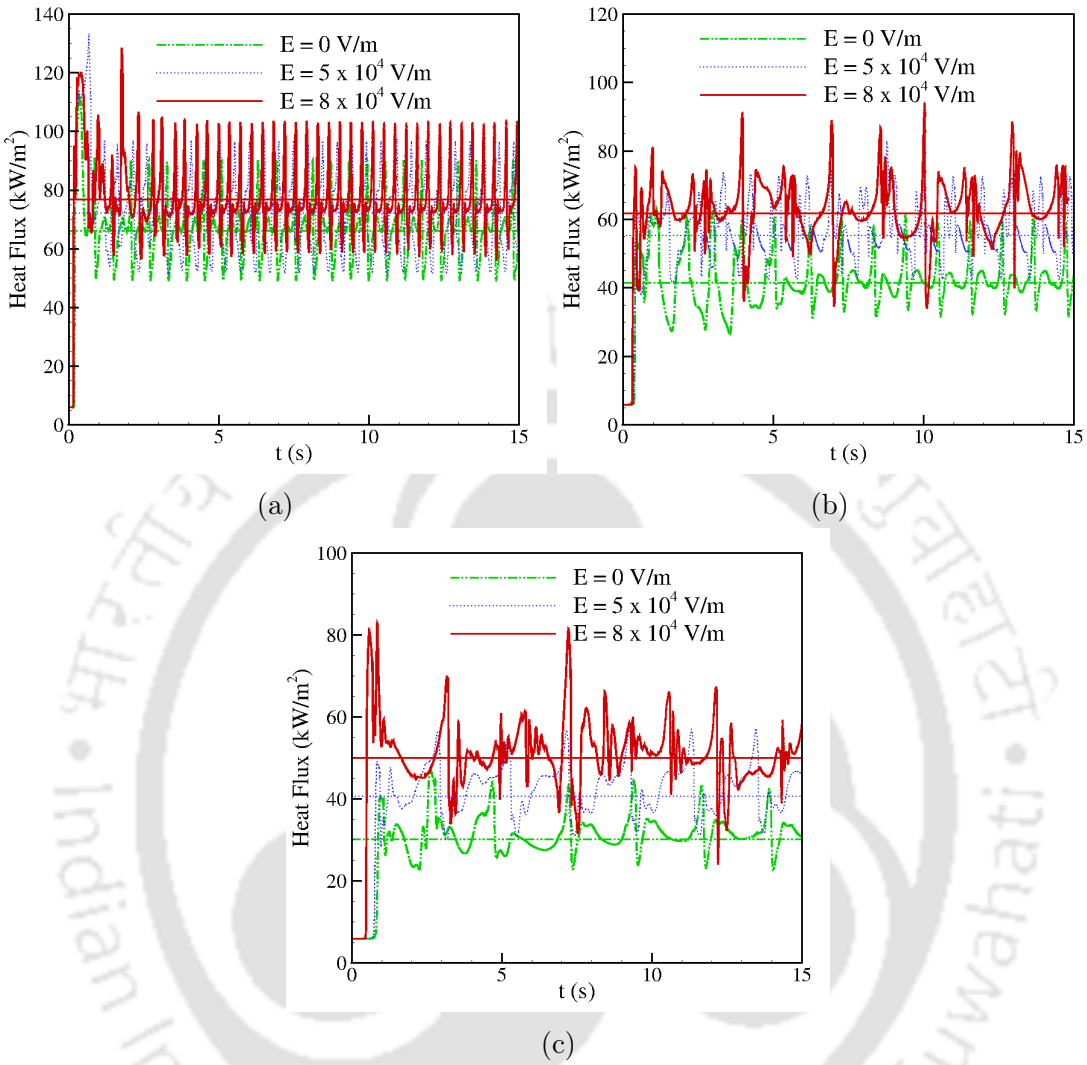

Figure 4.11: Interface growth for water at 5 K wall superheat with different values of applied electric field intensity at gravity levels of (a) $g/g_e = 1.0$ (b) $g/g_e = 0.37$ and (c) $g/g_e = 0.16$.

4.13(b). It can be observed from the plots in Fig. 4.13(a) that as the intensity of electric field increases, the difference in heat flux values decreases between normal and reduced gravity conditions. Hence, the dominance of electric field seems to increase with the increase in intensity of electric field for the lower value of gravity.

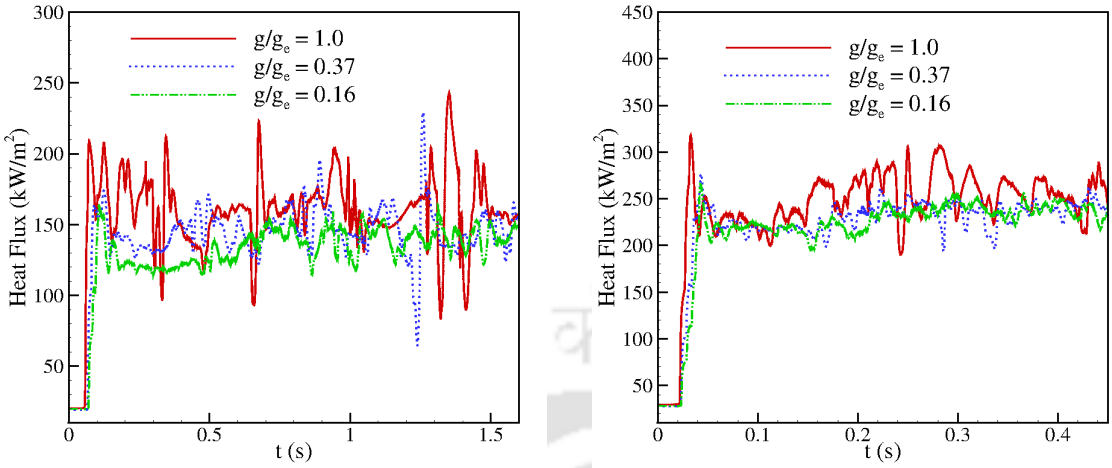

Figure 4.12: Variation of heat flux at different gravity levels at an applied electric field intensity of (a) 2×10^5 V/m and (b) 3×10^5 V/m for water at $\Delta T = 5$ K.

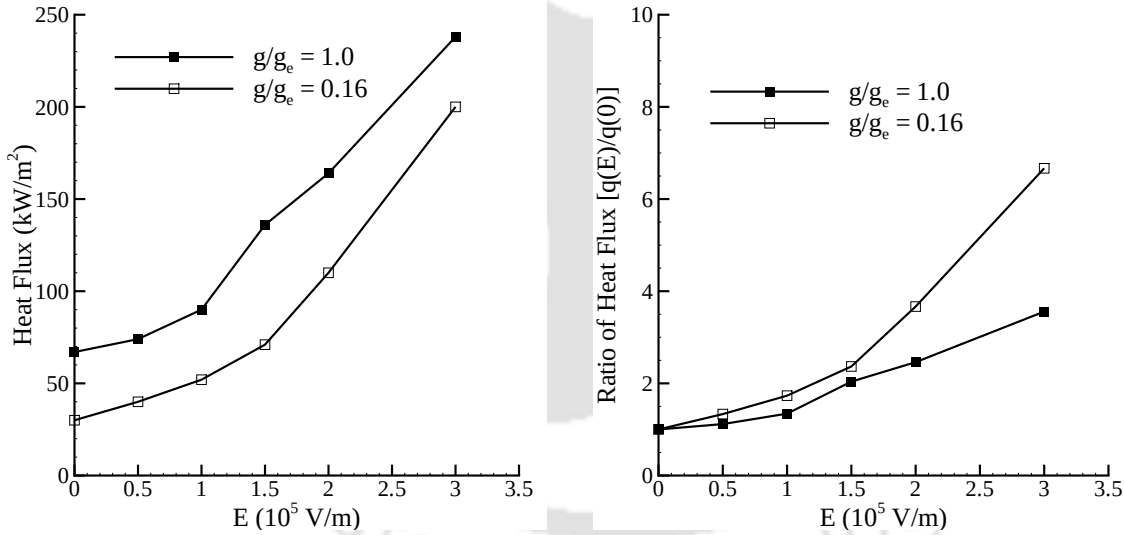

Figure 4.13: Variation of (a) heat flux and (b) ratio of heat flux with electric field to that of without electric field in normal and reduced gravity conditions for water at $\Delta T = 5$ K.

4.4 Self-similarity During Bubble Growth

Generation of vapor due to applied heat flux results in velocity jump across the liquid-vapor interface. Aggravated by the gravity-capillary effects combined with

the applied heat flux, it generates free surface waves. The bubble growth is a consequence of increased Rayleigh-Taylor instability at the liquid-vapor interface at lower degree of superheat. The instability mode shifts to Taylor-Helmholtz as the superheat is increased [3, 161].The vapor bulge incipience tending to bubble formation can be considered as a dynamical phenomenon exhibiting singularity. Every physical system exhibiting such singularities leads to an ultraviolet cutoff (defined by Hogrefe et al. [168]) terminating the singularity. In this case, this cutoff is depicted as the detachment of the growing bubble from the bulk vapor phase.

The vapor growth affected by the Rayleigh instability leads to a mushroom like structure in the case of viscous fluids. This phenomenon initiates the neck formation in the growing vapor mass. Duchemin et al. [169] studied the self-similarity behavior of the tip of the growing spikes in accelerated motion of the liquid due to the Rayleigh-Taylor instability. The study assumed inviscid fluid with high density ratio. As mentioned in Hogrefe et al. [168], the instability in the presence of stretching occurring at the neck, results due to axial velocity of the fluid around the growing spike. Hogrefe et al. [168] developed a relation for the height of the growing spike in Faraday singularity as a function of the radius of the spike and the time of growth. The profile of the growing spike is given as $y = bt^{\alpha}(xt^{\beta})^{\gamma}$.

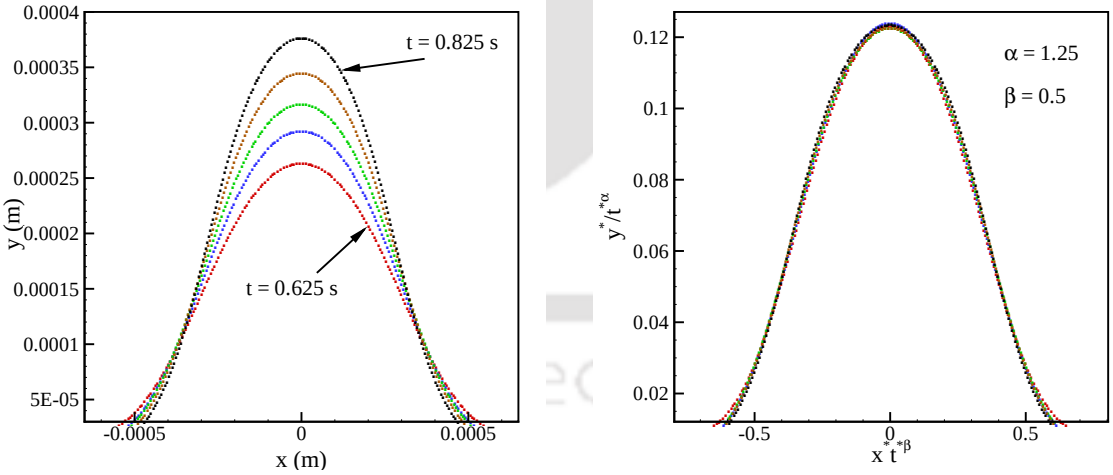

(a) (b)

Figure 4.14: (a) Interface profiles at different instants of time from t = 0.625 s to t = 0.825 s for $\Delta T = 2$ K. (b) Profiles at the same instants of time as in left hand side, rescaled following $y^*/t^* = ax^*t^{*\beta}$

Considering the initial phase of bubble growth as influenced by the Rayleigh-

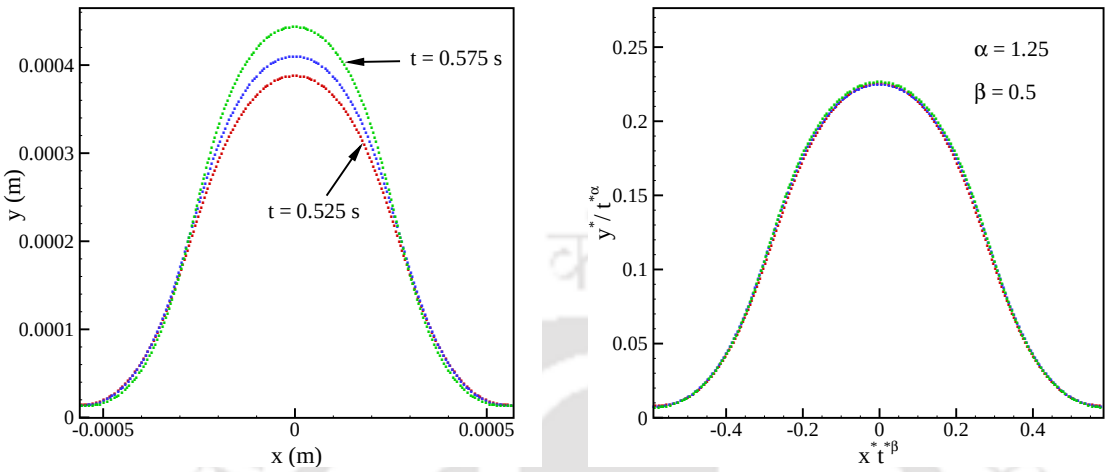

(a) (b)

Figure 4.15: (a) Interface profiles at different instants of time from t = 0.525 s to t = 0.575 s for $\Delta T = 5$ K. (b) Profiles at the same instants of time as in left hand side, rescaled following $y^*/t^* = ax^*t^{*\beta}$

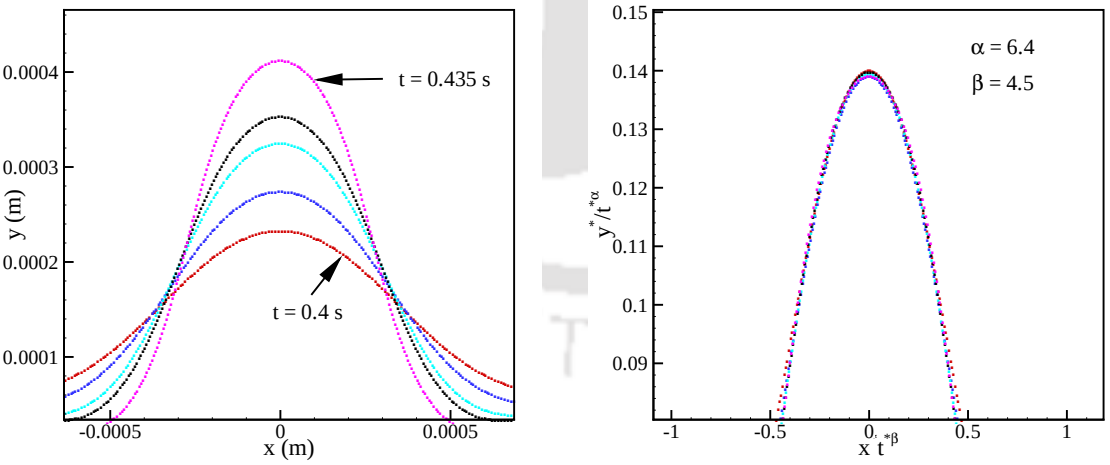

(a) (b)

Figure 4.16: (a) Interface profiles at different instants of time from t = 0.40 s to t = 0.435 s for $\Delta T = 10$ K. (b) Profiles at the same instants of time as in left hand side, rescaled following $y^*/t^* = ax^*t^{*\beta}$

Taylor mode of instability, we performed self-similarity analysis of the profiles of growing vapor bubbles. The fitting function we used is of the form, $y^*/t^* = ax^*t^{*\beta}$ as the general solution for the kinetic free-surface problem of Hogrefe et al. [168]. For small superheat value of $\Delta T = 2$ K, between the time instants t = 0.625 s and t = 0.825 s, the growing bubble profiles collapse on a single curve (Fig. 4.14). The relation between α and β is followed as, $\alpha = 1 + \beta/2$. The value of the constant a is 1 and the values of the exponents α and β are 1.25 and 0.5, respectively. The dimensional quantities are scaled with half of the characteristic wavelength, $\lambda_B/2$ and the time is scaled using viscous time, $\tau_v = l^2\rho_l/\mu_l$ where l is the characteristic length scale. The same analysis is performed at $\Delta T = 5$ K for the same values of α and β. The profile is shown in Fig. 4.15. It is observed that the growing vapor bubble profiles follow self-similarity but for a smaller time range, i.e. between t = 0.525 s and t = 0.575 s. This indicates the variation in the values of exponents α and β with the increase in the value of the superheat. The above indication proved to be valid from the self-similarity profiles of interface growth at $\Delta T = 10$ K as shown in Fig. 4.16.

The values of the exponents are taken as $\alpha = 6.4$ and $\beta = 4.5$ and the relation between α and β is $\alpha = 1 + 6\beta/5$. The difference in the values of the scaling exponents and their interrelationship can be attributed to the change in instability mode with increasing superheat.

4.5 Summary

In this chapter, the study concerning saturated film boiling under reduced gravity has been performed through direct numerical simulations. Boiling under reduced gravity results in reduction in heat transfer rate and appreciable variation in bubble morphology as compared to that under normal gravity. The application of electric field in reduced gravity conditions has been observed to restore the heat transfer rate to that in normal gravity. Simulations performed showed a significant enhancement in length and time scales for boiling in reduced gravity. The most significant observation from the present work under reduced gravity is the increase in the dominance of electric field as the gravity-level is reduced which has been signified by the variation of ratio of heat flux value with applied electric field to that without electric field.

Chapter 5

Bubble Lifecycle During Heterogeneous Nucleate Boiling

Heterogeneous nucleate boiling over a flat surface has been studied through complete numerical simulations. During the growth and departure of the vapor bubble, the interface is tracked following a coupled level-set and volume of fluid (CLSVOF) approach. A microlayer evaporation model due to Sato and Niceno ["A depletable micro-layer model for nucleate pool boiling," Journal of Computational physics 300, 20-52 (2015)] has been deployed in this investigation. A detailed study of the changes in the microlayer structure as a result of different modes of boiling has been performed. The departure diameter is found to increase with increase in substrate superheat. The predicted departure diameter has been compared with the available experimental and analytical results. A power-law curve has been obtained for depicting the growth rate of the bubble depending on the degree of superheat at the wall. The space-time averaged wall-heat flux at different values of superheat temperature of substrate is obtained. Bubble growth during subcooled boiling at low and intermediate subcooled degrees has been observed through direct numerical simulations. The variations in bubble dynamics after its departure from the surface in saturated and subcooled liquid conditions have been compared.

5.1 Introduction and Definition of the Problem

In the present investigations, a single bubble during nucleate boiling is studied in terms of its growth and departure from a superheated surface. The study considers the initial state of liquid to be either saturated or subcooled depending on the problem under investigation. Simulations have been performed considering the fluid to be incompressible. The properties of the fluid have been mentioned in Table 5.1 for water at atmospheric pressure. The computational domain utilized has been shown in Fig. 5.1. For initiation of the simulations, a bubble of radius 0.1 mm is placed at the cavity center (considered to be at the bottom-left corner of the domain). The boundary conditions have been incorporated following Sec. 2.8 considering the wettability of the surface at the bottom boundary. The initial thermal boundary layer thickness (δ_T) in the liquid phase is calculated following the correlation given by Kays and Crawford [170] as

$$\delta_T = 7.14(\nu_l \alpha_l / g\beta_T \Delta T)^{1/3}. \tag{5.1}$$

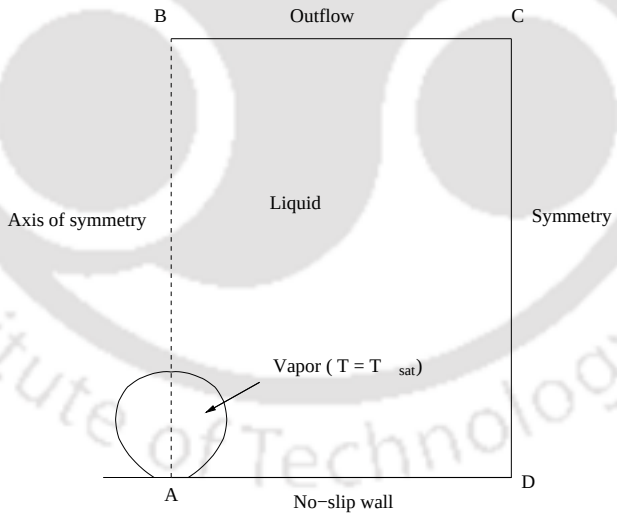

Figure 5.1: Schematic of the computational domain.

Two-dimensional axisymmetric problem has been considered by solving same set of governing equations as described in Sec. 2.1. However, the phase-change at the liquid-vapor interface is modelled as the jump condition incorporated in the modified

Table 5.1: Properties of water at atmospheric pressure ($P_{sat} = 1.01 \times 10^5 \text{N/m}^2$)

T_{sat} = 373.15 K; P_{sat} = 101.3 kPa; h_{lv} = 2260.0 kJ/kg; σ = 59.0 mN/m				
Phase	Density(ρ) (kg/m^3)	Viscosity(μ) ($\mu\text{N.s/m}^2$)	Conductivity(k) (W/m.K)	Specific heat(c_p) (kJ/kg.K)
Liquid	958.3	277.53	0.679	4.22
Vapor	0.597	12.60	0.025	2.03

continuity equation as

$$\int_{S_C} \mathrm{U} \cdot \hat{n} dS + \int_{S_I(t)} \left(\frac{1}{\rho_l} - \frac{1}{\rho_v} \right) \frac{|\mathrm{q}| \cdot \hat{n}}{h_{lv}} dS = 0 \tag{5.2}$$

The vapor generation occurs as a result of heat transfer from the superheated liquid to the bubble across the interface (q_{lv}) and due to the evaporation of the liquid microlayer underneath the bubble (q_{ml}). In Eq. 5.2, the term q is the summation of q_{lv} and q_{ml}. Details of the microlayer model used to calculate q_{ml} have been described in Sec. 2.7. A time-step of $\Delta t = 4 \times 10^{-7}$ s has been considered for all the simulations.

Incorporating the microlayer model, the present investigation demonstrates detailed simulations of a single bubble during its growth and departure from the surface. The effect of surface temperature on the bubble departure time and departure diameter has been discussed. Evaporation rate of the microlayer is compared at different levels of surface superheat. The study is further extended to show the effect of liquid subcooling on the dynamics of bubble growth. The analyses are performed to understand the behavior of the bubble after its departure from the heated surface under saturated and subcooled liquid ambience.

5.2 Grid Refinement Study

A grid convergence study has been performed for the bubble growth in case of contact angle of $\gamma = 50^\circ$ and $\Delta T = 8.5$ K. A comparison of the growth rate of the bubble with three different grid-meshes of 150×300, 200×400 and 250×500

has been depicted as the variation of diameter with time. Departure time and departure diameter have been compared in Fig. 5.2a among the results obtained from all the grid-meshes under observation. A change in departure time of 3.48% has been observed between the grid-meshes of 150×300 and 200×400 while 0.8% has been observed between 200×400 and 250×500. However, the change in departure diameter is observed to be 0.2% for the first case and 1.6% for the second case. Figure 5.2b illustrates the bubble profile at an instant of 0.001 s for all three grid-meshes. The profiles match closely for grid-meshes of 200×400 and 250×500 while for the 150×300 grid-mesh, the bubble profile has some difference with the other two cases at the same instant of time.

Considering the linear model for micro-layer thickness according to the Eq. 2.59, small deviations are acceptable with the change in grid size. For the present investigations, a grid mesh of 200×400 is utilized for the simulations domain as represented by the schematic in Fig. 2.59.

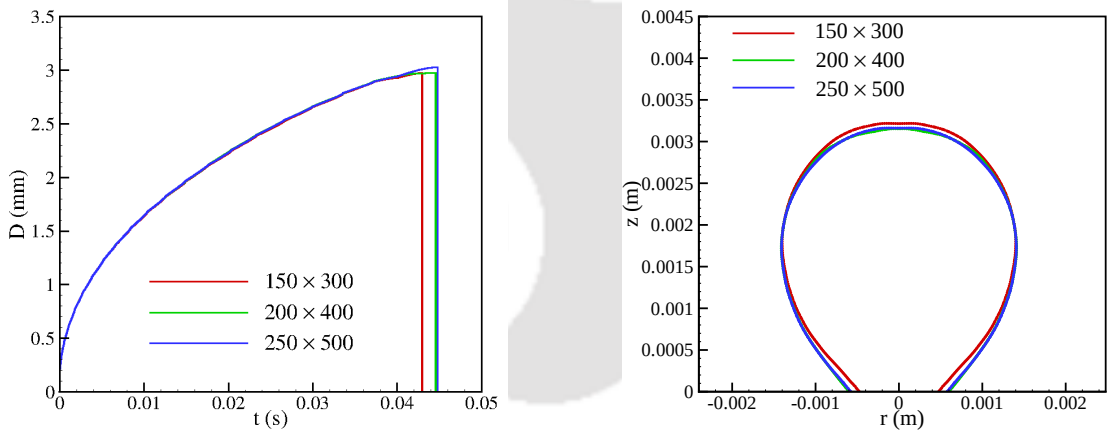

(a) (b)

Figure 5.2: (a) Variation of bubble diameter with time and (b) bubble profile at the time instant of 0.001 s for $\gamma = 50°$ and $\Delta T = 8.5$ K with three different grid-meshes.

5.3 Validation of the Model

The present approach for modelling of microlayer evaporation, requires an extensive numerical testing to determine the initial microlayer thickness for a specified surface wettability. In the present work, simulations for surface wettability corresponding to

contact angles of 38° and 50° have been peformed. The initial microlayer thickness has been obtained after several simulations to attain an acceptable match of the departure time and departure diameter with the available results in the literature. As the initial microlayer thickness is considered to be a function of the radial distance from the center of the cavity, its value depends on C_0 as mentioned in Eq.2.59. The values of C_0 in the present simulations have been considered as 2.81×10^{-2} and 2.51×10^{-2} for contact angles of 38° and 50°, respectively. Validations for growth

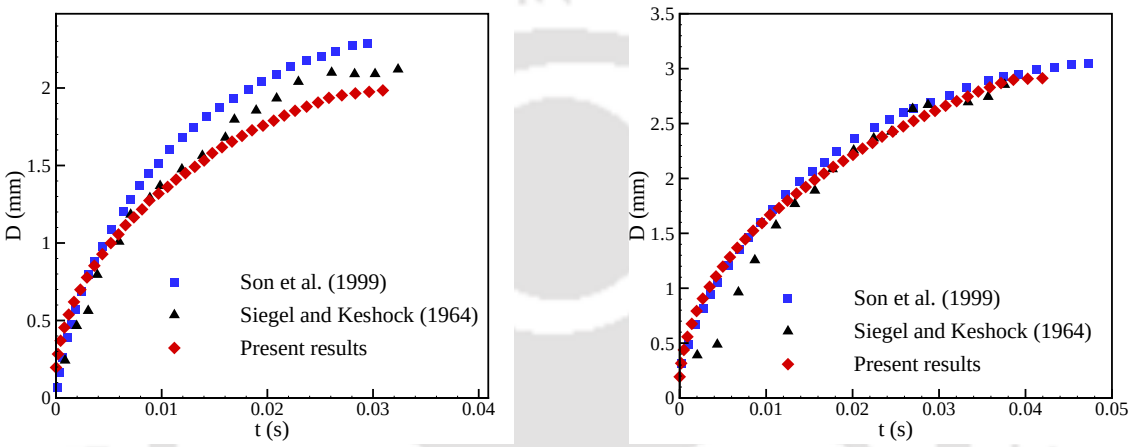

Figure 5.3: Variation of bubble diameter with time for (a) $\gamma = 38°$ and $\Delta T = 6.2$ K and (b) $\gamma = 50°$ and $\Delta T = 8.5$ K.

rates have been shown in the Fig. 5.3a and Fig. 5.3b. The growth rate of bubble starting from a pre-defined initial diameter upto the departure diameter, has been shown and compared with the numerical results from Son et al. [72] and experimental results of Siegel and Keshok [21].

5.4 Effect of Surface Superheat

The variation of growth rate with the changes in surface superheat has been shown in Fig. 5.4a for the contact angle of 38°. As can be observed, the bubble departure diameter increases and the departure time decreases with the increase in surface superheat. The departure diameter, as calculated from Eq. 1.11 for the contact angle of 38° is approximately equal to 1.9 mm. In the present simulations, we obtained a departure diameter of 1.95 mm for $\Delta T = 6.2$ K. This value increases with an

increase in superheat, as expected from the correlation mentioned in Eq. 1.12. As

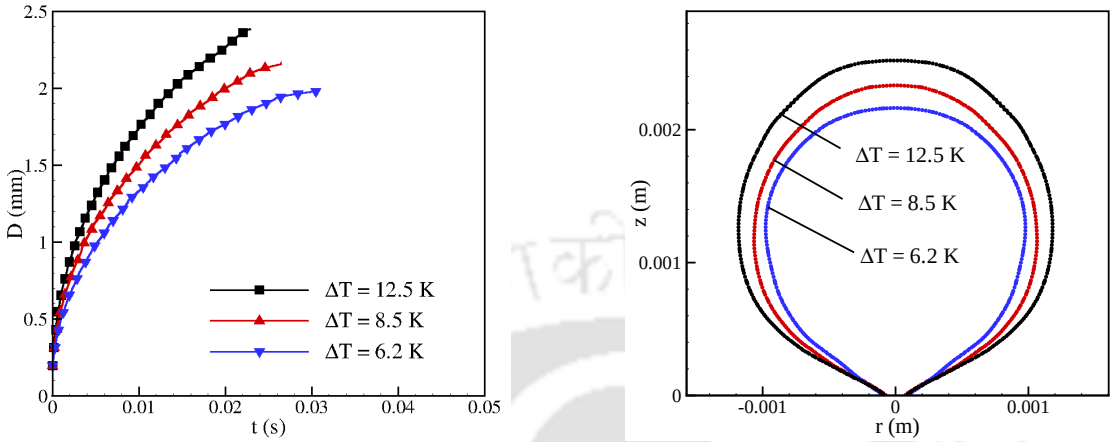

(a) (b)

Figure 5.4: Effect of superheat on (a) bubble growth rate and (b) bubble morphology just before departure for the contact angle of 38°.

can be observed from the Fig. 5.4a, bubble growth rate depends on the temperature difference between the vapor and the liquid phases which directly depends on the surface superheat. The growth of a bubble governed by temperature difference, is inherently a heat diffusion controlled phenomenon. According to Mikic et al. [56], the growth of a bubble can either be inertia dependent or heat diffusion dependent based on the pressure and temperature conditions inside the bubble and the outside ambient. During the heat diffusion controlled growth, diameter of bubble increases following the relation

$$D \propto t^n \tag{5.3}$$

For a heat diffusion controlled growth, the value of n as mentioned by Mikic et al. [56] is 1/2. We have plotted the growth rate obtained at different values of superheat and compared those with their corresponding power law fit curves following the relation as mentioned in Eq. 5.3. The values of exponent n was observed to be dependent on the values of superheat and its values obtained at every superheat are close to 1/2. The plots have been shown in Fig. 5.5.

The increase in superheat results in higher rate of vapor generation owing to faster evaporation of the microlayer and increased liquid superheat. The depletion of microlayer at the same instant of time for different levels of superheat can be ob-

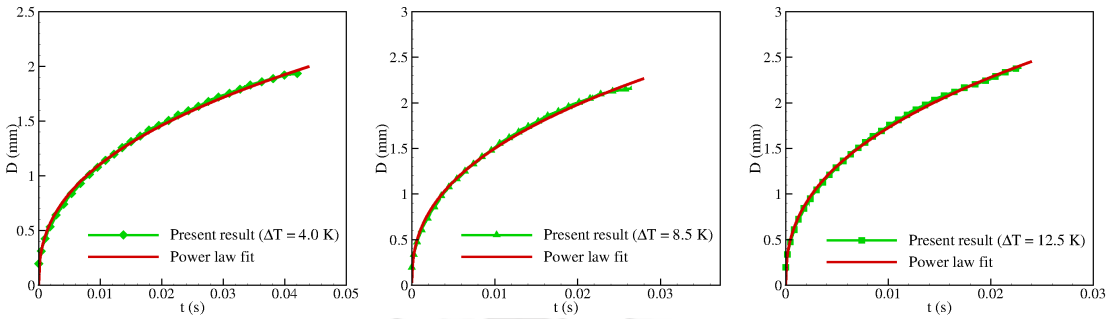

(a) $D \propto t^{0.3989}$ (b) $D \propto t^{0.401}$ (c) $D \propto t^{0.405}$

Figure 5.5: Comparison of growth rate of bubbles at different superheats of (a) 4 K (b) 8.5 K and (c) 12.5 K with the power law fit curves.

served from the Fig. 5.6a. The positive values in the plots represent the microlayer thicknesses at the corresponding radial location (r) from the center of nucleation. It can be observed that the values of microlayer thickness become zero at the depleted portion where the liquid inside the microlayer is completely evaporated. The thickness increases with the distance from the cavity center upto the location where interface contacts the solid wall, beyond which there is bulk liquid phase and therefore the values come down to zero again. It can also be observed that the microlayer depletion at the same instant of time is more in the case of higher superheats due to the higher rate of vaporization. Also, since the interface moves away faster from the cavity center in the case of higher superheats, the maximum value of microlayer thickness increases as the superheat increases. At a particular value of surface superheat, the variation in microlayer thickness with time can be observed from the Fig. 5.6b. Depletion of microlayer starting from the cavity center and its extension towards the contact point of liquid-vapor interface with solid surface can be again observed from the plots.

The growth of bubble results in increase in base radius; reaching a maximum value and after complete depletion of microlayer, the base-radius starts decreasing followed by departure from the heated surface. Fig. 5.7a shows the bubble profiles at different instants of time during the growth period. The figure shows that the bubble-height increases monotonically during the growth of the bubble while the base-radius increases for a certain period and then decreases continuously until the departure of the bubble. The above mentioned phenomenon is further illustrated via Fig. 5.7b, where a comparison of the variation of base-radius with time is presented.

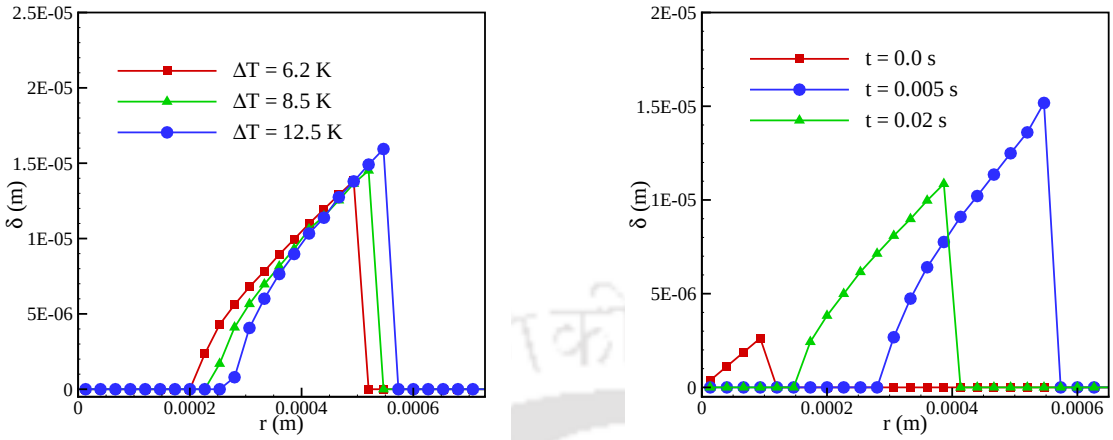

(a) (b)

Figure 5.6: Variation of microlayer thickness along the surface (a) at different values of superheat after 0.01 s of bubble initiation and (b) for the superheat value of $\Delta T = 6.2$ K at different instants of time for 38° contact angle.

The evaporation of microlayer leads to its depletion which contributes to the vapor generation. The rate of depletion of microlayer at various locations inside the bubble is plotted in Fig. 5.8a. As the distance increases from the center of the bubble, the time of depletion increases. This is obvious from the fact that the initial thickness of the microlayer increases with the distance from center. The vapor mass-flux variation from the microlayer at any instant of time during the bubble growth is shown in Fig. 5.8b. The variation of microlayer thickness at the same instant is also shown in the plot to better understand the variation of mass-flux distribution owing to the change in microlayer thickness at any location. The location of the microlayer with minimum thickness corresponds to the maximum heat-flux region and hence the maximum vapor mass flux.

A comparison of variation of wall heat-flux to the liquid side with time is shown in Fig. 5.9. The value of the heat-flux fluctuates around a constant value during the expansion stage of the bubble-base. When the bubble-base starts retracting back, the neighboring superheated liquid rushes towards the base of the bubble which causes rewetting of the dryout regions. This enhances the overall heat-flux value from the wall to the liquid which attains a maxima during the departure of the bubble from the surface.

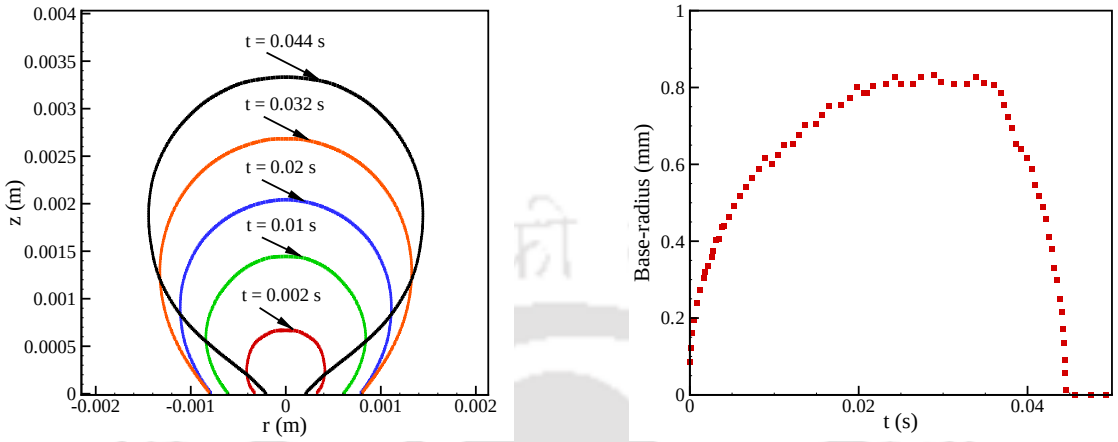

(a) (b)

Figure 5.7: (a) Interface profiles during the growth of a bubble at different instants of time and (b) variation of base-radius with time for 50° contact angle and ΔT_{sup} = 8.5 K.

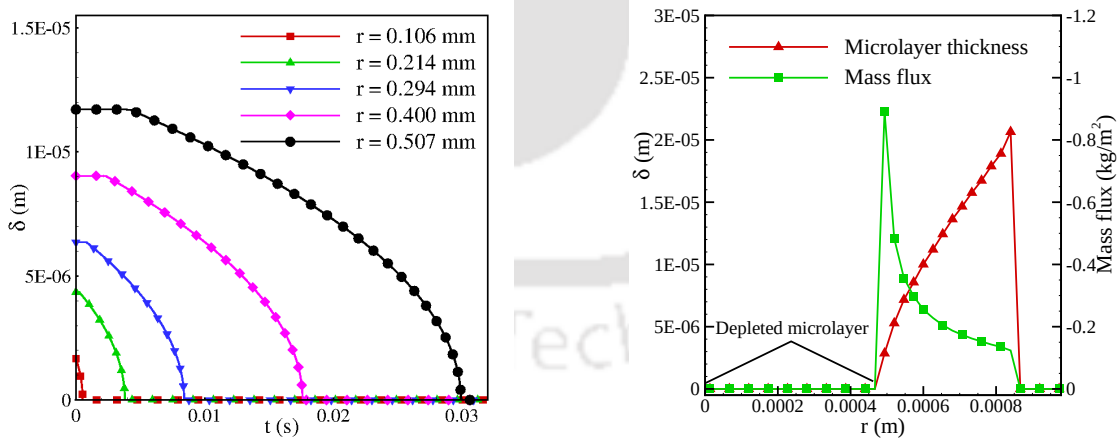

(a) (b)

Figure 5.8: (a) Variation of microlayer-thickness with time at different radial locations and(b) variation of mass-flux through the microlayer and thickness of the microlayer at $t = 0.032$ s for 50° contact angle and $\Delta T_{sup} = 8.5$ K.

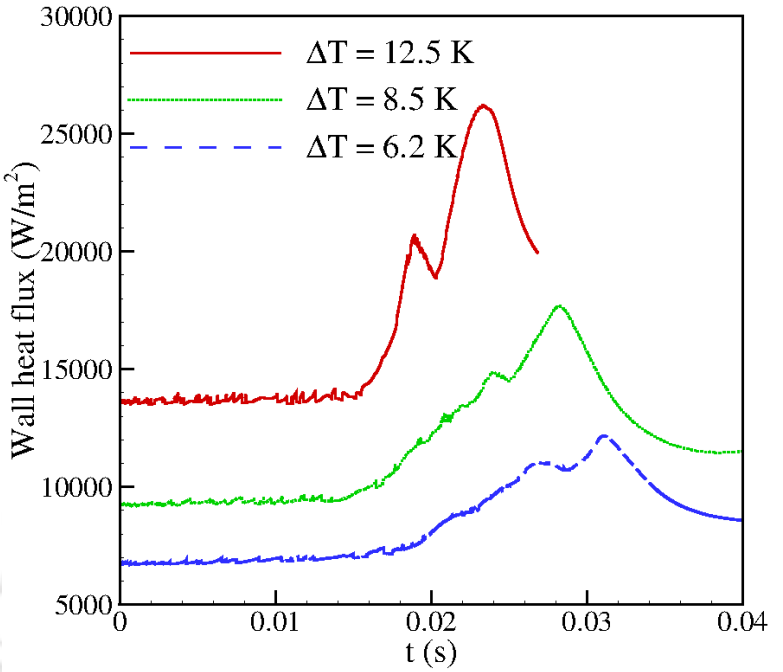

Figure 5.9: Comparison of wall heat-flux to the liquid side at different degrees of superheat for 38° contact angle.

5.5 Boiling under Subcooled Liquid

During the subcooled boiling conditions, the liquid temperature above the thermal boundary layer around the vapor bubble is lower than the saturation temperature. Most of the energy received from the heated wall contributes in the sensible heating of the liquid based on the degree of subcooling. As explained in Section 1, at certain values of subcooling and wall superheat, bubble grows and crosses the thermal layer. Its contact with the subcooled liquid results in vapor condensation at the top portion of the bubble.

Fig. 5.10 a and 5.10 b show a comparison of the present numerical results on subcooled boiling with the previous numerical and experimental results of Wu and Dhir [80] and Ramanujapu [79], respectively. The plots show the variation of bubble equivalent diameter with time for two different boiling conditions.

In the present results, the departure time of bubble from the heated surface in case of $\Delta T_{sub} = 1.5$ K is in close comparison with the other two illustrated results. For the subcooled condition of $\Delta T_{sub} = 4.0$ K, we observed a reduction in diameter of the bubble after attaining a maximum value and maintaining an almost constant

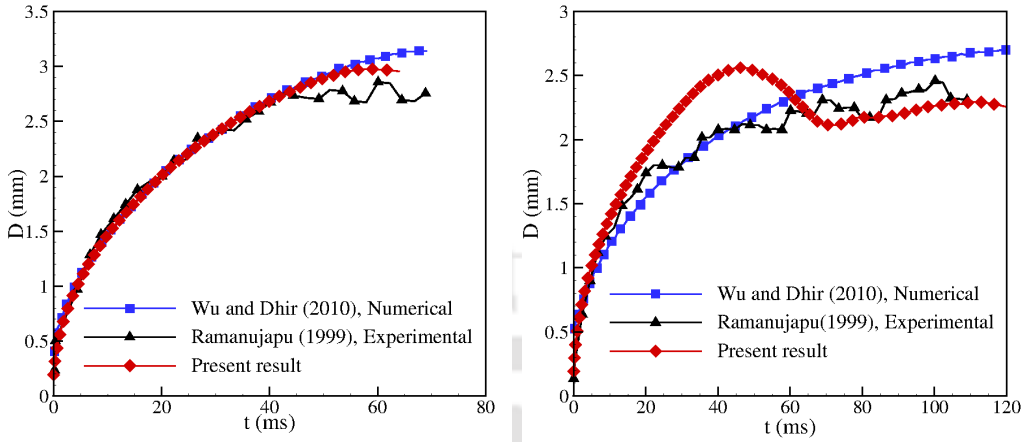

Figure 5.10: Variation of bubble equivalent diameter with time for (a) $\Delta T_{sub} = 1.5$ K and $\Delta T_{sup} = 7.0$ K and (b) $\Delta T_{sub} = 4.0$ K and $\Delta T_{sup} = 6.5$ K for 54° contact angle.

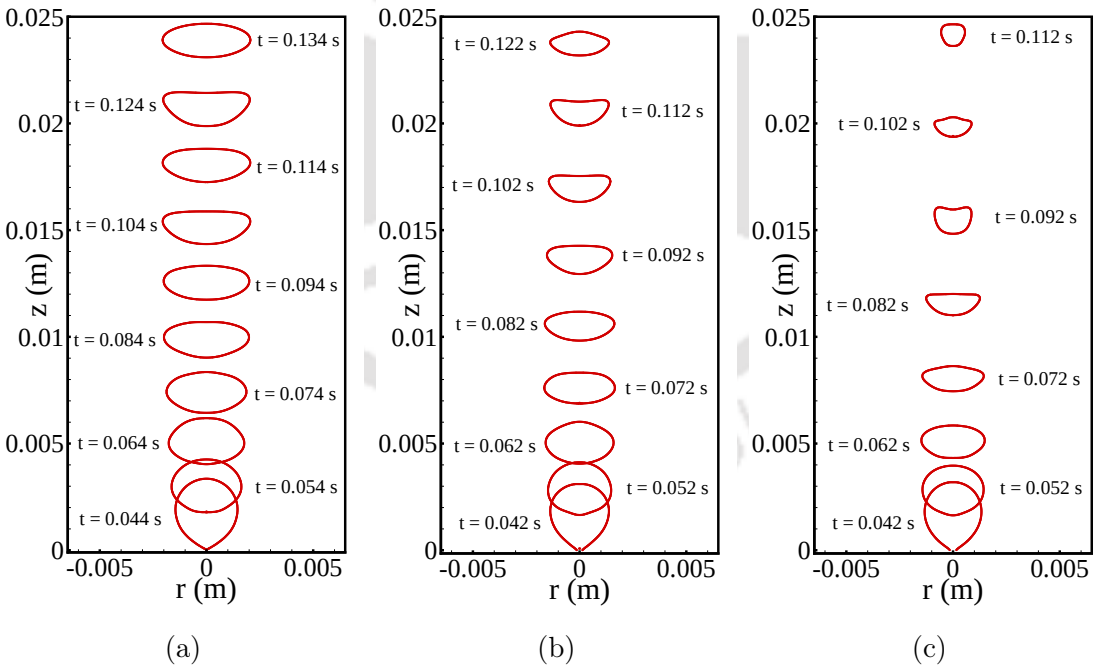

Figure 5.11: Profile of a bubble after the instant of departure from the surface in (a) saturated liquid condition, (b) subcooled condition of $\Delta T_{sub} = 1.5$ K and (c) subcooled condition of $\Delta T_{sub} = 3.0$ K for 50° contact angle.

value afterwards (Fig. 5.10 b). The bubble starts oscillating at its location over the heated surface and does not depart untill the observed time period of 120 ms. The oscillatory behavior of bubble diameter can be observed from the experimental data by Ramanujapu [79] although the numerical results by Wu and Dhir [80] observed a continuous rise in diameter for the given time, attaining an almost asymptotic value at the end.

From the simulations performed on subcooled boiling, it has been observed that the behavior of bubble growth and departure is highly dependent on the degree of subcooling and the surface conditions. Since there is a decrease in diameter during the final stage of bubble growth in case of subcooled boiling, the volume of bubble departed from the surface is always lower than in the saturated liquid conditions. The dynamics of the departed bubble, therefore, exhibit an appreciable variation in subcooled conditions. To observe the changes in bubble behavior after departure, a comparison is shown in the bubble profiles in the Fig. 5.11 between the saturated liquid condition and the subcooled condition of $\Delta T_{sub} = 1.5$ K and $\Delta T_{sub} = 3.0$ K.

For the saturated condition case (Fig. 5.11a), the volume of bubble remains constant after departure as is also observed from the Fig. 5.12a. On the other hand, the profile of the bubble shows complete different behavior in case of subcooled boiling conditions. There is a continuous decrease in volume of the bubble due to the condensation of vapor phase in the comparitively cooler liquid phase. In Fig. 5.12a, the plot compares the variation in diameter with time between the saturated and subcooled cases. The variation in diameter of bubble is shown from its growth to departure and after departure during its rise through the liquid phase. After the bubble departure in the subcooled conditions, volume of bubble reduces due to its condensation in the subcooled liquid. The rate of reduction of volume increases with increase in degree of subcooling from $\Delta T_{sub} = 1.5$ K to $\Delta T_{sub} = 3.0$ K.

Also, the variation in vertical velocity (rise velocity) of bubble after departure is plotted in Fig. 5.12b for the corresponding conditions. The velocity of bubble in all the conditions attains an initial jump due to the thrust provided by the bubble pinch-off from the surface. In the saturated liquid condition, the velocity attains an almost constant value with small flutuations. Whereas, in the subcooled boiling condition of $\Delta T_{sub} = 1.5$ K, there is a comparatively larger fluctuation in velocity for the same time duration of bubble-rise. The fluctuations in velocity of bubble further increases in case of subcooled condition of $\Delta T_{sub} = 3.0$ K as the rate of condensation is higher. The higher magnitude of velocity in subcooled conditions

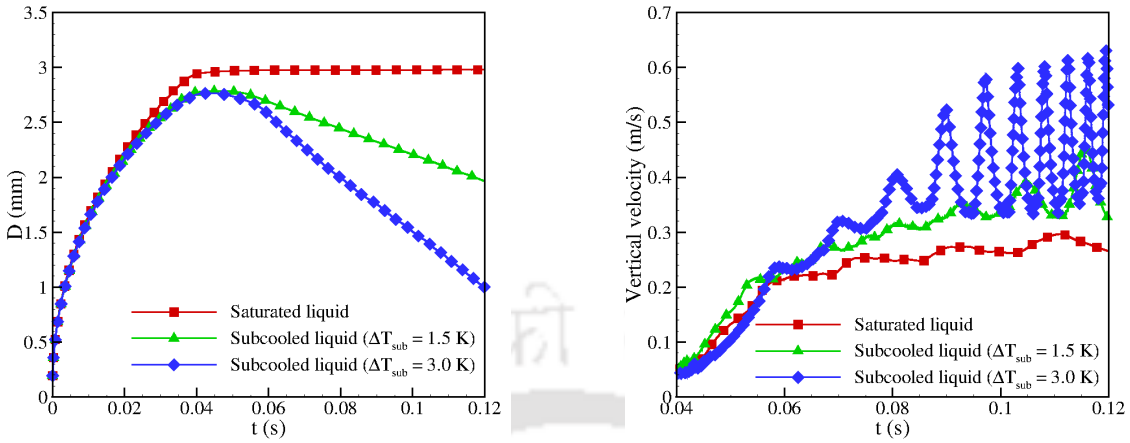

(a) (b)

Figure 5.12: Comparison of (a) diameter and (b) vertical velocity of bubble between saturated liquid condition and subcooled condition of $\Delta T_{sub} = 1.5$ K.

can be due to the conservation in momentum of the vapor volume with the effect of condensation considered. The increased rate of condensation affects the dynamics of bubble as a result of variations in drag force and buoyancy.

5.6 Summary

In this chapter, nucleate boiling of a single bubble has been studied and its growth, departure and after-departure dynamics have been analysed. Variation in growth rate and departure diameter of a bubble with change in substrate-superheat has been presented and been found to increase with the increase in superheat. Heat transfer leading to the generation of vapor occurs from superheated liquid to the bubble and also through the liquid-microlayer underneath the bubble. The contribution from the microlayer evaporation in bubble growth is separately modelled so as to satisfy the mass conservation near the interfacial region. The subcooling of the liquid has been found to affect the bubble growth significantly. Whether the bubble departs from the surface or continues to oscillate over the surface depends on the combined influence of evaporation due to superheated liquid layer and condensation at the bubble-top due to subcooled liquid. Bubble dynamics after departure from the surface is also found to be highly influenced by the subcooling of the liquid.

Chapter 6

Effect of Surface Wettability and Applied Electric Field on Transition from Film Boiling to Nucleate Boiling

The phenomenon of liquid-solid contact during the film boiling due to the effect of surface-wettability is the main focus in the present study. Numerical simulations during the film boiling show the collapse of vapor layer when the surface-wettability is sufficiently high, i.e. for a hydrophilic surface. The vapor film collapse results in liquid-contact with the heated surface which causes the boiling mode to shift towards the nucleate regime. The contact area of the liquid increases with time. In case of a hydrophobic surface or a surface with higher contact angle, such a transition is not observed. However, when a sufficiently strong electric field is applied across the liquid-vapor interface over a hydrophobic surface, the vapor film collapses and the system demonstrates a similar transition from film boiling to nucleate boiling. The required intensity of electric field at which the vapor film collapses, increases with the increase in surface-superheat.

6.1 Introduction and Definition of the Problem

In this chapter, the numerical results pertaining to the bubble growth during film boiling and the instabilities occurring at the interface as a result of the effect of surface-wettability have been presented. As a result of continuous vapor generation during film boiling, bubbles grow and are buoyed away periodically. During the pinch-off stage of the bubble, a thin neck forms near the base of bubble. The film thickness adjacent to the bubble at this stage attains a minimum value. At these locations and at these instants of time, the probability of liquid-solid contact is maximum. In chapter 1 (Sec. 1.3), the importance of surface wettability during transition boiling has been explained while discussing the research developed so far. Witte and Lienhard [102] have pointed out the influence of the contact angle exhibited by the interface over the surface and later Choudhury and Winterton [104] have clearly observed and explained the increase in heat-flux as the tendency of liquid wetting over the surface increases.

In the present work, the effect of wettability on the vapor-layer-collapse during film boiling - which may lead to the transition to nucleate boiling - has been presented. During the bubble formation stage in the film boiling regime, the vapor layer may become thin enough so as to allow the liquid to come in contact with the heated surface. This tendency of liquid-contact varies with the wettability of the surface. The following work demonstrates this phenomena through numerical simulations in film boiling regimes with varying contact angles of the solid surface. The effect of liquid-solid contact induced by an applied electric field has also been shown in case of low wettability surfaces.

Simulations have been performed using water near its critical pressure (Table. 3.1). The simulations are initiated with a thin layer of vapor having random thickness along the horizontal direction and a mean average height of $\lambda_B/8$. The domain-dimensions are proportional to the Berenson's critical wavelength [6], λ_B. The grid-dimension considered is $\Delta x = \Delta y = \lambda_B/240$ and the time-step used is $\Delta t = 5\times10^{-6}$. The governing equations for mass, momentum and energy conservation have been followed as described in Sec. 2.1 and boundary conditions are implemented as presented in Sec. 2.8, considering the wettability of the surface. Fluids are considered perfect dielectrics and the electric forces are calculated through the fomulation described in detail in Sec. 2.6. The present model focuses mainly on the liquid-solid contact during film boiling. The continuous nucleation of bubbles from the surface

have not been modelled due to the assumption of constant temperature of the liquid at saturation temperature.

6.2 Transition Due to High Surface-Wettability

Surfaces possessing high wettability have a higher affinity for water than surfaces with low wettability. Hence during the bubble departure, the tendency of the bulk-liquid to contact the heated-substrate increases in case of surfaces with higher wettability (or lower contact-angle). To demonstrate this phenomenon, the interface profiles during the bubble formation in film boiling are presented in Fig. 6.1 over a surface with contact angle of 38° (Fig. 6.1a) and 50° (Fig. 6.1b). It is clearly observed from the profiles that a regular bubble departure occurs in the case of contact angle $\gamma = 50°$ without liquid-solid contact at any location over the surface. Discrete bubbles emerge from the vapor film, maintaining a separation distance proportional to the critical wavelength (λ_c). However, in the case of $\gamma = 38°$, the vapor film ruptures before the pinch-off of the bubbles at certain locations leading to departure from the film boiling mode. The disintegration of the interface can be observed with independent bubbles over the surface which get buoyed away, accomodating the neighboring liquid to occupy their place over the surface.

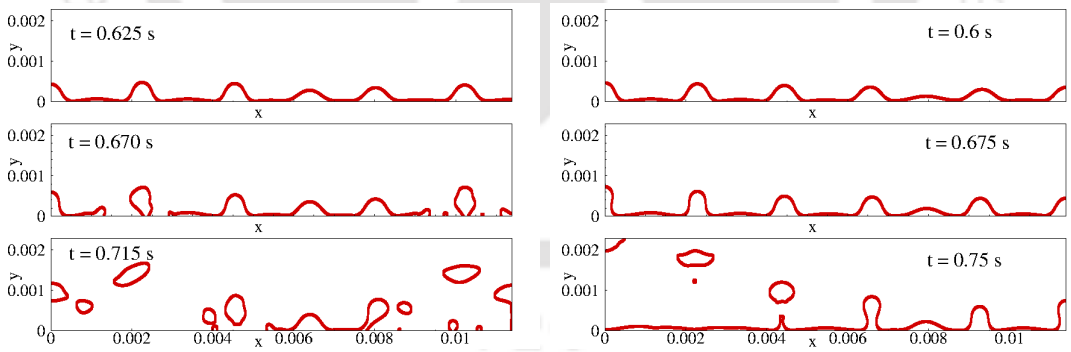

Figure 6.1: Interface profiles at different instants of time for (a) $\gamma = 38°$ and (b) $\gamma = 50°$ with $\Delta T = 5$ K.

Due to the liquid-solid contact, the vapor-fraction in contact with the surface starts decreasing and ultimately the entire surface gets covered with liquid. In the present context, the vapor-fraction is defined as the ratio of area of the superheated

surface occupied by vapor to the total area of the superheated surface (horizontal domain-length in the simulations). The variation of vapor-fraction with time is shown in Fig. 6.2. It can be observed that with the initiation of the liquid contact, the vapor-fraction starts decreasing abruptly due to the continuous detachment of bubbles from the surface.

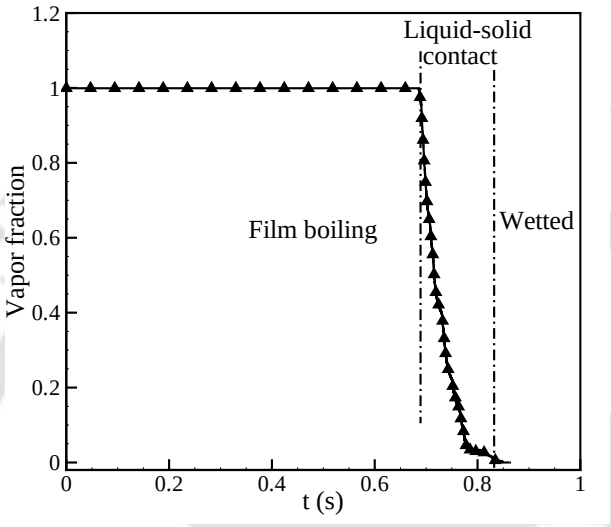

Figure 6.2: Variation of vapor fraction over the superheated surface ($\gamma = 38°$) with time.

The liquid-contact with the solid-surface at various locations results in a sudden increase in heat-flux from the surface. Figure 6.3 shows the variation of space-averaged heat flux over the surface for contact angles of $\gamma = 38°$ and $\gamma = 50°$. It can be observed from the plots that due to the rupture of vapor film in case of $\gamma = 38°$, the heat-flux increases significantly as compared to that in regular film boiling corresponding to $\gamma = 50°$. A frequent variation in heat-transfer results due to the intermittent liquid-contacts with the heated surface.

6.3 Electric Field Induced Transition

The high wettability, i.e. hydrophilic condition over the surface leads to the transition from film boiling to nucleate boiling regime. On the contrary, the film boiling regime continues in case of hydrophobic surfaces and the periodic release of bubbles is observed. These deductions can be made from the results in Sec. 6.2. However,

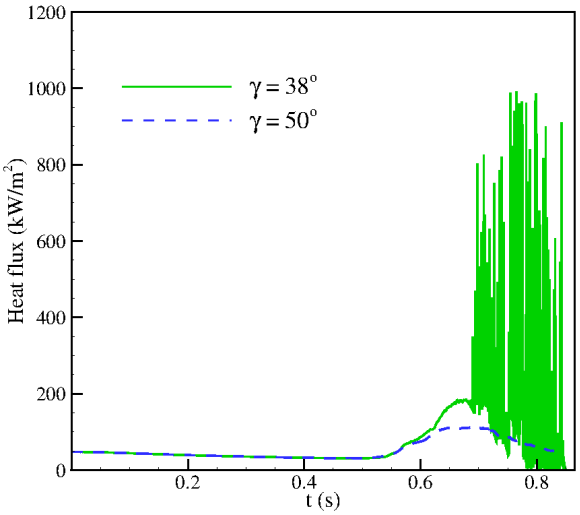

Figure 6.3: Variation of heat flux with time for different values of wettability.

with the application of sufficient intensity of the electric field (depends on the superheat) across the liquid-vapor interface, the frequency of bubble release is increased which results in decrease in the average height of the vapor film. The high frequency of bubble-release and decrease in average vapor-height makes the system vulnerable to liquid-solid contact at certain locations over the surface. The effect of electric field in attaining the transition in boiling over a hydrophobic surface can be observed from Fig. 6.4.

Figure 6.4 shows that regular film boiling prevails over the surface when the electrohydrodynamic forces are not acting ($E = 0$). With the application of electric field of intensity $E = 1 \times 10^5$ V/m, the bubble generation rate increases due to the increase in instabilities at the interface. The interface, in this condition is not ruptured and the liquid does not contact the solid surface. However, when the intensity of applied electric field is increased further ($E = 1.5 \times 10^5$ V/m), the transition can be clearly observed due to the liquid-solid contacts at various locations over the surface. An increased intensity of the applied electric field makes the interface more unstable which can be deduced from Eq. 1.2.

The transition of boiling regimes with the application of a specified intensity of electric field depends also on the degree of superheat of the surface. Figure 6.4 shows that the transition occurs over the surface with $\Delta T = 5$ K for an applied electric field intensity of 1.5×10^5 V/m. When the surface-superheat is increased to $\Delta T = 15$ K, a normal film boiling persists for the same electric field intensity of

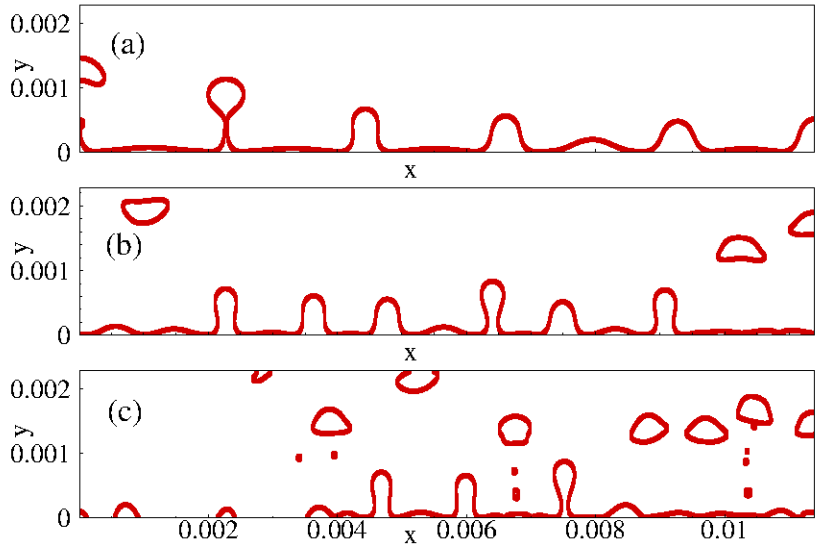

Figure 6.4: Morphology of bubbles over a surface with 120° contact-angle, $\Delta T = 5$ K and an applied electric field of strength (a) $E = 0$, (b) $E = 1 \times 10^5$ V/m and (c) $E = 1.5 \times 10^5$ V/m.

1.5×10^5 V/m and no liquid-solid contacts are observed. A comparison of the profiles of bubbles is shown in Fig. 6.5 for superheat values of $\Delta T = 5$ K and $\Delta T = 15$ K.

To clarify the effect of superheat, the temperature contours (Fig. 6.6) have been shown on a zoomed scale of the Fig. 6.5. It is to be noted that the simulations performed here focus mainly on observing the phenomena of liquid-solid contact during film boiling. The liquid temperature is considered to be at saturation temperature throughout the simulations and hence, the complete scenario of nucleate boiling after film rupture is not accommodated.

The transition to nucleate regime depends on the balance between the rate of vapor generation and vapor release. At higher values of superheat, the rate of bubble generation increases, thus, maintaining the appropriate vapor-film-thickness and preventing the liquid from rupturing the interface. A comparatively higher intensity of electric field is required to bring the liquid-solid contacts into effect in case of higher superheat-values over a hydrophobic surface. This is illustrated in Fig. 6.7. The vapor film does not rupture even with the application of an electric field of intensity 2×10^5 V/m. With a further increase in intensity to 2.5×10^5 V/m, the transition occurs and the bubbles disintegrate from the vapor film to form discrete bubbles.

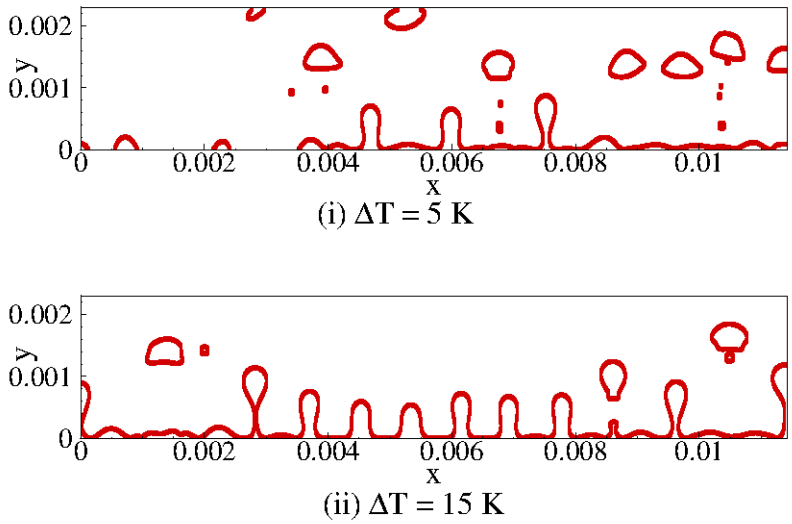

Figure 6.5: Interface profiles during the first set of bubble-departure over a surface ($\gamma = 120°$) with different values of superheat and with an applied electric field of intensity $E = 1.5 \times 10^5$ V/m

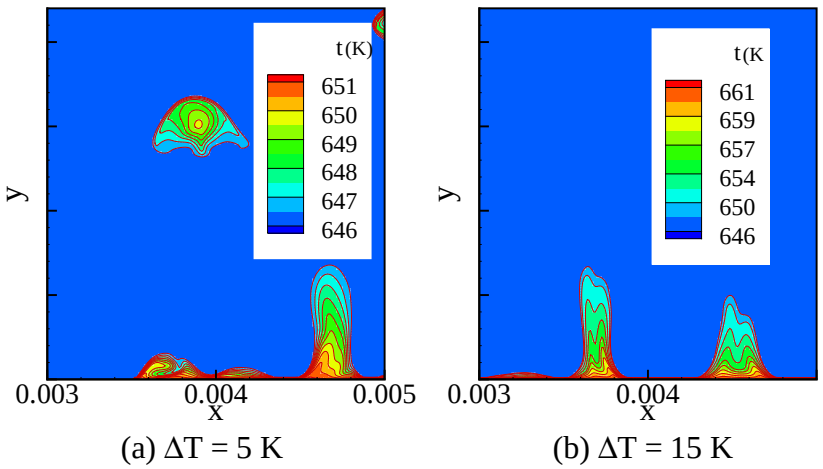

Figure 6.6: Temperature contours at a zoomed view for both the cases in Fig. 6.5.

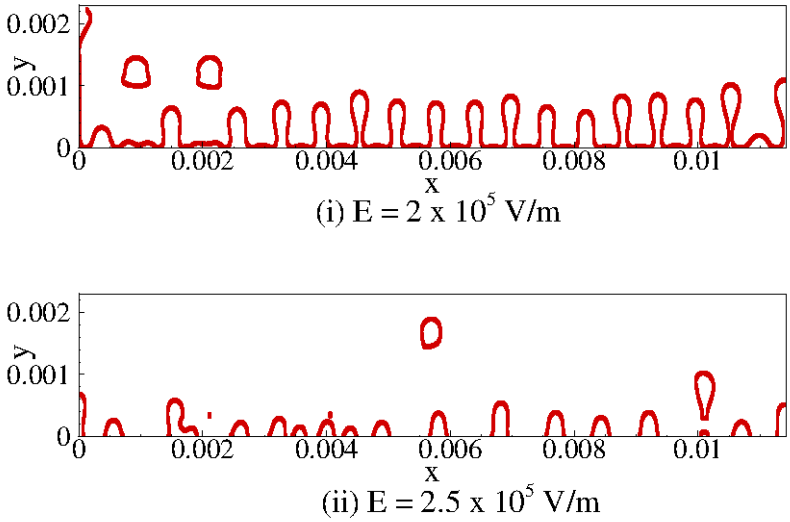

Figure 6.7: Bubble growth over a surface ($\gamma = 120°$) with $\Delta T = 15$ K and with different values of applied electric field.

6.4 Effect of Biphilic Surface

To observe the changes in boiling characteristics as a result of different wettability of the heated substrate, simulations have been performed over a surface exhibiting variation in wettability along its length, i.e. a surface having biphilic nature. Since hydrophilic and hydrophobic surfaces show different behaviors during transition boiling, a part of the surface is considered hydrophilic ($\gamma = 30°$) while the remaining part is considered hydrophobic ($\gamma = 120°$) for the simulations. The results obtained have been illustrated in Fig. 6.8 depicting the interface profiles at different instants of time.

Once the hydrophilic region comes in contact with the liquid, vapor generation is mostly limited to the hydrophobic region where a thin layer of vapor-film is still present over the surface. The initiation of liquid-contact can be seen in Fig. 6.8b. However, the liquid-vapor front continues to move towards the hydrophobic side due to the motion of bulk-liquid. The vapor film in the hydrophobic region remains prominent throughout the simulation and a continuous release of discrete bubbles can be observed through the vapor layer over the hydrophobic region.

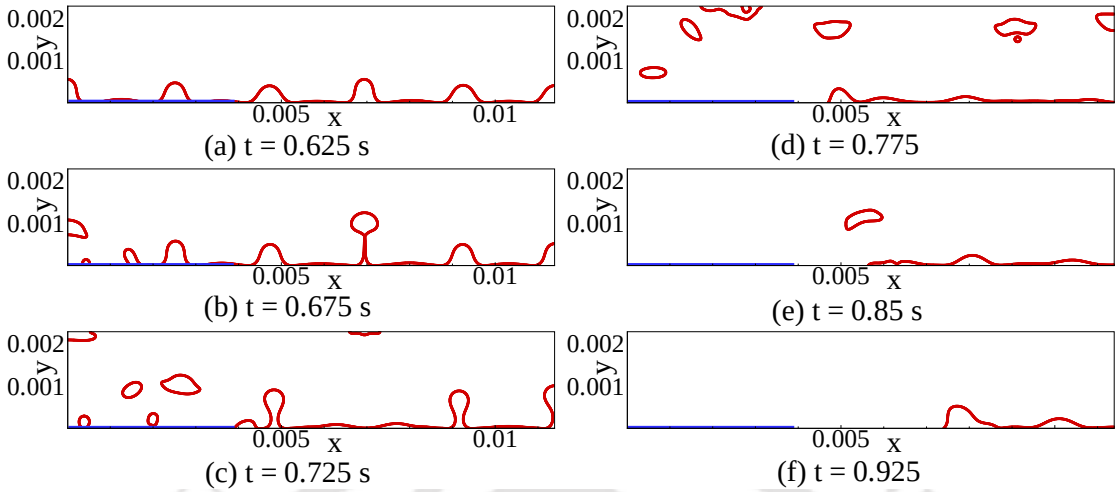

Figure 6.8: Liquid-solid contact over a biphilic surface. Contact starts preferably at hydrophilic region (blue lines) while the hydrophobic region still covered with vapor.

6.5 Summary

The study performed in this chapter has been focused upon the effects of surface-wettability and applied electric field on the intermittent liquid-solid contacts during saturated film boiling. When the wettability of the surface was considered in the simulations of saturated film boiling, it was observed that sufficiently high surface-wettability prompts vapor-film rupture, which results in transition from film boiling to nucleate boiling regime. The analyses have been performed for various wettabilities of the surface, considering both hydrophilic and hydrophobic behavior. Although a hydrophobic surface does not show any transition, application of an external electric field of sufficient intensity is found to induce the transition over such surfaces as well.

Chapter 7

Conclusions and Future Perspectives

In the present thesis, direct numerical simulations have been performed to analyse the dynamics of vapor bubbles formed during various regimes of boiling. The occurrence of continuous interface-deformation during bubble growth governs the heat-transfer rate in boiling. Irrespective of the mode of boiling, the interface-capturing technique (CLSVOF) has been found to depict the growth dynamics of bubbles accurately. Finally, the heat-transfer rate associated with the phenomena is predicted.

7.1 Conclusions

The objectives of the present investigations have been defined based on the research done so far, where various factors affecting the mechanism of bubble growth during film boiling and nucleate boiling have been discussed. The numerical techniques used for interface-capturing, modelling of the surface tension and electric force and microlayer evaporation model required for nucleate boiling have been explained elaborately.

In accordance with the investigations performed on saturated film boiling, the following conclusive remarks can be drawn,

- Starting from the isolated effect of wall superheat, the study demonstrates the change in bubble formation modes and heat transfer characteristics at various values of superheats. At higher superheat of 22 K, alternate formation of vapor

columns at nodes and discrete bubbles at the anti-nodes is observed confirming the experimental observations of Reimann and Grigull [1] and numerical results of Son and Dhir [166]. The isolated effect of an electric field at a given superheat shows the enhancement in heat transfer rate due to the increase in bubble release frequency. The experimental and analytical observations of Verplaetsen and Berghmans [12] for the effect of electric field on maximum bubble height are also validated. The maximum bubble height is found to be almost invariant with applied electric field. The lateral deformation in bubbles leads to the decrease in bubble radius with increasing electric field values.

- The inclusion of electric field at different superheats, shows the changes in the evolution patterns of interface. Discrete bubble formation with increasing release rate and decrease in bubble spacing is observed at lower superheat with increased value of the electric field. The bubble release loses its temporal periodicity with the higher value of electric field intensity (2×10^5 V/m) but spatial periodicity remain unaffected. At even higher intensities of the electric field, the bubble release rate becomes aperiodic which is otherwise periodic at a lower superheat and without electric field effects. At higher electric field values, i.e. for $\frac{3(\rho_l - \rho_v)g\sigma}{f^2} << 1$ and at a lower value of superheat, vapor film ruptures leading to onset of the transition from film boiling to nucleate boiling.

- At higher superheat values, i.e. above 18 K, higher intensity of the electric field (3×10^5 V/m) results in formation of an increased number of vapor columns which interact and merge together entailing spatially aperiodic bubble release. Johnson's [9] hypothesis of existence of a minimum electric field intensity to cause a significant effect on boiling characteristics is confirmed through our simulations. The variation in bubble separation distance is presented and compared with the theoretical correlations for varying electric field intensities. The applied electric field decreases the bubble separation distance enormously and thus, the heat transfer rate increases due to the increased convection currents and vigorous intermixing of vapor and liquid phases.

In continuation with the investigation of bubble formation during saturated film boiling, the work has been extended to the study of variation in boiling mechanism as a result of reduced gravity. Several important conclusions can be drawn based on the investigations performed, such as,

- Based on the direct numerical simulation of saturated film boiling at various gravity levels, it is found that with the reduction in gravity level, the length and time scales of the boiling phenomena increase substantially. The bubble size and height in reduced gravity level is much larger than those at normal gravity level. The heat transfer rate deteriorates as the gravity-level decreases. The inclusion of electric field in reduced gravity restores the value of heat flux commensurate with the normal gravity condition. The imposed electric field also reduces the separation distance between adjacent bubble formation sites and the frequency of bubble release is increased. Thus, the application of an electric field can be considered a strategic technique to enhance or control the heat transfer rate under reduced gravity conditions.

- Comparative study of the effect of gravity-level on the film boiling phenomena with an imposed electric field intensity shows that the dominance of electric field on the process enhances with the reduction in gravity. This has been observed from the morphological changes (lateral merger of the bubbles) and the heat transfer characteristics. The percentage change in heat flux due to imposed electric field is observed to increase with the reduction in gravity.

- The study of the interface profile during the bubble growth period showed that the bubble profiles at different instants of time tend to overlap with each other if a proper scaling law is defined for length and time. The values of the scaling exponents depend on the degree of superheat as the governing instability mode changes with the superheat value. The interface, thus exhibits self-similarity behavior during the linear stage of bubble growth.

The numerical simulation of the growth of a single bubble during nucleate pool boiling in a stagnant liquid has been performed and validated. The major conclusions that can be drawn as a result of observations obtained are as follows,

- A microlayer model is incorporated to include the effect of the thin layer of liquid which evaporates during the boiling process. During the growth of a bubble, the variation in thickness of the microlayer has been presented and is analysed in detail at different degrees of superheat. The growth rate of the bubble is shown to be dependent on the surface-superheat and the variation of wall-heat flux is shown to increase with an increase in the degree of superheat.

- The simulations performed under subcooled liquid conditions showed a significant variation in boiling behavior. For a lower value of liquid subcooling ($\Delta T_{sub} = 1.5$ K), the bubble showed a decrease in growth rate before departure. Whereas at comparatively higher subcooled value ($\Delta T_{sub} = 4.0$ K), the bubble ceases to depart from the surface and starts oscillating at its maximum volume.

- The dynamics of the bubble after departure showed different behaviors under saturated and subcooled liquid conditions. While the bubble volume remains constant after departure in case of saturated condition, the volume decreases appreciably with time in case of subcooled condition. The condensation of vapor bubble after departure in subcooled boiling prevents the bubble from attaining its terminal velocity and shows significant jump and oscillations in its rising velocity due to continuous change in its shape and volume.

The phenomenon of transition-boiling as a result of liquid-solid contact during film boiling due to high surface-wettability has been studied. The observations and conclusions are as follows,

- It was found from the simulations that the liquid-contacts are more prominent when the surface is more hydrophilic as compared to those when it is hydrophobic. Once the liquid contacts the heated surface, the mechanism of bubble generation transforms from film boiling to nucleate boiling. A sudden enhancement in heat-transfer rate is observed as a result of liquid-solid contact.

- Although regular film boiling prevails in case of boiling over a hydrophobic surface, the instability induced by the application of an electric field at the liquid-vapor interface results in an enhanced vapor release-rate and decrease in average film-height which may result in vapor-film-rupture. Thus, depending on the degree of superheat and the intensity of the applied electric field, the transition may also occur over the hydrophobic surface. A comparatively higher intensity of electric field is required for the vapor film to rupture in case of higher degree of superheat.

- The effect of surface-wettability induced transition is shown more prominently by studying boiling over a biphilic surface. The liquid-solid contact starts

preferably over the hydrophilic region while the hydrophobic surface remains covered with the vapor film.

7.2 Future Perspectives

In the context of the outcomes of the present investigations, further scope for study related to the various thermal and dynamical aspects of boiling can be defined in the following way

- In saturated film boiling conditions, the effect of liquid subcooling can be analyzed to explore the variation in boiling behavior in terms of bubble growth rate and heat transfer rate. Unlike the present study where the saturated liquid condition allows for the assumption of constant temperature, in the case of subcooled conditions, the variation in temperature of the liquid due to sensible heating also has to be considered.
- During nucleate boiling, the effect of temperature gradient along the interface is likely to culminate in the tangential component of the capillary force to act at the interface. This leads to Marangoni convection in the surrounding liquid which may change the dynamics of bubble growth.
- The application of an external electric field during nucleate boiling can be studied with focus on the variation in growth rate of the bubble and thus analyze the possibility of enhancing the time period of nucleate boiling.

References

[1] Reimann M. and Grigull U. (1975) 'Wärmeübergang bei freier konvektion und filmsieden im kritischen gebiet von wasser und kohlendioxid', *Wärme - und Stoffübertragung*, vol. 8(4), pp. 229–239.

[2] Carey V.P., *Liquid-Vapor Phase-Change Phenomena* (Taylor and Francis Group, LLC, 2008), 2nd Ed.

[3] Tomar G., Biswas G., Sharma A., and Welch S.W.J. (2008) 'Multimode analysis of bubble growth in saturated film boiling', *Physics of Fluids*, vol. 20(9), p. 092101.

[4] Zuber N. (1959) *Hydrodynamic Aspects of Boiling Heat Transfer*, Ph.D. thesis, University of California, Los Angeles.

[5] Panzarella C.H., Davis S.H., and Bankoff S.G. (2000) 'Nonlinear dynamics in horizontal film boiling', *Journal of Fluid Mechanics*, vol. 402, pp. 163–194.

[6] Berenson P.J. (1961) 'Film boiling heat transfer from a horizontal surface', *Journal of Heat Transfer*, vol. 83, pp. 351–356.

[7] Griffiths D.J., *Introduction to Electrodynamics* (Pearson Education, Inc., 2006), 3rd Ed.

[8] Tomar G., Gerlach D., Biswas G., Alleborn N., Sharma A., Durst F., Welch S., and Delgado A. (2007) 'Two-phase electrohydrodynamic simulations using a volume-of-fluid approach', *Journal of Computational Physics*, vol. 227(2), pp. 1267–1285.

[9] Johnson R.L. (1968) 'Effect of an electric field on boiling heat transfer', *AIAA Journal*, vol. 6, pp. 1456–1460.

[10] Jones T.B. and Schaeffer R.C. (1976) 'Electrohydrodynamically coupled minimum film boiling in dielectric liquids', *AIAA Journal*, vol. 14(12), pp. 1759–1765.

[11] Verplaetsen F.M. and Berghmans J.A. (1997) 'The influence of an electric field on the heat transfer during film boiling of stagnant fluids rate', *Revue générale de thermique*, vol. 37, pp. 83–88.

[12] Verplaetsen F.M. and Berghmans J.A. (1999) 'Film boiling of an electrically insulating fluid in the presence of an electric field', *Heat and Mass Transfer*, vol. 35, pp. 235–241.

[13] Klimenko V.V. (1981) 'Film boiling on a horizontal plate - new correlation', *International Journal of Heat and Mass Transfer*, vol. 24(2), pp. 69–79.

[14] Oka T., Abe Y., Mori Y.H., and Nagashima A. (1995) 'Pool boiling of n-pentane, CFC-113 and water under reduced gravity: Parabolic flight experiments with a transparent heater', *Journal of Heat Transfer*, vol. 117, pp. 408–417.

[15] Zell M., Straub J., and Vogel B. (1989) 'Pool boiling under microgravity', *PCH. Physicochemical hydrodynamics*, vol. 11, pp. 812–823.

[16] Oka T., Abe Y., Tanaka K., Mori Y.H., and Nagashima A. (1992) 'Observational study of pool boiling under microgravity', *JSME International Journal, Series 2: Fluids Engineering, Heat Transfer, Power, Combustion, Thermophysical Properties*, vol. 35(2), pp. 280–286.

[17] Lienhard J.H. (1985) 'On the two regimes of nucleate boiling', *Journal of Heat Transfer*, vol. 107(1), pp. 262–264.

[18] Moissis R. and Berenson P.J. (1963) 'On the hydrodynamic transitions in nucleate boiling', *Journal of Heat Transfer*, vol. 85, pp. 221–226.

[19] Siegel R. and Usiskin C. (1959) 'A photographic study of boiling in the absence of gravity', *Journal of Heat Transfer*, vol. 81, pp. 230–236.

[20] Usiskin C. and Siegel R. (1961) 'An experimental study of boiling in reduced and zero gravity fields', *Journal of Heat Transfer*, vol. 83, pp. 243–253.

[21] Siegel R. and Keshock E.G. (1964) 'Effects of reduced gravity on nucleate boiling bubble dynamics in saturated water', *AIChE Journal*, vol. 10(4), pp. 509–517.

[22] Merte Jr H. and Clark J.A. (1964) 'Boiling heat transfer with cryogenic fluids at standard, fractional, and near-zero gravity', *Journal of Heat Transfer*, vol. 86, pp. 351–358.

[23] Lee H.S., Merte Jr H., and Chiaramonte F. (1997) 'Pool boiling curve in microgravity', *Journal of Thermophysical Heat Transfer*, vol. 11(2), pp. 216–222.

[24] Kim J. and Benton J.F. (2002) 'Highly subcooled pool boiling heat transfer at various gravity levels', *International Journal of Heat and Fluid Flow*, vol. 23(4), pp. 497–508.

[25] Raj R., Kim J., and McQuillen J. (2009) 'Subcooled pool boiling in variable gravity environments', *Journal of Heat Transfer*, vol. 131(9), p. 091502.

[26] Straub J. (1994) 'The role of surface tension for two-phase heat and mass transfer in the absence of gravity', *Experimental Thermal and Fluid Science*, vol. 9(3), pp. 253 – 273.

[27] Straub J. (2000) 'Microscale boiling heat transfer under 0g and 1g conditions', *International Journal of Physical Sciences*, vol. 39(4), pp. 490–497.

[28] Marek R. and Straub J. (2001) 'The origin of thermocapillary convection in subcooled nucleate pool boiling', *International Journal of Heat and Mass Transfer*, vol. 44(3), pp. 619–632.

[29] Shatto D.P. and Peterson G. (1999) 'Pool boiling critical heat flux in reduced gravity', *Journal of Heat Transfer*, vol. 121(4), pp. 865–873.

[30] Qiu D.M., Dhir V.K., Chao D., Hasan M.M., Neumann E., Yee G., and Birchenough A. (2002) 'Single-bubble dynamics during pool boiling under low gravity conditions', *Journal of Thermophysics and Heat Transfer*, vol. 16(3), pp. 336–345.

[31] Abarajith H.S., Dhir V.K., and Son G., 'Numerical simulation of the dynamics of multiple bubble merger during pool boiling under reduced gravity

conditions', in 'Proceedings of 7th Japan-US Seminar on Two-Phase Flow Dynamics, Moriyama, Japan', (2004), pp. 467–475.

[32] Dhir V.K., Warrier G.R., Aktinol E., Chao D., Eggers J., Sheredy W., and Booth W. (2012) 'Nucleate pool boiling experiments (NPBX) on the international space station', *Microgravity Science and Technology*, vol. 24(5), pp. 307–325.

[33] Aktinol E., Warrier G.R., and Dhir V.K. (2014) 'Single bubble dynamics under microgravity conditions in the presence of dissolved gas in the liquid', *International Journal of Heat and Mass Transfer*, vol. 79, pp. 251 – 268.

[34] Warrier G.R., Dhir V.K., and Chao D.F. (2015) 'Nucleate pool boiling experiment (NPBX) in microgravity: International space station', *International Journal of Heat and Mass Transfer*, vol. 83, pp. 781 – 798.

[35] Wan S.X. and Zhao J.F. (2008) 'Pool boiling in microgravity: Recent results and perspectives for the project depa-sj10', *Microgravity Science and Technology*, vol. 20(3-4), pp. 219–224.

[36] Zhao J.F., Li J., Yan N., and Wang S.F. (2009) 'Bubble behavior and heat transfer in quasi-steady pool boiling in microgravity', *Microgravity Science and Technology*, vol. 21(1), pp. 175–183.

[37] Verplaetsen F.M. and Berghmans J.A. (1997) 'The influence of an electric field on the heat transfer rate during film boiling of stagnant fluids', *Revue générale de thermique*, vol. 37, pp. 83–88.

[38] Di Marco P. and Grassi W. (2002) 'Motivation and results of a long-term research on pool boiling heat transfer in low gravity', *International Journal of Physical Sciences*, vol. 41(7), pp. 567–585.

[39] Carrica P., Di Marco P., and Grassi W. (1996) 'Electric field effects on film boiling on a wire', *Experimental Heat Transfer*, vol. 9(1), pp. 11–27.

[40] Di Marco P., Grassi W., and Trentavizi F. (2001) 'Pool film boiling experiments on a wire in low gravity', *Annals of the New York Academy of Sciences*, vol. 974(1), pp. 428–446.

[41] Markels M. and Durfee R.L. (1964) 'The effect of applied voltage on boiling heat transfer', *AIChE Journal*, vol. 10(1), pp. 106–110.

[42] Lovenguth R.F. and Hanesian D. (1971) 'Boiling heat transfer in the presence of nonuniform, direct current electric fields', *Industrial and Engineering Chemistry Fundamentals*, vol. 10(4), pp. 570–576.

[43] Cooper P. (1990) 'EHD enhancement of nucleate boiling', *Journal of Heat Transfer*, vol. 112(2), pp. 458–464.

[44] Judd R. (1999) 'The role of bubble waiting time in steady nucleate boiling', *Journal of Heat Transfer*, vol. 121, pp. 852–855.

[45] Kurihara H. and Myers J. (1960) 'The effects of superheat and surface roughness on boiling coefficients', *AIChE Journal*, vol. 6(1), pp. 83–91.

[46] Hsu Y. (1962) 'On the size range of active nucleation cavities on a heating surface', *Journal of Heat Transfer*, vol. 84(3), pp. 207–213.

[47] Rohsenow W.M. (1951) 'A method of correlating heat transfer data for surface boiling of liquids', Tech. rep., Cambridge, Mass.: MIT Division of Industrial Cooporation,[1951].

[48] Tien C. (1962) 'A hydrodynamic model for nucleate pool boiling', *International Journal of Heat and Mass Transfer*, vol. 5(6), pp. 533–540.

[49] Zuber N. (1963) 'Nucleate boiling. the region of isolated bubbles and the similarity with natural convection', *International Journal of Heat and Mass Transfer*, vol. 6(1), pp. 53–78.

[50] Lienhard J.H. and Wong P.T.Y. (1963) 'The dominant unstable wavelength and minimum heat flux during film boiling on a horizontal cylinder', *Journal of Heat Transfer*, vol. 86, pp. 220–226.

[51] Forster H. and Zuber N. (1955) 'Dynamics of vapor bubbles and boiling heat transfer', *AIChE Journal*, vol. 1(4), pp. 531–535.

[52] Fritz W. (1935) 'Maximum volume of vapor bubbles', *Physikalische Zeitschrift*, vol. 36, pp. 379–384.

[53] Cole R. (1967) 'Bubble frequencies and departure volumes at subatmospheric pressures', *AIChE Journal*, vol. 13(4), pp. 779–783.

[54] Liaw S.P. and Dhir V.K. (1989) 'Void fraction measurements during saturated pool boiling of water on partially wetted vertical surfaces', *Journal of Heat Transfer*, vol. 111(3), pp. 731–738.

[55] Wang C. and Dhir V.K. (1993) 'Effect of surface wettability on active nucleation site density during pool boiling of water on a vertical surface', *Journal of Heat Transfer*, vol. 115(3), pp. 659–669.

[56] Mikic B., Rohsenow W., and Griffith P. (1970) 'On bubble growth rates', *International Journal of Heat and Mass Transfer*, vol. 13(4), pp. 657–666.

[57] Lien Y.C. (1969) *Bubble growth rates at reduced pressure.*, Ph.D. thesis, Massachusetts Institute of Technology.

[58] Moore F.D. and Mesler R.B. (1961) 'The measurement of rapid surface temperature fluctuations during nucleate boiling of water', *AIChE Journal*, vol. 7(4), pp. 620–624.

[59] Hendricks R.C. and Sharp R.R., *Initiation of cooling due to bubble growth on a heating surface*, NASA technical note (National Aeronautics and Space Administration, 1964).

[60] Sharp R. and Center L.R., *The nature of liquid film evaporation during nucleate boiling*, NASA technical note (National Aeronautics and Space Administration, 1964).

[61] Jawurek H. (1969) 'Simultaneous determination of microlayer geometry and bubble growth in nucleate boiling', *International Journal of Heat and Mass Transfer*, vol. 12(8), pp. 843–846.

[62] Voutsinos C. and Judd R. (1975) 'Laser interferometric investigation of the microlayer evaporation phenomenon', *Journal of Heat Transfer*, vol. 97(1), pp. 88–92.

[63] Fath H. and Judd R. (1978) 'Influence of system pressure on microlayer evaporation heat transfer', *Journal of Heat Transfer*, vol. 100, pp. 49–55.

[64] Cooper M. (1969) 'The microlayer and bubble growth in nucleate pool boiling', *International Journal of Heat and Mass Transfer*, vol. 12(8), pp. 915–933.

[65] Yabuki T. and Nakabeppu O., 'Study on heat transfer mechanism of isolated bubble nucleate boiling with mems sensors', in '14th International Heat Transfer Conference', (2010), pp. 515–521.

[66] Utaka Y., Kashiwabara Y., and Ozaki M. (2013) 'Microlayer structure in nucleate boiling of water and ethanol at atmospheric pressure', *International Journal of Heat and Mass Transfer*, vol. 57(1), pp. 222–230.

[67] Koffman L. and Plesset M. (1983) 'Experimental observations of the microlayer in vapor bubble growth on a heated solid', *Journal of Heat Transfer*, vol. 105(3), pp. 625–632.

[68] Lay J. and Dhir V.K. (1995) 'Shape of a vapor stem during nucleate boiling of saturated liquids', *Journal of Heat Transfer*, vol. 117, pp. 394–394.

[69] Wayner P.C. (1999) 'Intermolecular forces in phase-change heat transfer: 1998 kern award review', *AIChE Journal*, vol. 45(10), pp. 2055–2068.

[70] Sharma A. (1993) 'Relationship of thin film stability and morphology to macroscopic parameters of wetting in the apolar and polar systems', *Langmuir*, vol. 9(3), pp. 861–869.

[71] Lee R. and Nydahl J. (1989) 'Numerical calculation of bubble growth in nucleate boiling from inception through departure', *Journal of Heat Transfer*, vol. 111(2), pp. 474–479.

[72] Son G., Dhir V.K., and Ramanujapu N. (1999) 'Dynamics and heat transfer associated with a single bubble during nucleate boiling on a horizontal surface', *Journal of Heat Transfer*, vol. 121(3), pp. 623–631.

[73] Son G. and Hur N. (2002) 'A coupled level set and volume-of-fluid method for the buoyancy-driven motion of fluid particles', *Numerical Heat Transfer, Part B: Fundamentals*, vol. 42(6), pp. 523–542.

[74] Mukherjee A. and Dhir V.K. (2004) 'Study of lateral merger of vapor bubbles during nucleate pool boiling', *Journal of Heat Transfer*, vol. 126(6), pp. 1023–1039.

[75] Yoon H.Y., Koshizuka S., and Oka Y. (2001) 'Direct calculation of bubble growth, departure, and rise in nucleate pool boiling', *International Journal of Multiphase Flow*, vol. 27(2), pp. 277–298.

[76] Das A., Das P., and Saha P. (2006) 'Heat transfer during pool boiling based on evaporation from micro and macrolayer', *International Journal of Heat and Mass Transfer*, vol. 49(19), pp. 3487–3499.

[77] Zhao Y.H., Masuoka T., and Tsuruta T. (2002) 'Unified theoretical prediction of fully developed nucleate boiling and critical heat flux based on a dynamic microlayer model', *International Journal of Heat and Mass Transfer*, vol. 45(15), pp. 3189–3197.

[78] Kim S.H., Lee G.C., Kang J.Y., Moriyama K., Park H.S., and Kim M.H. (2017) 'The role of surface energy in heterogeneous bubble growth on ideal surface', *International Journal of Heat and Mass Transfer*, vol. 108, pp. 1901–1909.

[79] Ramanujapu N. (1999) *Study of Growth Rate, Departure Frequency and Shape of a Single Bubble During Saturated and Subcooled Nuclear Boiling*, Ph.D. prospectus, University of California, Los Angeles.

[80] Wu J. and Dhir V.K. (2010) 'Numerical simulations of the dynamics and heat transfer associated with a single bubble in subcooled pool boiling', *Journal of Heat Transfer*, vol. 132(11), p. 111501.

[81] Bankoff S. and Mikesell R. (1959) 'Bubble growth rates in highly subcooled nucleate boiling', *Chemical Engineering Progress*, vol. 55.

[82] Robin T.T. and Snyder N.W. (1970) 'Bubble dynamics in subcooled nucleate boiling based on the mass transfer mechanism', *International Journal of Heat and Mass Transfer*, vol. 13(2), pp. 305–318.

[83] Plesset M.S. and Prosperetti A. (1978) 'The contribution of latent heat transport in subcooled nucleate boiling', *International Journal of Heat and Mass Transfer*, vol. 21(6), pp. 725–734.

[84] Snyder N. and Robin T. (1969) 'Mass-transfer model in subcooled nucleate boiling', *Journal of Heat Transfer*, vol. 91(3), pp. 404–411.

[85] Gunther F. (1951) 'Photographic study of surface-boiling heat transfer to water with forced convection', *Transactions of ASME*, vol. 73(2), pp. 115–123.

[86] Ibrahim E. and Judd R. (1985) 'An experimental investigation of the effect of subcooling on bubble growth and waiting time in nucleate boiling', *Journal of Heat Transfer*, vol. 107(1), pp. 168–174.

[87] Demiray F. and Kim J. (2004) 'Microscale heat transfer measurements during pool boiling of fc-72: effect of subcooling', *International Journal of Heat and Mass Transfer*, vol. 47(14), pp. 3257–3268.

[88] Goel P., Nayak A.K., Kulkarni P.P., and Joshi J.B. (2017) 'Experimental study on bubble departure characteristics in subcooled nucleate pool boiling', *International Journal of Multiphase Flow*, vol. 89, pp. 163–176.

[89] Berenson P.J. (1960) 'Transition boiling heat transfer from a horizontal surface', Tech. rep., Massachusetts Institute of Technology, Cambridge, Massachusetts.

[90] Ramilison J.M. and Lienhard J. (1987) 'Transition boiling heat transfer and the film transition regime', *Journal of Heat Transfer*, vol. 109(3), pp. 746–752.

[91] Yao S.C. and Henry R. (1978) 'An investigation of the minimum film boiling temperature on horizontal surfaces', *Journal of Heat Transfer*, vol. 100(2), pp. 260–267.

[92] Sharon A. and Bürger M. (1992) 'Stability analysis for the prediction of the minimum temperature of film boiling', *Chemical Engineering Communications*, vol. 118(1), pp. 207–220.

[93] Curzon F. (1978) 'The leidenfrost phenomenon', *American Journal of Physics*, vol. 46(8), pp. 825–828.

[94] Westwater J. and Santangelo J. (1955) 'Photographic study of boiling', *Industrial and Engineering Chemistry Fundamentals*, vol. 47(8), pp. 1605–1610.

[95] Bankoff S. and Mason J. (1962) 'Heat transfer from the surface of a steam bubble in turbulent subcooled liquid stream', *AIChE Journal*, vol. 8(1), pp. 30–33.

[96] Bradfield W.S. (1966) 'Liquid-solid contact in stable film boiling', *Industrial and Engineering Chemistry Fundamentals*, vol. 5(2), pp. 200–204.

[97] Kovalev S. (1966) 'An investigation of minimum heat fluxes in pool boiling of water', *International Journal of Heat and Mass Transfer*, vol. 9(11), pp. 1219–1226.

[98] Nishikawa K., Fujii T., and Honda H. (1972) 'Experimental study on the mechanism of transition boiling heat transfer: 1st report, measurements of local solid-liquid contact and temperature fluctuations on the heating surface', *Bulletin of JSME*, vol. 15(79), pp. 93–103.

[99] Ragheb H., Cheng S., and Groeneveld D. (1978) 'Measurement of transition boiling boundaries in forced convective flow', *International Journal of Heat and Mass Transfer*, vol. 21(12), pp. 1621–1624.

[100] Kao Y., Rahrooh G., and Weisman J. (1980) 'Transition boiling heat transfer in a vertical round tube', *Chemical Engineering Communications*, vol. 4(1-3), pp. 219–235.

[101] Lee L., Chen J., and Nelson R. (1982) 'Surface probe for measurement of liquid contact in film and transition boiling on high-temperature surfaces', *Review of Scientific Instruments*, vol. 53(9), pp. 1472–1476.

[102] Witte L.C. and Lienhard J.H. (1982) 'On the existence of two 'transition' boiling curves', *International Journal of Heat and Mass Transfer*, vol. 25(6), pp. 771–779.

[103] Shoji M., Witte L.C., and Sankaran S. (1990) 'The influence of surface conditions and subcooling on film-transition boiling', *Experimental Thermal and Fluid Science*, vol. 3(3), pp. 280–290.

[104] Chowdhury S.R. and Winterton R. (1985) 'Surface effects in pool boiling', *International Journal of Heat and Mass Transfer*, vol. 28(10), pp. 1881–1889.

[105] Dhuga D.S. and Winterton R. (1985) 'Measurement of surface contact in transition boiling', *International Journal of Heat and Mass Transfer*, vol. 28(10), pp. 1869–1880.

[106] Li J.Q., Mou L.W., Zhang Y.H., Yang Z.S., Hou M.H., Fan L.W., and Yu Z.T. (2018) 'An experimental study of the accelerated quenching rate and enhanced pool boiling heat transfer on rodlets with a superhydrophilic surface in subcooled water', *Experimental Thermal and Fluid Science*, vol. 92, pp. 103–112.

[107] Hsu S.H., Ho Y.H., Ho M.X., Wang J.C., and Pan C. (2015) 'On the formation of vapor film during quenching in de-ionized water and elimination of film boiling during quenching in natural sea water', *International Journal of Heat and Mass Transfer*, vol. 86, pp. 65–71.

[108] Freud R., Harari R., and Sher E. (2009) 'Collapsing criteria for vapor film around solid spheres as a fundamental stage leading to vapor explosion', *Nuclear Engineering and Design*, vol. 239(4), pp. 722–727.

[109] Kang J.y., Kim S.H., Jo H., Park G., Ahn H.S., Moriyama K., Kim M.H., and Park H.S. (2016) 'Film boiling heat transfer on a completely wettable surface with atmospheric saturated distilled water quenching', *International Journal of Heat and Mass Transfer*, vol. 93, pp. 67–74.

[110] Kim H., Buongiorno J., Hu L.W., and McKrell T. (2010) 'Nanoparticle deposition effects on the minimum heat flux point and quench front speed during quenching in water-based alumina nanofluids', *International Journal of Heat and Mass Transfer*, vol. 53(7-8), pp. 1542–1553.

[111] Fan L.W., Li J.Q., Zhang L., Yu Z.T., and Cen K.F. (2016) 'Pool boiling heat transfer on a nanoscale roughness-enhanced superhydrophilic surface for accelerated quenching in water', *Applied Thermal Engineering*, vol. 109, pp. 630–639.

[112] Kang J.y., Lee G.C., Kim M.H., Moriyama K., and Park H.S. (2018) 'Subcooled water quenching on a super-hydrophilic surface under atmospheric pressure', *International Journal of Heat and Mass Transfer*, vol. 117, pp. 538–547.

[113] Zvirin Y., Hewitt G.R., and Kenning D.B.R. (1990) 'Boiling on free-falling spheres: drag and heat transfer coefficients', *Experimental Heat Transfer*, vol. 3(3), pp. 185–214.

[114] Kenning D.B. (2004) 'Optical studies of boiling heat transfer: Insights and limitations', *International Journal of Heat and Fluid Flow*, vol. 25(2), pp. 209–222.

[115] Ohtake H. and Koizumi Y. (2004) 'Study on propagative collapse of a vapor film in film boiling (mechanism of vapor-film collapse at wall temperature above the thermodynamic limit of liquid superheat)', *International Journal of Heat and Mass Transfer*, vol. 47(8-9), pp. 1965–1977.

[116] Yagov V.V., Lexin M.A., Zabirov A.R., and Kaban'kov O.N. (2016) 'Film boiling of subcooled liquids. part I: Leidenfrost phenomenon and experimental results for subcooled water', *International Journal of Heat and Mass Transfer*, vol. 100, pp. 908–917.

[117] Yagov V.V., Leksin M.A., Zabirov A.R., and Denisov M.A. (2016) 'Film boiling of subcooled liquids. part II: Steady regimes of subcooled liquids film boiling', *International Journal of Heat and Mass Transfer*, vol. 100, pp. 918–926.

[118] Kang J.y., Kim T.K., Lee G.C., Park H.S., and Kim M.H. (2018) 'Minimum heat flux and minimum film-boiling temperature on a completely wettable surface: Effect of the bond number', *International Journal of Heat and Mass Transfer*, vol. 120, pp. 399–410.

[119] Fau S., Bergez W., and Colin C. (2017) 'Transition between nucleate and film boiling in rapid transient heating', *Experimental Thermal and Fluid Science*, vol. 83, pp. 118–128.

[120] Sher I., Harari R., Reshef R., and Sher E. (2012) 'Film boiling collapse in solid spheres immersed in a sub-cooled liquid', *Applied Thermal Engineering*, vol. 36, pp. 219–226.

[121] Uchi Y.K., Takeshi E., and Itaru M. (1992) 'Measurement of liquid-solid contact in film boiling', *International Journal of Heat and Mass Transfer*, vol. 35(6), pp. 1589–1594.

[122] Jouhara H. and Axcell B.P. (2009) 'Film boiling heat transfer and vapour film collapse on spheres, cylinders and plane surfaces', *Nuclear Engineering and Design*, vol. 239(10), pp. 1885–1900.

[123] Makishi O. and Honda H. (2012) 'Examination of minimum-heat-flux-point condition for film boiling on a sphere in terms of the limiting liquid superheat and the critical vapor film thickness', *International Journal of Heat and Mass Transfer*, vol. 55(9-10), pp. 2377–2383.

[124] Hirt C.W. and Nichols B. (1981) 'Volume of fluid (VOF) method for the dynamics of free boundaries', *Journal of Computational Physics*, vol. 39(1), pp. 201–225.

[125] Osher S. and Sethian, J. A. (1988) 'Fronts propagating with curvature dependent speed', *Journal of Computational Physics*, vol. 79, pp. 12–49.

[126] Sussman M., Smereka P., and Osher S. (1994) 'A level set approach for computing solutions to incompressible two-phase flow', *Journal of Computational Physics*, vol. 114, pp. 146–159.

[127] Sussman M., Almgren A.S., Bell J.B., Colella P., Howell L.H., and Welcome M.L. (1999) 'An adaptive level set approach for incompressible two-phase flows', *Journal of Computational Physics*, vol. 148(1), pp. 81–124.

[128] Chang Y.C., Hou T.Y., Meriman B., and Osher S. (1996) 'A level set formulation of eulerian interface capturing methods for incompressible fluid flows', *Journal of Computational Physics*, vol. 464(124), pp. 449–464.

[129] Welch S.W.J. (1995) 'Local simulation of two-phase flows including interface tracking with mass transfer', *Journal of Computational Physics*, vol. 121, pp. 142–154.

[130] Unverdi S.O. (1992) 'A front-tracking method for viscous , incompressible , multi-fluid flows', *Journal of Computational Physics*, vol. 100, pp. 25–37.

[131] Juric D. and Tryggvason G. (1996) 'A front-tracking method for dendritic solidification', *Journal of Computational Physics*, vol. 123, pp. 127–148.

[132] Popinet S. and Zaleski S. (1999) 'A front-tracking algorithm for accurate representation of surface tension', *International Journal for Numerical Methods in Fluids*, vol. 30, pp. 775–793.

[133] Peskin C.S. (1977) 'Numerical analysis of blood flow in the heart', *Journal of Computational Physics*, vol. 25, pp. 220–252.

[134] Welch S.W.J. and Wilson J. (2000) 'A volume of fluid based method for fluid flows with phase change', *Journal of Computational Physics*, vol. 160(2), pp. 662–682.

[135] Sussman M. and Puckett E.G. (2000) 'A coupled level set and volume-of-fluid method for computing 3d and axisymmetric incompressible two-phase flows', *Journal of Computational Physics*, vol. 162(2), pp. 301–337.

[136] Puckett E.G., Almgren A.S., Bell J.B., Marcus D.L., and Rider W.J. (1997) 'A high-order projection method for tracking fluid interfaces in variable density incompressible flows', *Journal of Computational Physics*, vol. 130(2), pp. 269–282.

[137] Noh W.F. and Woodward P., 'Slic (simple line interface calculation)', in A.I. van de Vooren and P.J. Zandbergen, (Editors) 'Proceedings of the Fifth International Conference on Numerical Methods in Fluid Dynamics June 28 – July 2, 1976 Twente University, Enschede', (Springer Berlin Heidelberg, Berlin, Heidelberg, 1976), pp. 330–340.

[138] Youngs D.L., 'Time-dependent multi-material flow with large fluid distortion', in K. Morton and M.E. Baines, (Editors) 'Numerical Methods for Fluid Dynamics', (Academic Press, New York, 1982), pp. 273–285.

[139] Renardy Y. and Renardy M. (2002) 'PROST: A parabolic reconstruction of surface tension for the volume-of-fluid method', *Journal of Computational Physics*, vol. 183(2), pp. 400–421.

[140] Ashgriz N. and Poo J.Y. (1991) 'FLAIR: Flux line-segment sodel for advection and interface reconstruction', *Journal of Computational Physics*, vol. 93, pp. 449–468.

[141] Brackbill J.U., Kothe D.B., and Zemach C. (1992) 'A continuum method for modeling surface tension', *Journal of Computational Physics*, vol. 100, pp. 335–354.

[142] Lafaurie B., Nardone C., Scardovelli R., Zaleski S., and Zanetti G. (1994) 'Modeling merging and fragmentation in multiphase flows with SURFER', *Journal of Computational Physics*, vol. 113, pp. 134–147.

[143] Williams M., Kothe D., and Puckett E. (1998) 'Accuracy and convergence of continuum surface tension models', *Fluid Dynamics at Interfaces, Cambridge University Press, Cambridge*, pp. 294–305.

[144] Gerlach D., Tomar G., Biswas G., and Durst F. (2006) 'Comparison of volume-of-fluid methods for surface tension-dominant two-phase flows', *International Journal of Heat and Mass Transfer*, vol. 49(3-4), pp. 740–754.

[145] Ray B., Biswas G., and Sharma A. (2010) 'Generation of secondary droplets in coalescenceof a drop at a liquid-liquid interface', *Journal of Fluid Mechanics*, vol. 655, pp. 72–104.

[146] Chakraborty I., Ray B., Biswas G., Durst F., Sharma A., and Ghoshdastidar P.S. (2009) 'Computational investigation on bubble detachment from submerged orifice in quiescent liquid under normal and reduced gravity', *Physics of Fluids*, vol. 21, p. 062103.

[147] Ray B., Biswas G., and Sharma A. (2012) 'Bubble pinch-off and scaling during liquid drop impact on liquid pool', *Physics of Fluids*, vol. 24, p. 082108.

[148] Melcher T.R. and Taylor G.I. (1969) 'Electrohydrodynamics: A review of the role of interfacial shear stresses', *Annual Review of Fluid Mechanics*, vol. 1(1), pp. 111–146.

[149] Harlow F.H. and Welch J.E. (1965) 'Numerical calculation of time-dependent viscous incompressible flow of fluid with free surface', *Physics of Fluids*, vol. 8, pp. 2182–2189.

[150] Welch S.W.J. and Rachidi T. (2002) 'Numerical computation of film boiling including conjugate heat transfer', *Numerical Heat Transfer, Part B: Fundamentals*, vol. 42, pp. 35–53.

[151] Strang G. (1968) 'On the construction and comparison of difference schemes', *SIAM Journal on Numerical Analysis*, vol. 5(3), pp. 506–517.

[152] Leonard B.P. (1979) 'A stable and accurate convective modelling procedure based on quadratic upstream interpolation', *Computer Methods in Applied Mechanics and Engineering*, vol. 19, pp. 59–98.

[153] Center for Applied Science Computing, Lawrence Livermore National Laboratory, USA (2006) *Hypre 2.0.0 user manual*, silver Ed.

[154] Sato Y. and Niceno B. (2015) 'A depletable micro-layer model for nucleate pool boiling', *Journal of Computational physics*, vol. 300, pp. 20–52.

[155] Tryggvason G. (1988) 'Numerical simulations of the Rayleigh-Taylor instability', *Journal of Computational Physics*, vol. 75(2), pp. 253–282.

[156] Ding H., Spelt P.D., and Shu C. (2007) 'Diffuse interface model for incompressible two-phase flows with large density ratios', *Journal of Computational Physics*, vol. 226(2), pp. 2078–2095.

[157] Guermond J.L. and Quartapelle L. (2000) 'A projection fem for variable density incompressible flows', *Journal of Computational Physics*, vol. 165(1), pp. 167–188.

[158] Bellman R. and Pennington R.H. (1954) 'Effects of surface tension and viscosity on Taylor instability', *Quarterly of Applied Mathematics*, vol. 12(2), pp. 151–162.

[159] Daly B.J. (1967) 'Numerical study of two fluid Rayleigh-Taylor instability', *Physics of Fluids*, vol. 10(2), pp. 297–307.

[160] Tomar G., Biswas G., Sharma A., and Agrawal A. (2005) 'Numerical simulation of bubble growth in film boiling using a coupled level-set and volume-of-fluid method', *Physics of Fluids*, vol. 17(11), p. 112103.

[161] Hens A., Biswas G., and De S. (2014) 'Analysis of interfacial instability and multimode bubble formation in saturated boiling using coupled level set and volume-of-fluid approach', *Physics of Fluids*, vol. 26(1), p. 012105.

[162] Welch S.W.J. and Biswas G. (2007) 'Direct simulation of film boiling including electrohydrodynamic forces', *Physics of Fluids*, vol. 19(1), p. 012106.

[163] Tomar G., Biswas G., Sharma A., and Welch S.W.J. (2009) 'Influence of electric field on saturated film boiling', *Physics of Fluids*, vol. 21(3), p. 032107.

[164] Tomar G., Gerlach D., Biswas G., Alleborn N., Sharma A., Durst F., Welch S., and Delgado A. (2007) 'Two-phase electrohydrodynamic simulations using

a volume-of-fluid approach', *Journal of Computational Physics*, vol. 227(2), pp. 1267–1285.

[165] Hosler E.R. and Westwater J.W. (1962) 'Film boiling on a horizontal plate', *ARS Journal*, vol. 32(4), pp. 553–558.

[166] Son G. and Dhir V.K. (1998) 'Numerical simulation of film boiling near critical pressures with a level set method', *Journal of Heat Transfer*, vol. 120, pp. 183–192.

[167] Agarwal D.K., Welch S.W.J., Biswas G., and Durst F. (2004) 'Planar simulation of bubble growth in film boiling in near-critical water using a variant of the VOF method', *Journal of Heat Transfer*, vol. 126(3), pp. 329–338.

[168] Hogrefe J.E., Peffley N.L., Goodridge C.L., Shi W.T., Hentschel H.G.E., and Lathrop D.P. (1998) 'Power-law singularities in gravity-capillary waves', *Physica D: Nonlinear Phenomena*, vol. 123(1), pp. 183–205.

[169] Duchemin L., Josserand C., and Clavin P. (2005) 'Asymptotic behavior of the Rayleigh-Taylor instability', *Physical Review Letters*, vol. 94(22), p. 224501.

[170] Kays W. and Crawford M., *Convective Heat and Mass Transfer* (McGraw-Hill, New York, 1980).

LIST OF PUBLICATIONS

Journals

- **Pandey, V.**, Biswas, G., and Dalal, A., "Effect of superheat and electric field on saturated film boiling", Physics of Fluids, 2016, Vol. 28, pp. 052102-1 – 052102-19. (available online, DOI: http://dx.doi.org/10.1063/1.4948545).

- **Pandey, V.**, Biswas, G., and Dalal, A., 2017, "Saturated film boiling at various gravity levels under the influence of electrohydrodynamic forces", Physics of Fluids, Vol. 29, pp. 032104-1 – 032104-13.
(available online, DOI: http://dx.doi.org/10.1063/1.4978056).

- **Pandey, V.**, Biswas, G., Dalal, A. and Welch, S. W. J., 2018, "Bubble lifecycle during heterogeneous nucleate boiling", ASME Journal of Heat Transfer (Under Review).

- **Pandey, V.**, Biswas, G. and Dalal, A., "Effect of surface wettability on transition of film boiling to nucleate boiling", (Manuscript ready).

Conferences

- **Pandey, V.**, Dalal, A., and Biswas, G., 2014, "Bubble Formation in Film Boiling including Electrohydrodynamic Forces", IUTAM Symposium on Multiphase Flows with Phase Change: Challenges and Opportunities, IIT Hyderabad, India.

- **Pandey, V.**, Dalal, A., Biswas, G., and Natarajan, G., 2015, "Effect of Electrohydrodynamics in Saturated Film Boiling With Varying Superheat", Paper No. CHT-15-258, ICHMT International Symposium on Advances in Computational Heat Transfer, Rutgers University, Piscataway, USA.

- **Pandey, V.**, Biswas, G., and Dalal, A., 2016, "Saturated Film Boiling in Reduced Gravity with Applied Electric Field", 4th International Conference on Computational Methods for Thermal Problems, Gerogia Tech., USA.

- **Pandey, V.**, Dalal, A., and Biswas, G., 2017, "Growth and Departure of a Single Bubble in Nucleate Boiling Regime", ICHMT International Symposium on Advances in Computational Heat Transfer, Napoli, Italy.

- **Pandey, V.**, Biswas, G., and Dalal, A., 2017, "Dependence of Growth Rate, Pinch-off Velocity and Size of a Single Bubble During Film Boiling on Superheat and Gravity-level", Paper No: IHMTC2017-13-1109, Proceedings of the 24th National and 2nd International ISHMT-ASTFE Heat and Mass Transfer Conference, BITS-Pilani, Hyderabad, India.

- **Pandey, V.**, Dalal, A., and Biswas, G., 2018, "Surface Wettability Instigated Transition from Film to Nucleate Boiling Regime", The 16th International Heat Transfer Conference, China National Convention Center, Beijing, China, August 10-15 (submitted).